WESTFÄLISCHE
WILHELMS-UNIVERSITÄT
MÜNSTER

Description of particle production in pp, p–Pb and Pb–Pb collisions at the LHC using PYTHIA

MASTER THESIS

Tim Stellhorn

First Referee: Anton Andronic
Second Referee: Christian Klein-Bösing

Westfälische Wilhelms-Universität Münster
Institut für Kernphysik
AG Andronic

— August 2023 —

„There's something that doesn't make sense.
Let's go and poke it with a stick."

- Eleventh Doctor
from: Doctor Who
written by: Steven Moffat

Contents

Acronyms

QGP	Quark-Gluon Plasma
MC	Monte-Carlo
ALICE	A Large Ion Collider Experiment
LHC	Large Hadron Collider
pp	Proton-Proton
p–Pb	Proton-Lead
Pb–Pb	Lead-Lead
QCD	Quantum ChromoDynamics
QED	Quantum ElectroDynamics
CMS	Centre-of-Mass System
NN	Nucleon-Nucleon
IP	Interaction Point
ZDC	Zero Degree Calorimeter
ITS	Inner Tracking System
TPC	Time-Projection Chamber
TRD	Transition Radiation Detector
TOF	Time-Of-Flight
HMPID	High Momentum Particle Identification Detector
PHOS	PHOton Spectrometer
EMCal	ElectroMagnetic Calorimeter
SPD	Silicon Pixel Detector
SDD	Silicon Drift Detector
SSD	Silicon Strip Detector
MB	Minimum-Bias
NSD	Non-Single Diffractive
ISR	Initial State Radiation
FSR	Final State Radiation
MPI	MultiParton Interaction
BSM	Beyond Standard Model

1. Introduction

In the introductory quote, the Doctor from the British TV series *Doctor Who* is confronted with a phenomenon he does not quite understand. His solution is to "poke it with a stick" to find out more about its nature.
One could say that particle physicists have a similar approach in order to understand the elementary building blocks of matter. Many open questions represent the "something that doesn't make sense". Among them are the search for dark matter and dark energy, the unification of forces or the search for new exotic particles, just to name a few. Of special importance for this thesis is the exploration of a particular state of matter, the Quark-Gluon Plasma (QGP).
The "stick" that is used to investigate these questions are particles that are accelerated to velocities close to the speed of light. The unknown is then "poked" with the stick by colliding the accelerated particles which leads to new particles being created from the energy of the collision. Outgoing particles are then measured by a surrounding particle detector. Using these data, physicists search for new processes that might occur under the extreme conditions present in high-energetic particle collisions.
Nevertheless, the detector can not directly measure all the occurring processes and most of them can also not be calculated analytically. Instead, one can simulate the particle collision and the interactions of newly created particles with each other in a Monte-Carlo (MC) event generator. Data from these simulations can be used to test new theoretical models by comparing them with the data measured in accelerator experiments.
In this thesis, results from simulations with the PYTHIA event generator will be compared with data from the ALICE (A Large Ion Collider Experiment) detector located at the Large Hadron Collider (LHC). Additionally to collisions of protons (pp), collisions including heavy ions like proton-lead (p-Pb) and lead-lead (Pb–Pb) collisions are of special interest. These are simulated by the Angantyr model. The aim of the thesis is to describe the different steps of particle production in PYTHIA and Angantyr and to analyse how well the simulation results reproduce measured data. A special focus lies on the description of effects that are ascribed to the formation of a QGP.
In order to do so, the theory behind particle collisions is elaborated first in section 2. Afterwards, section 3 gives an overview of how the ALICE detector works and which datasets are used in this thesis. Section 4 presents the different steps in the PYTHIA event generator and the Angantyr model before the results of my simulations are analysed and discussed in section 5. Finally, concluding thoughts will be presented in section 6.

2. Theoretical Background

In this chapter, the main theory behind high-energy particle collisions is described. Its theoretical foundation is the standard model of particle physics. It describes our current knowledge about the elementary constituents of matter and three out of four fundamental forces of nature, i.e. the electromagnetic, weak and strong interaction. Gravity is not included in the standard model but is also neglectable at (sub)atomic levels. Hence, it does not play any role in the scope of this thesis.

The constituents of the standard model will be described further in section 2.1. The following subsection explains in more detail the strong interaction and the Lund string model which is a basic part of simulations with PYTHIA. Thereafter, some observables in particle collisions are discussed. Also, different kinds of process classes in PYTHIA hadron-hadron collisions are introduced in section 2.4 that are relevant for the data analysis. Finally, the last subsection gives an overview of heavy-ion collisions and the Glauber Model.

2.1. The Standard Model

The standard model of particle physics [BD16], shown in fig. 1, divides the elementary particles into two different groups. One group are the fermions which constitute the known matter, while the other group contains bosons which describe interactions between particles.

Fermions are again divided into quarks and leptons. Both appear in three different generations. Each generation contains two particles with different electric charge and mass. Also, each fermion has an antiparticle with the same mass but opposite charge.

Quarks (q) interact via all four fundamental forces. There are up-type quarks (u, c, t) with an electric charge of +2/3 and down-type quarks (d, s, b) with an electric charge of -1/3. Additionally, quarks carry one out of three possible colour charges (r = red, g = green and b = blue) which lets them interact via the strong force. Respectively, antiquarks ($\bar{q}$) carry an anticolour ($\bar{r}, \bar{g}, \bar{b}$).

In contrast to quarks, leptons do not carry a colour charge and thus do not interact strongly. On the one side, one finds the electron (e), muon (μ) and tauon (τ) with an electric charge of -1. They interact weakly and electromagnetically. On the other side are the electron (ν_e), muon (ν_μ) and tau (ν_τ) neutrinos. They have no charge and therefore only interact weakly.

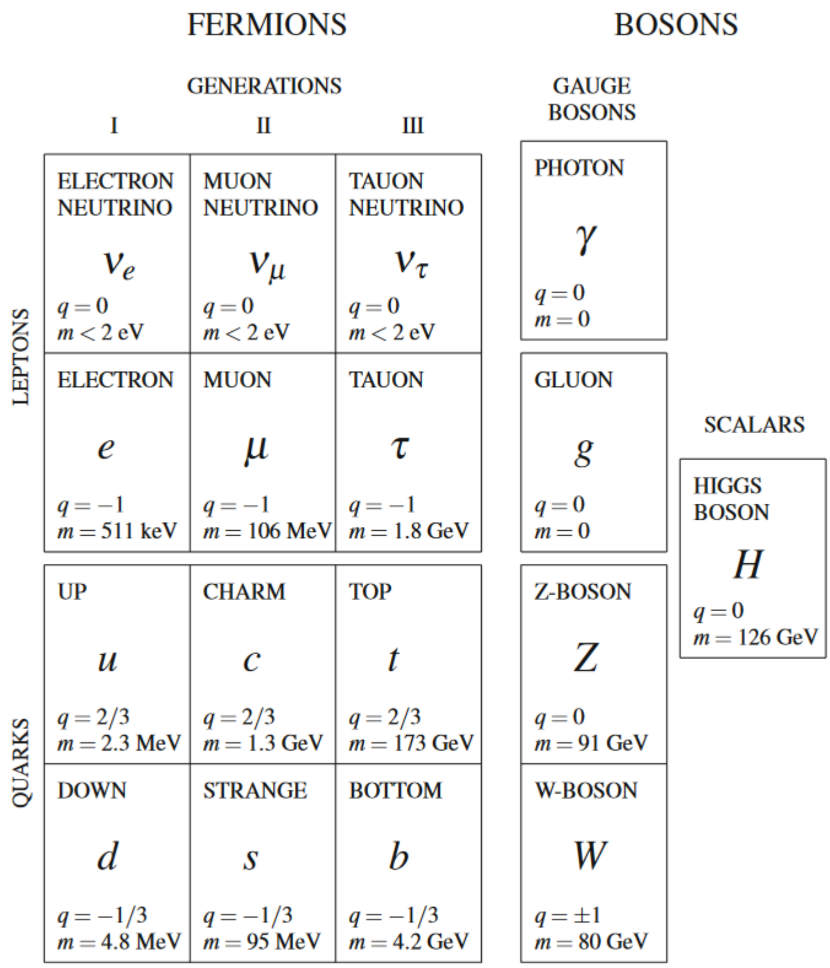

Figure 1: The standard model of particle physics with q being the electric charge and m the rest energy of the particles. Taken from [BD16] fig. 3.1.

Bosons are divided into gauge bosons, mediators of the fundamental forces, and a scalar boson called Higgs particle which gives other elementary particles their mass. Among the gauge bosons is the photon (γ) which mediates the electromagnetic interaction. The weak interaction is induced by the heavy $W^{\pm}$ and Z bosons. Finally, the gluons (g) mediate the strong interaction. While photons do not carry electromagnetic charge, gluons carry a combination of colour and anticolour and can thus interact with themselves. The fourth known fundamental force, gravity, can not (yet) be described by the standard model.

Despite its strengths, the standard model leaves many phenomena unexplained. As already discussed, it does not provide a unified theory including gravity. Also other questions like the origin of dark matter and dark energy remain unanswered.

2.2. Quantum Chromodynamics

This section takes a closer look at the strong interaction described by the theory of Quantum ChromoDynamics (QCD). It is based on the SU(3) symmetry group and is therefore invariant under rotation of colours. Furthermore, gluons as the mediators of QCD appear as a colour-octet state with eight gluons carrying a different combination of colour and anticolour. Introducing this colour charge, one would expect to find hadrons (particles made up of quarks) with different net colour charges. As they have not been observed, it is believed that only colour singlet states with no net colour (or net colour white) can exist as free particles. These singlet states can be obtained in two different ways: three quarks with only different colours sum up to a net colour of white as well as a quark with a colour and an antiquark with the respective anticolour. The mentioned states are called baryons (qqq) or mesons ($q\bar{q}$). [BD16] [Dem17]
The interaction between quarks is described by the quark-antiquark-potential as shown in eq. (1), where α_s is the coupling constant of the strong interaction and the string constant κ is approximately $1\,\mathrm{GeV/fm}$. [FS18]

$$V_{\mathrm{QCD}} = -\frac{4}{3}\frac{\alpha_{\mathrm{s}} \cdot \hbar c}{r} + \kappa \cdot r \tag{1}$$

In this equation, the first term is dominating for small distances r between the quarks and leads to a behaviour similar to the electromagnetic interaction described by Quantum ElectroDynamics (QED). For large r, the second term dominates and the potential rises almost linearly with the distance. Trying to pull a quark and an antiquark apart would therefore only increase the energy which holds them together. The force lines form a flux tube between the two separated quarks where the gluons are interacting with themselves. When the energy of the flux tube is large enough, a new $q\bar{q}$ pair is created and mesons are formed in which the quarks remain confined. Hence, particles like quarks which carry a colour charge can not be free. This phenomenon is called confinement.
However, the coupling constant $\alpha_{\mathrm{s}}(Q^2)$ actually depends on the momentum transfer Q^2. In first order perturbation theory, it is given by [Pov+14]

$$\alpha_{\mathrm{s}}(Q^2) = \frac{12\pi}{(33 - 2N_{\mathrm{q}}) \cdot \ln\left(\frac{Q^2}{\Lambda_{\mathrm{QCD}}^2}\right)} \tag{2}$$

Here, N_{q} is the number of quark flavours and Λ_{QCD} is a free parameter which has been found experimentally to be $\Lambda_{\mathrm{QCD}} \approx 250\,\mathrm{MeV}$ [Pov+14]. Equation (2) shows that the strong coupling decreases with increasing Q^2 which corresponds to a small distance between the quarks. Perturbation theory is only applicable if $\alpha_s << 1$ meaning $Q^2 >> \Lambda^2_{\mathrm{QCD}} \approx 0.06\,\mathrm{GeV}^2$, also referred to as the hard QCD regime. In the limes $Q^2 \to \infty$, quarks are seen as free which is called asymptotic freedom. [Pov+14]

2.2.1. The Lund String Model

As mentioned in the previous section, perturbation theory breaks down at lower energy scales. Thus, phenomenological models are required to describe the non-perturbative hadronisation process in particle collisions. Hadronisation in PYTHIA, for example, is based on the Lund String Model. [AS00]

This model describes the breakup of a high-energy $q\bar{q}$ system into several systems with smaller energy. It is based on the following assumptions: i) spanned between the quarks is a coloured force field, ii) causality and Lorentz covariance are given and iii) particle production can be described as a stochastical process which is eventually stopped by saturation. Moreover, only the linear term of the QCD potential (see eq. (1)) is taken into consideration. The colour flux tube between a quark and an antiquark can thus be simplified to a one-dimensional string with the (anti-)quarks at the endpoints as shown in fig. 2. The gluons are then seen as excitations on the string. [FS18]

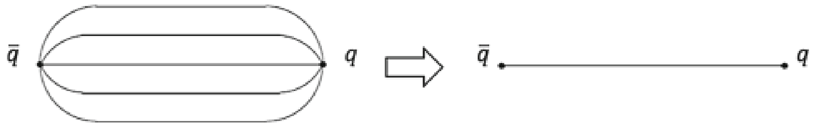

Figure 2: Sketch of a simplified colour force field between a $q\bar{q}$ pair and on the right the further simplified string representation. Taken from [FS18] fig. 1.

Figure 3 depicts an original $q_0\bar{q}_0$ pair which is assumed as massless and can therefore be created at a single space-time point. The quarks are then moving apart along the light cone which stretches the string between them and the energy stored in the string increases with the string constant κ. If the energy gets large enough, a virtual $q_1\bar{q}_1$ pair can become on-shell and break the string. The breaking points are represented in the illustration as black dots. The newly created pair is also assumed to be massless and moves apart along the lightcone. If the invariant mass in one of the systems is still large enough, more $q_j\bar{q}_j$ pairs can be created which breaks the string further.

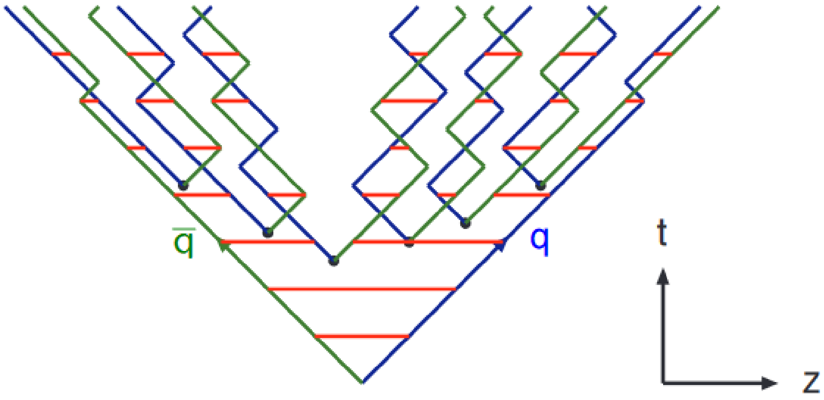

Figure 3: Illustration of an original $q\bar{q}$ pair moving apart causing further pair creation and string break ups. Taken from [Buc+11] fig. 13.

In contrast to the assumption of massless quarks, heavy quarks have to be created with a certain distance to each other. From a quantum mechanical point of view, the quarks are created in one point and are then tunneling towards a classically allowed distance. Due to these quantum mechanical processes, the production of heavy quarks is suppressed by factors of $u : d : s : c \approx 1 : 1 : 0.3 : 10^{-11}$. [Buc+11]
Eventually, a quark q_j will form a meson together with an antiquark $q_{\bar{j-1}}$ from an adjacent string break. One possibility for baryon production is a diquark-antidiquark pair emerging from a string break. Together with a quark or an antiquark from an adjacent break, this pair can fragment into baryons. Another possibility is the popcorn model, which will not be discussed here in further detail. [Buc+11]

2.3. Physical Observables

This chapter describes different observables that can be used to characterise high-energy particle collisions. [Dem17] In doing so, natural units are used throughout this thesis with $c = \hbar = 1$. Firstly, different kinematic variables are described in section 2.3.1. Secondly, building on these variables, the measured spectra that are discussed in this thesis are presented in section 2.3.2.

2.3.1. Kinematic Variables

In particle physics, momenta are often given as 4-vectors containing the energy E and the 3-momentum $\vec{p}$ of the particle: $p^\mu = (p^0, p^1, p^2, p^3) = (E, \vec{p})$. By squaring the 4-momentum p, one obtains a relation between energy and momentum of a particle:

$$m_0^2 = E^2 - p^2 \tag{3}$$

Equation (3) gives a formula for the rest energy m_0 of a particle. The rest energy or invariant mass of a system of two particles is given as the square root of the Mandelstam variable s which is defined for two colliding particles a and b as follows:

$$s = (p_a + p_b)^2 \overset{\text{CMS}}{=} (E_a + E_b)^2 \tag{4}$$

This quantity is invariant under Lorentz transformation and simplifies to a squared sum of the energies in the Centre-of-Mass System (CMS). It represents the energy available for the creation of new particles after a collision as it does not depend on the kinetic energy of the colliding particles.
Secondly, particles resulting from a collision are described in terms of their transverse momentum p_T, i.e. the component of the momentum which is perpendicular to the beam line. It can be calculated via

$$p_\mathrm{T} = |\vec{p}| \sin\theta \tag{5}$$

where θ is the polar angle of a particle which is increasing clockwise from the beam line to the axis pointing upwards (see fig. 10 in section 3.1). Since the momenta before the collision are mainly aligned in direction of the beam line, the p_T of resulting particles originates from the collision energy.
Another variable used to describe the movement of particles after the collision is the rapidity: [Ber06]

$$y = \frac{1}{2} \cdot \ln\left(\frac{1 + \frac{v_z}{c}}{1 - \frac{v_z}{c}}\right) = \frac{1}{2} \cdot \ln\left(\frac{E + p_z}{E - p_z}\right) \tag{6}$$

In eq. (6), v_z and p_z are the components of velocity and momentum parallel to the beam

line and E is the total energy of a particle. The rapidity is a measure of the velocity in terms of the speed of light c. A particle with $y = 0$ moves perpendicular to the beam and a particle with $y = \pm\infty$ moves parallel to the beam.
To measure the rapidity one needs to identify the particles to obtain their energy which depends on their mass according to eq. (3). This can be difficult and thus the pseudorapidity η is given as:

$$\eta = \frac{1}{2} \cdot \frac{|\vec{p}| + p_z}{|\vec{p}| - p_z} = -\ln\left(\tan\frac{\theta}{2}\right) \tag{7}$$

It is defined in terms of the absolute value of the 3-momentum of a particle instead of its energy. Hence, it is not required to identify a particle to determine its pseudorapidity. It even simplifies to a formula depending only on the polar angle θ so that it is sufficient to measure the angular distribution.
Still, rapidity and pseudorapidity show the same behaviour towards infinite values. In case of high-energetic collisions, where $m \ll |\vec{p}|$, the approximation $y \approx \eta$ is justified. [Ber06]

2.3.2. Measured Spectra

In this thesis, transverse-momentum spectra $1/N_{\mathrm{ev}} \cdot d^2N/(dp_{\mathrm{T}}d\eta)$ are used to determine the probability of finding particles with a certain p_T after a collision. These distributions also depend on the (pseudo-)rapidity interval in which the particles are measured and they are normalised by the number of observed events. Hereby, the term “event” denotes the outcome of one collision.
Additionally, these spectra only include primary charged particles. This kind of particle is defined in ALICE as a “charged particle with a mean proper lifetime τ larger than 1 cm which is either produced directly in the interaction, or from decays of particles with τ smaller than 1 cm, excluding particles produced in interactions with the detector material” [ALI18].
Another observable which will be analysed is the charged-particle multiplicity. For each event, it gives the number of primary charged particles. For a large number of events, one can obtain the probability $P(N_{\mathrm{ch}})$ to find a particular number of charged particles in an event from the multiplicity. [GR10]

2.4. PYTHIA Event Classes in Hadron-Hadron Collisions

The total cross section for a collision between two high-energetic hadrons A and B is in PYTHIA defined as: [Bie+22]

$$\begin{aligned}\sigma_{\mathrm{tot}}^{AB}(s) &= \sigma_{\mathrm{el}}^{AB}(s) + \sigma_{\mathrm{inel}}^{AB}(s) \\ &= \sigma_{\mathrm{el}}^{AB}(s) + \sigma_{\mathrm{sd(XB)}}^{AB}(s) + \sigma_{\mathrm{sd(AX)}}^{AB}(s) + \sigma_{\mathrm{dd}}^{AB}(s) + \sigma_{\mathrm{cd}}^{AB}(s) + \sigma_{\mathrm{nd}}^{AB}(s)\end{aligned} \tag{8}$$

It is divided into an elastic and an inelastic part. In an elastic scattering $AB \to AB$, the hadrons are scattered by a certain angle but remain unharmed. All other scatterings, where the final state differs from AB, are summarised under the term inelastic.

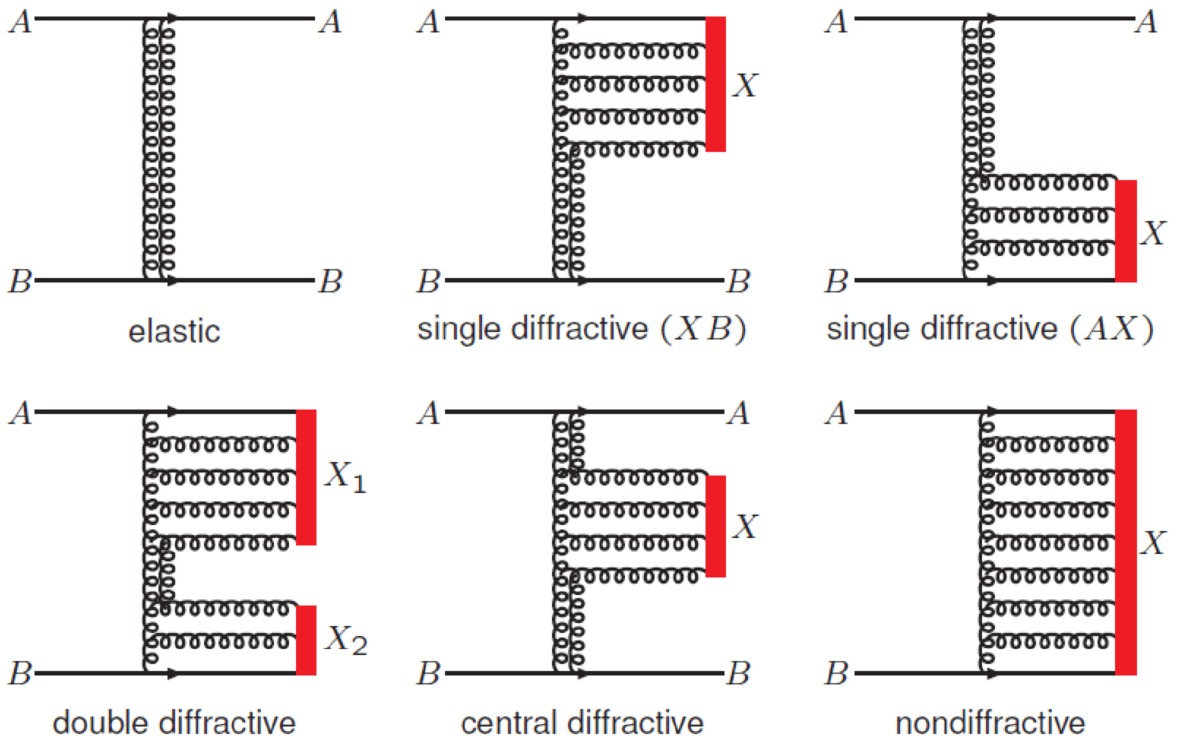

Figure 4: Illustration of different event classes of interactions between two high-energetic hadrons A and B. A single vertical gluon represents a colour-octet exchange, while a pair of gluon gives a colour-singlet exchange (a pomeron). The vertical axis represents the rapidity range spanned between the hadrons and the red bars are regions where hadrons are produced. Taken from [Bie+22] fig. 9.

Among these inelastic scatterings are single diffractive (sd) ones, where either hadron A or hadron B results in an excited system X from which new hadrons will be produced (either $AB \to XB$ or $AB \to AX$). In a double diffractive (dd) scattering $AB \to X_1X_2$, both hadrons are excited but remain separate systems. Central diffraction (cd) means that both hadrons survive. However, they both lose energy to a new central excited system ($AB \to AXB$) which then creates new particles. In contrast to that, in a nondiffractive (nd) interaction $AB \to X$ both hadrons break up and form a common excited system X. The inelastic nondiffractive part is also called absorption and is modelled in PYTHIA by colour exchange between the colliding hadrons. Similarly, diffraction is modelled as a colour neutral exchange of pomerons, a hypothetical particle consisting of glueballs.
Experimentally, single and double diffractive scatterings are identified because particle production only takes place at one or both ends of the rapidity range as portrayed in fig. 4. In between is a so-called rapidity gap where no particles are created since there is no net colour exchange. This is different in nondiffractive interactions, where particles are assumed to be created over the whole available rapidity range.

2.5. Collisions Including Heavy Ions

This section describes special characteristics in collisions with heavy ions in more detail. Specifically, the two cases discussed in the following are a) a proton colliding with a nucleus containing A nucleons (pA collision) or b) two nuclei with the same mass number colliding with each other (AA collision). In this thesis, collisions of lead ions with protons (p–Pb) or with other lead ions (Pb–Pb) are of particular interest since they can be compared with ALICE data.
In the following subsections, the concept of centrality is introduced first to characterise collisions including heavy ions. Afterwards, a brief overview of the Glauber formalism is given, which is used in Angantyr to simulate heavy-ion collisions. Finally, several effects that are based on the formation of a QGP will be presented. The QGP is a special state of matter that exists only under extreme conditions and that is assumed to have existed very shortly after the Big Bang.

2.5.1. Centrality

As nuclei are extended objects, the outcome of the collision depends amongst others on the number of participating nucleons. In a central collision, there are more nucleons colliding than in a peripheral collision. Hence, the centrality is an important quantity in heavy-ion collisions. [Sne11]
An illustration of such a collision is given in fig. 5. There, the lead nuclei are assumed to be disks, where an interaction occurs if the disks overlap. This assumption is viable as the longitudinal size of the nuclei is Lorentz contracted by a factor $\gamma \sim 100$ in comparison to their radial extent. The distance between the centres of the two disks is given by the impact parameter b. Thus, the smaller b is, the more nucleons are interacting (or "wounded"). They are so-called participants in the collision while the non-interacting nucleons are called spectators.

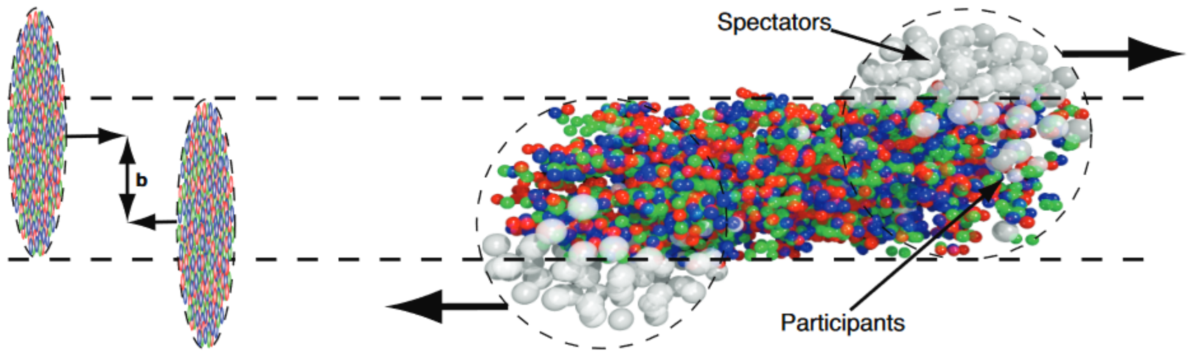

Figure 5: Depiction of a collisions between two ions viewed as disks. Only nucleons in the overlap region can interact with each other. Taken from [Sne11] fig. 2.

In heavy-ion collisions, the centrality

$$c = \frac{\sigma(b)}{\sigma(b_{\max})} = \frac{b^2}{4R_A^2} \tag{9}$$

is defined as a fraction of geometrical cross sections and depends on the impact parameter b and the nuclear radius R_A of the colliding ions. The maximum impact parameter $b_{\max}$ corresponds to $2R_A$.
Experimentally, the centrality is defined through the measured charged-particle multiplicity because the impact parameter can not be observed directly. The events with the highest number of charged particles are assigned to be the most central events while events with low multiplicities are interpreted as peripheral.

2.5.2. Glauber Model

The Glauber model [Mil+07] describes a heavy-ion collision as a sequence of binary Nucleon-Nucleon (NN) interactions as already outlined in section 2.5.1. It is used in Angantyr to calculate the number of wounded nucleons and of NN collisions in an event. In the following, the formalism is presented for the case of AA collisions but it works similarly for pA collisions between protons and ions.
In the optical limit, the nucleons are assumed to move independently inside the nuclei and that the latter ones are large in comparison to the range of the NN interaction. Furthermore, the nucleons are seen as undeflected and thus travel along straight trajectories while the nuclei collide. In this limit, the resulting number $N_{\text{part}}(\vec{b})$ of participating nucleons as well as the number $N_{\text{coll}}(\vec{b})$ of nucleon-nuceleon collisions can be calculated analytically.

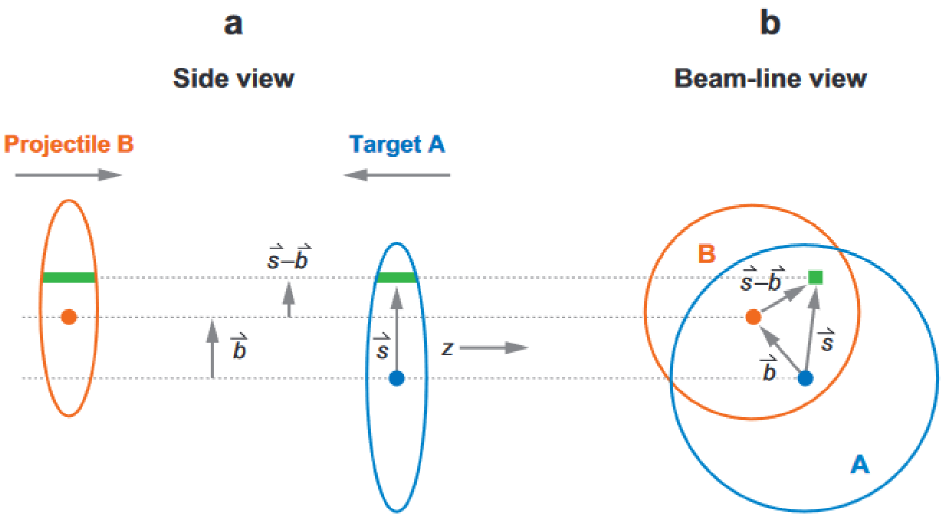

Figure 6: Sketch of a collision between a target nucleus A and a projectile nucleus B once viewed from the side and once viewed in direction of the beam line. Taken from [Mil+07] fig. 3.

Figure 6 shows a collision between two nuclei similar to fig. 5, but with a beam line view additionally to the side view. Here, two flux tubes are highlighted with the vector $\vec{s}$ marking the distance from the centre of target A to the flux tube and the vector $\vec{s}-\vec{b}$ marking the distance from the centre of projectile B to the flux tube.

The probability

$$\hat{T}_A(\vec{s}) = \int \hat{\rho}_A(\vec{s}, z_A)\, dz_A \tag{10}$$

to find a nucleon in the target flux tube is defined as a function of the distance $\vec{s}$ of the nucleon from the centre of the nucleus. It is obtained by integrating over the probability per unit volume $\hat{\rho}_A(\vec{s}, z_A)$ for a nucleon to be located at position $(\vec{s}, z_A)$ where z_A can assume all possible positions inside the nucleus along the beam line axis. An analogous term can be written for the projectile flux tube.
During the collision, these flux tubes overlap and the product $\hat{T}_A(\vec{s})\, \hat{T}_B(\vec{s}-\vec{b})\, d^2s$ can be interpreted as the probability per unit area for nucleons to be located in the respective overlapping flux tubes. Integrating over all values of $\vec{s}$ in this product results into the thickness function

$$\hat{T}_{AB}(\vec{b}) = \int \hat{T}_A(\vec{s})\, \hat{T}_B(\vec{s} - \vec{b})\, d^2s. \tag{11}$$

This function gives the overlap area in which a specific nucleon in A can interact with a given nucleon in B. Elastic processes are not considered in the Glauber Model due to their very little energy loss. Hence, the probability for an interaction to occur can be calculated by $\hat{T}_{AB}(\vec{b}) \cdot \sigma_{\text{inel}}^{NN}$, where $\sigma_{\text{inel}}^{NN}$ is the NN inelastic cross section.
With a number of a nucleons in target A and b nucleons in projectile B, the probability

$$P(n, \vec{b}) = \binom{ab}{n} \left[\hat{T}_{AB}(\vec{b}) \cdot \sigma_{\text{inel}}^{NN}\right]^n \left[1 - \hat{T}_{AB}(\vec{b}) \cdot \sigma_{\text{inel}}^{\text{NN}}\right]^{ab-n} \tag{12}$$

for n interactions to occur between the nucleons is expressed as a binomial distribution. In this equation, the first term gives the possible combination for getting n collisions out of all possible nucleon-nucleon interactions (expressed as the product ab). The second term states the probability for n collisions to occur and the last term is the probability for having $ab - n$ nucleon pairs which are not colliding.
Using this distribution, the total number of NN collisions can be written as a sum over all values of n:

$$N_{\text{coll}}(\vec{b}) = \sum_{n=1}^{ab} n \cdot P(n, \vec{b}) = ab \cdot \hat{T}_{AB}(\vec{b}) \cdot \sigma_{\text{inel}}^{\text{NN}} \tag{13}$$

Starting again from eq. (10), one can also calculate the number of participating nucleons

$$
\begin{aligned}
N_{\text{part}}(\vec{b}) = a \cdot \int \hat{T}_A(\vec{s}) \left(1 - \left[1 - \hat{T}_B(\vec{s}-\vec{b})\, \sigma_{\text{inel}}^{\text{NN}}\right]^B\right) d^2s \\
+ b \cdot \int \hat{T}_B(\vec{s}-\vec{b}) \left(1 - \left[1 - \hat{T}_A(\vec{s})\, \sigma_{\text{inel}}^{\text{NN}}\right]^A\right) d^2s
\end{aligned}
\tag{14}
$$

as an integral over all distances $\vec{s}$ from the respective target / projectile centre. The integral over the bracketed terms also represents the inelastic cross section

$$
\sigma_{\text{inel}}^{A} = \int d^2s \left(1 - \left[1 - \hat{T}_A(\vec{s})\, \sigma_{\text{inel}}^{\text{NN}}\right]^A\right) \tag{15}
$$

for nucleon-nucleus collisions between a projectile (target) nucleon and the target nucleus A (projectile nucleus B).

In contrast to the optical Glauber model which is based on a continuous nucleon density distribution, the nucleons in the Monte-Carlo approach are located at specific coordinates. Regarding the nuclear density distributions of the colliding nuclei, the nucleons are placed in a three-dimensional coordinate system and a random impact parameter is created. This makes it possible to apply centrality cuts similar to the analysis of measured data. Similar to the optical approach, the collision is then described in terms of the individual interactions of the participating nucleons where these travel along straight lines and $\sigma_{\text{inel}}^{NN}$ is assumed to be independent of the number of collisions that were performed before. Finally, by simulating a large number of collisions, the Glauber MC approach gives average values for $\langle N_{\text{part}} \rangle$ and $\langle N_{\text{coll}} \rangle$.

2.5.3. Quark Gluon Plasma (QGP)

QGP [Ian14] is a state of matter where quarks and gluons (subsumed under the term partons) are not confined in hadrons as in normal hadronic matter. According to eq. (2), this can be achieved at high temperatures ($> 170\,\text{MeV}$) or at small distances between the quarks which corresponds to high nuclear densities. The extreme conditions that occur in a high-energetic heavy-ion collision can fulfil these requirements. If the energy density in the collision exceeds a critical value of about $1\,\text{GeV}\,\text{fm}^{-1}$, QGP forms. In this state, the attractive forces on the quarks are small and they can move around freely.

Figure 7 shows the evolution of QGP in several stages. Firstly, the two lead beams move towards each other from opposite directions and collide at time $t \sim 0\,\mathrm{fm}$. This can be described as a collision between two disks as illustrated in fig. 5. Instead of evolving independently, the resulting partons show collective phenomena which will be discussed in more detail later. Due to these interactions, the partonic matter rapidly thermalises in a time $t \leqslant 1\,\mathrm{fm}$. When thermal equilibrium is reached, the partonic system transforms into a state of a strongly coupled fluid, the QGP. While expanding, the system cools down in further partonic scatterings and at $t \sim 10\,\mathrm{fm}$, the temperature drops under the critical value T_c. As a result, the system transitions back into an hadronic state.
In this hadron gas phase, the system expands and cools down further in inelastic hadron-hadron collisions. When reaching the chemical freeze-out temperature T_ch, inelastic scattering ceases and the particle species become fixed. Elastic scattering continues until the kinetic freeze-out temperature T_fo is reached at $t \sim 20\,\mathrm{fm}$. This marks the transition from a fluid state to a system of free particles. These particles are then moving independently and are measured in the surrounding detector. Finally, the properties of these final-state particles give more insights on the characteristics of QGP.

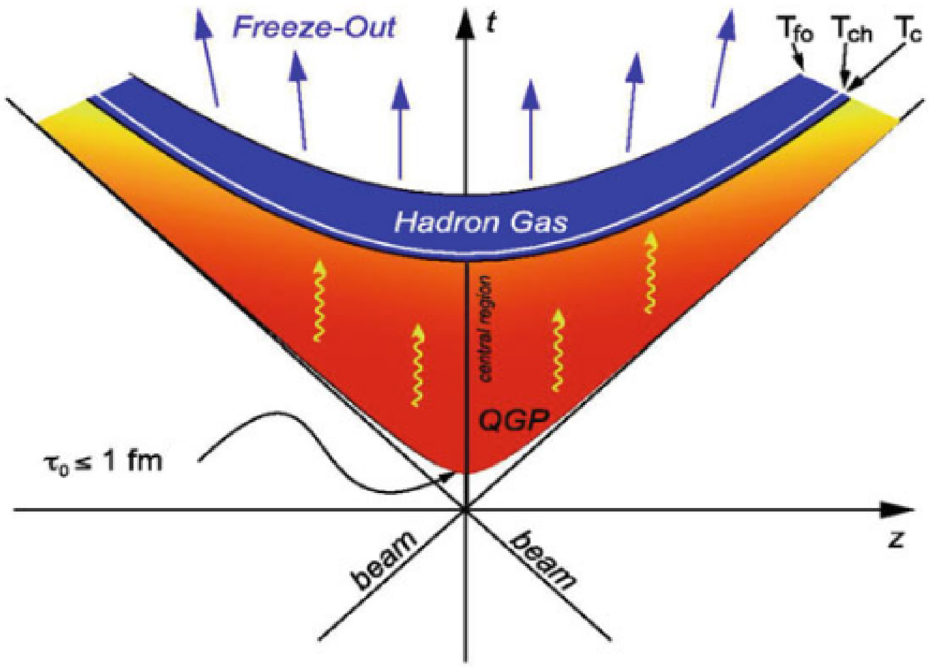

Figure 7: Schematic portrayal of the formation and evolution of QGP in a heavy-ion collision in one spatial (z) and one temporal (t) dimension. T_c is the critical temperature for QGP to turn into hadrons, T_ch the temperature of the chemical freeze-out where inelastic scattering ceases and T_fo the kinetic freeze-out temperature where elastic scattering ceases. Taken from [Kli+09] fig. 2.

As already mentioned, particles show a collective behaviour in the formation of QGP. This behaviour is called an anisotropic flow and it is caused by asymmetries in the geometry of heavy-ion collisions. Figure 8 displays the initially almond shaped form of the overlap region which leads to strong pressure gradients in the reaction plane. Hence, particles are expanding mainly in the reaction plane, converting the initial spatial anisotropy into a momentum anisotropy. This is called the elliptic flow, characterised by the second order Fourier coefficient $v_2 = \langle \cos 2\varphi \rangle$, where φ is the azimuthal angle in the reaction plane. Higher order Fourier coefficients are also present in the anisotropic flow and arise from initial fluctuations in the geometry. [Sne11]

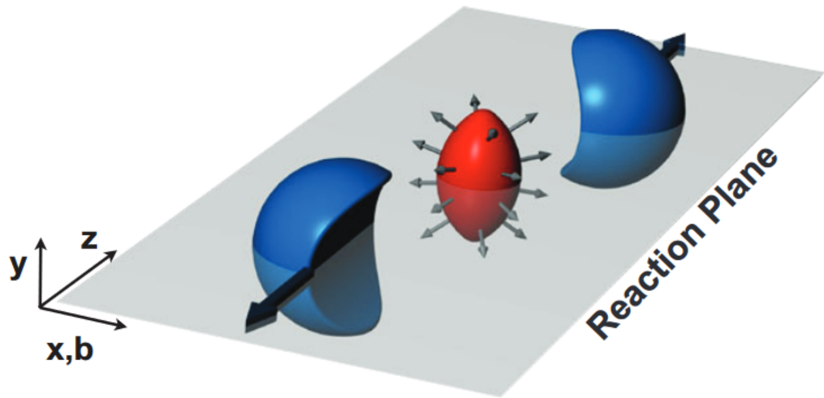

Figure 8: Illustration of asymmetries in the spatial overlap during a heavy-ion collision leading to anisotropic flow. Taken from [Sne11] fig. 4.

Another phenomenon observed in QGP is the so-called jet quenching [dEn10]. Jets are collimated sprays of hadrons resulting from high-energetic partons. These partons were created in a hard scattering process between partons from each one of the colliding hadrons. Due to interactions with the surrounding medium, the partons lose energy by radiating gluons or splitting into quark-antiquark pairs. The longer a parton travels through the plasma, the more energy it loses (it is quenched). Eventually leaving the medium, it hadronises into a (possibly quenched) jet which can be seen in fig. 9.
The jets are used as hard probes (due to their high energy) to study QGP properties which can be characterised by the energy loss of partons inside the plasma. These properties are for example the medium temperature T, the gluon density $\mathrm{d}N^g/\mathrm{d}y$ inside the plasma or the transport coefficient $\langle \hat{q} \rangle$. This coefficient resembles the average p_T^2 that a parton acquires per unit path length.

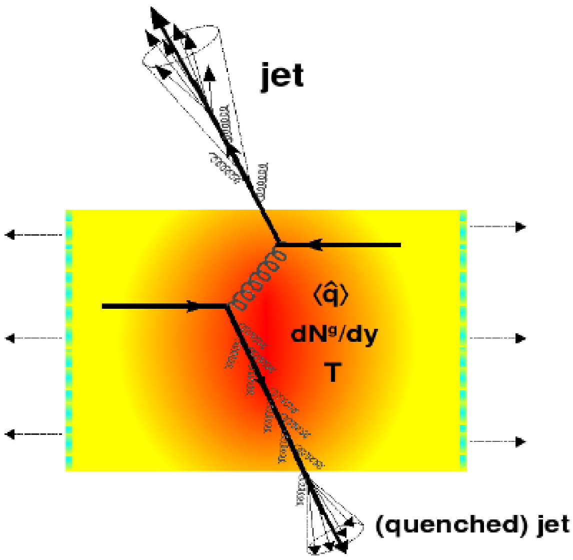

Figure 9: Depiction of two high-energetic partons resulting from a hard scattering process in a nucleus-nucleus collision. One parton leaves the plasma directly and hadronises into a jet of hadrons while the other one suffers energy loss due to the radiation of gluons in the medium and fragments outside the medium into a quenched jet. Taken from [dEn10] fig. 2.

In contrast to hadron jets, the quenching does not occur in the emission of photons as they are not interacting via the strong force with the plasma. QGP is thus not opaque for photons and they can leave the medium unaffected.
Jet quenching can also be quantified by using the nuclear modification factor [And14]

$$R_{\mathrm{AA}} = \frac{d^2N_{\mathrm{AA}}/dydp_{\mathrm{T}}}{\langle N_{\mathrm{coll}}\rangle \cdot d^2N_{\mathrm{pp}}/dydp_{\mathrm{T}}} \tag{16}$$

which compares a chosen observable measured in heavy-ion collisions to the respective observable in pp collisions. Here, $d^2N/dydp_{\mathrm{T}}$ represents the yield of the studied observable in pp or AA collisions and $\langle N_{\mathrm{coll}}\rangle$ denotes the average number of nucleon-nucleon collisions inside the AA collision.
Any enhancement ($R_{\mathrm{AA}} > 1$) or suppression ($R_{\mathrm{AA}} < 1$) in eq. (16) can be used to explain medium effects of QGP.

3. Experimental Approach

The LHC is located at the CERN ("Conseil Européen pour la Recherche Nucléaire") complex along the Franco-Swiss border near Geneva. At the moment, it is the largest and highest-energy particle accelerator in the world and it is designed as a synchrotron in a ring of 27 km circumference. In the LHC, bunches of protons are accelerated in two different beams, one of them running clockwise and the other one running anticlockwise. The design energy of such a proton beam is 7 TeV. Additionally to protons, beams of lead-nuclei are accelerated to reach higher energy-densities in a collision. There are four different Ineraction Points (IP) where two beams are collided. Around these IPs, the particle detectors ALICE, ATLAS ("A Toroidal LHC ApparatuS"), CMS ("Compact Muon Solenoid") and the LHCb ("Large Hadron Collider beauty") experiment are constructed to measure the results of the particle collisions. The first beam in the LHC has been produced in September 2008 and the first collision occurred in November 2009. [CER23a] [CER23b]

3.1. The ALICE Experiment

For this thesis, data from the ALICE detector [ALI08] [ALI14] is used that has been taken in Run 1 and Run 2 of the LHC. The detector is specialised on the measurement of heavy-ion collisions to study the formation of QGP under extreme energy densities and temperatures.

ALICE has an overall dimension of $16 \times 16 \times 26\,\mathrm{m}^3$ and contains a central barrel part and a forward muon spectrometer. Figure 10 portrays the original detector setup. It also includes a zoom into the most central detector part, the Inner Tracking System (ITS), where the ALICE coordinate system is specified. The beam pipe is orientated along the z axis pointing towards the A side with the IP in the origin of the coordinate system. Perpendicular to the beam pipe are the x axis pointing horizontally to the accelerator centre and the y axis pointing upwards. The azimuthal angle ϕ increases counter-clockwise from $x\,(\phi = 0)$ to $y\,(\phi = \frac{\pi}{2})$ and the polar angle θ increases clockwise from $z\,(\theta = 0)$ to $-z\,(\theta = \pi)$. [BC03]

The forward muon arm is located in negative z direction, covering a pseudorapidity range of $-4.0 < \eta < -2.5$ and the full azimuth. It contains several small detectors for global particle analysis and triggering. Among others, the Zero Degree Calorimeter

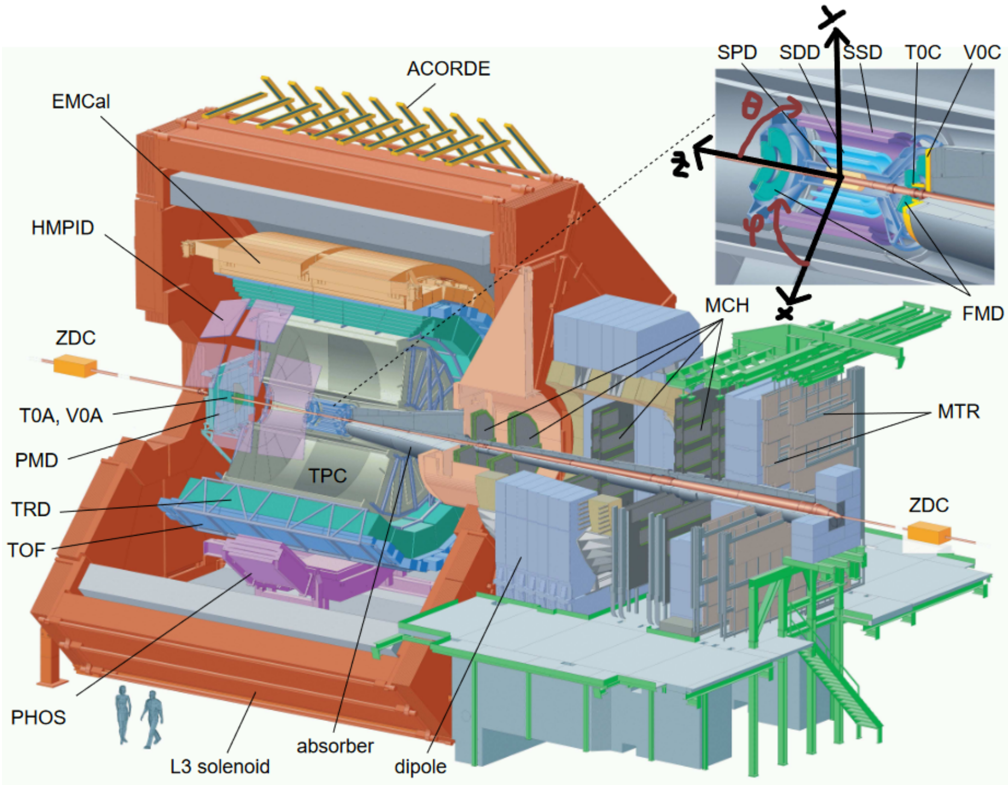

Figure 10: Schematic picture of the ALICE detector with a central barrel part and a forward muon spectrometer. A large solenoid magnet contains the central barrel detector parts: ITS, TPC, TRD, TOF, PHOS, EMCal, and HMPID. It also depicts the forward detectors PMD, FMD, V0, T0, and ZDC. A zoom into the ITS indicates the components of the ITS and the ALICE coordinate scheme including the angles ϕ and θ. Taken from [ALI14] fig. 1, modified.

(ZDC) is used to find the number of participants in a heavy-ion collision. Moreover, the $V0$ detector provides triggers for the analysis in the central barrel detectors and it is used to determine the centrality of an event via multiplicity measurement. Both systems will be further explained in section 3.1.5.

The central barrel part of the ALICE detector is also shown in fig. 11. Located in the middle of the detector is the beam pipe, surrounded by the ITS. Going outwards, one finds the Time-Projection Chamber (TPC), the Transition Radiation Detector (TRD) and the Time-Of-Flight (TOF) detector, which cover the full azimuth angle. Even further away from the IP are some detectors that do not cover the full azimuth, namely the High Momentum Particle Identification Detector (HMPID) and two electromagnetic calorimeters: the PHOton Spectrometer (PHOS) and the ElectroMagnetic Calorimeter (EMCal). Each of these subsystems is dedicated to measure different types of particles

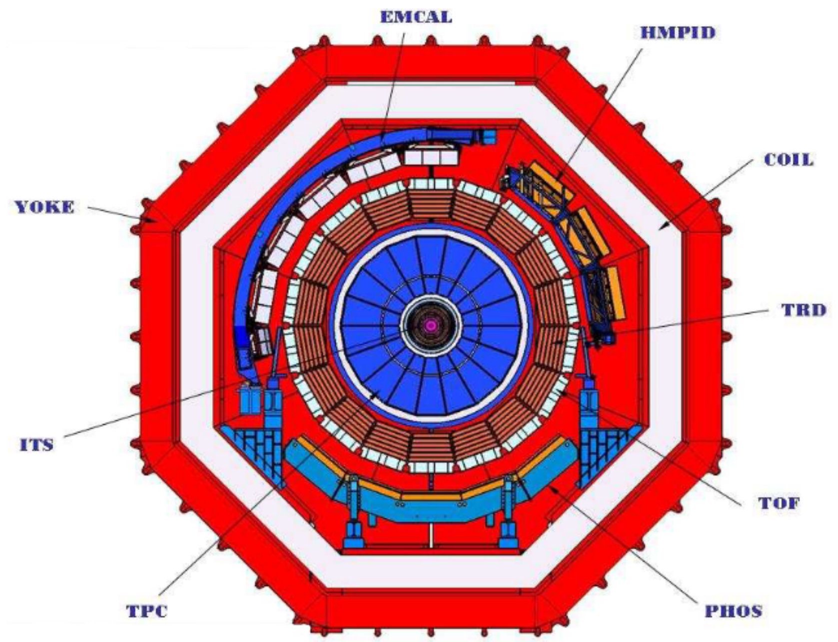

Figure 11: 2D cut through the central barrel part of the ALICE detector along the xy direction. Taken from [ALI08] fig. 1.2.

resulting from the collision in order to analyse the whole process. The whole barrel is embedded in a solenoid magnet. [ALI08]
While the TRD, EMCal and PHOS are systems specialised for electron measurement, the identification of hadrons is mainly performed in the ITS, TPC, TOF and HMPID. As the latter is the most important in the scope of this thesis, the four systems dedicated to hadron identification will be further explained in the following sections. [ALI14]

3.1.1. Inner Tracking System (ITS)

The main tasks of the ITS are to localise the primary vertex and to reconstruct possible secondary vertices. It is also used for identification and tracking of particles with a momentum below 200 MeV.
In order to do so, the original ITS consisted of 6 cylindrical layers of silicon detectors which were constructed around the beam pipe. The first two layers were realised as Silicon Pixel Detectors (SPD) and were located at a radius of 3.9 cm from the z-axis. The following two layers consisted of Silicon Drift Detectors (SDD) and the two outermost layers of Silicon Strip Detectors (SSD). Overall, the ITS had a radius of 43.6 cm. An illustration of all six layers is given in fig. 12.

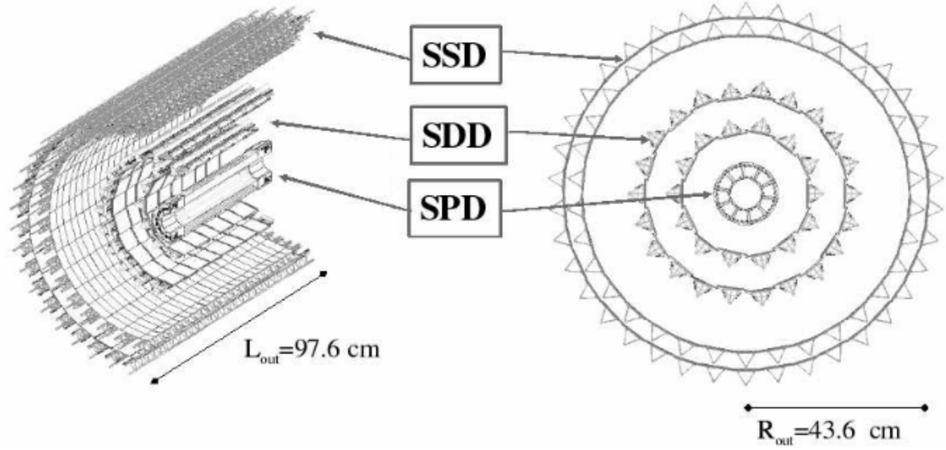

Figure 12: Sketch of the ITS layers and their distance to the beam pipe. Taken from [ALI08] fig. 3.1.

Together, the four outer layers were measuring the ionisation energy loss of particles traversing the detector. For each layer, a dE/dx value was obtained which was used for particle identification in a pseudorapidity interval of $|\eta| < 0.9$. The pseudorapidity coverage of the inner two layers was with $|\eta| < 1.98$ more extended for a continuous coverage of charged-particle multiplicity measurement.
After Run 2, the ITS was upgraded to seven layers of monolithic active pixel sensors and the first layer is constructed closer to the beam pipe with a distance of 2.3 cm. The primary goals are to improve the reconstruction of primary as well as secondary vertices and a more accurate detection of low-p_T particles. [Rei22]

3.1.2. Time Projection Chamber (TPC)

The TPC is a cylindrical field cage filled with $90\,m^3$ of $Ne/CO_2/N_2$. Until Run 2, multi-wire proportional chambers were mounted at the end plates for readout. In total, the TPC has a length of 5 m in beam direction with an inner radius of 85 cm and an outer radius of 250 cm.
Particle Identification in the TPC is obtained through a simultaneous measurement of the specific energy loss, charge and momentum of each particle. Thus, it enables tracking and identification of particles over a wide momentum range between $0.1\,\mathrm{GeV} < p_T < 100\,\mathrm{GeV}$ and for a pseudorapidity interval of $|\eta| < 0.9$.

3.1.3. Time-Of-Flight Detector (TOF)

Constructed as a cylindrical shell at a radius between 370 cm and 399 cm, the TOF detector provides particle identification via time-of-flight measurements. Traversing charged particles ionise the detector gas and thus produce a gas avalanche process from which the observed signals are obtained. As an example, in Pb–Pb collisions at a centrality below 70 % the overall time resolution for pions at 1 GeV reaches 80 ps.
Particle identification in TOF is optimised for momenta below 2.5 GeV for pions and kaons and $p < 4$ GeV for protons. The detector is covering a pseudorapidity range of $|\eta| < 0.9$ and the full azimuth. Coupled with ITS and TPC, it provides event-by-event identification for large amounts of pions, kaons, and protons.

3.1.4. High Momentum Particle Identification Detector (HMPID)

The HMPID is a single-arm array containing ring imaging Cherenkov detectors and is located at a radial position of 5 m. It was aimed to extend the track-by-track particle identification in ALICE to higher transverse momenta, up to 3 GeV for pions and 5 GeV for protons. The pseudorapidity coverage is $|\eta| < 0.6$ and the azimuthal coverage $1.2° < \phi < 58.8°$.

3.1.5. ZDC and V0 Detector

An important observable in AA collisions is the number of participant nucleons. The ZDC measures the number of spectators to derive the participants and the collision energy (as mentioned in section 2). To do so, it is placed at a distance of 116 m at both sides of the IP. Each ZDC contains a detector for neutrons (ZN) located between the beam pipes and a detector for protons (ZP) located outside of the outgoing beam. Additionally, electromagnetic calorimeters (ZEM) are placed at 7 m from the IP to measure the energy of emitted particles and thus distinguish between central and peripheral collisions. The location of the detectors on the side of the beam line opposite to the muon arm (in positive z direction) is also illustrated in fig. 13.
The V0 detector consists of two scintillator counters called V0A and V0C which are used for multiplicity measurements, located at either side of the IP. The V0C detector is placed on the side of the muon spectrometer at a distance of 90 cm to the IP and covers a pseudorapidity range of $-3.7 < \eta < -1.7$. Similarly, the V0A detector is placed on

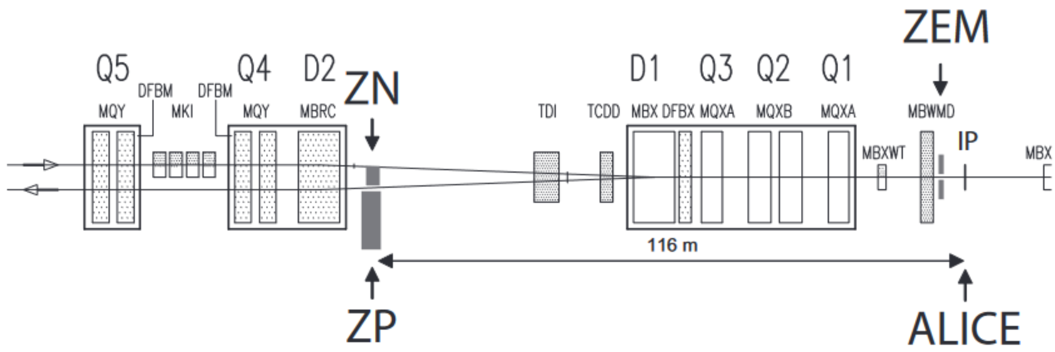

Figure 13: Top view on the beam line opposite to the muon arm showing the position of ZN, ZP and ZEM. Dipole (Dx) and quadrupole (Qx) magnet positions are also indicated. Taken from [ALI08] fig. 5.1.

the opposite side at a distance of 340 cm from the IP with a coverage of $2.8 < \eta < 5.1$. Together, the charged-particle multiplicity measured in V0A and V0C can be used as an indicator for the centrality of a heavy-ion collision. The most central events are assigned to the events with the highest multiplicity and the most peripheral events to the ones with the lowest multiplicity. Furthermore, the V0 detector serves as a Minimum-Bias (MB) trigger for the central barrel detectors. The term "minimum-bias" refers to an event class that has been selected with the smallest possible selection bias. The $\mathrm{MB_{or}}$ trigger requires a signal in either V0A, V0C or SPD, while the $\mathrm{MB_{and}}$ trigger requires a signal in both V0A and V0C. [ALI08] [ALI14]

3.2. Datasets

In this thesis, several datasets are used as comparison to the results of an MC event generation with PYTHIA.

Data about the multiplicity distributions in pp events have been published in 2017. These data are available at different energies and for different pseudorapidity intervals and are given for three different event classes in pp collisions. While the INEL class includes all inelastic events that were triggered by the $\mathrm{MB_{or}}$ trigger, the INEL>0 class requires an additional hit in the region $|\eta| < 1$. Moreover, the third class includes all events that were triggered by the $\mathrm{MB_{and}}$ trigger to remove most Non-Single Diffractive (NSD) events and is therefore called the NSD event class. In the following, only the INEL event class has been analysed at a Centre-of-Mass (CM) energy of $\sqrt{s} = 7\,\mathrm{TeV}$

and with a selection according to $|\eta| < 2$. [Col17]
In 2018, ALICE data have been published for transverse-momentum spectra of charged particles in inelastic pp, NSD p–Pb and Pb–Pb events at energies per colliding nucleon pair of $\sqrt{s_{\mathrm{NN}}} = 2.76\,\mathrm{TeV}$ and $\sqrt{s_{\mathrm{NN}}} = 5.02\,\mathrm{TeV}$ requiring the $\mathrm{MB_{and}}$ trigger. In this thesis, the latter energy value will be analysed for all three kinds of collisions. The spectra from Pb–Pb collisions are divided into nine different centrality classes and all datasets cover a pseudorapidity interval of $|\eta_{\mathrm{lab}}| < 0.8$. [ALI18]
Data for the transverse-momentum spectra of identified pions, kaons, and protons in pp, p–Pb (and Pb–Pb) events have been published in 2016 (2020). The pp data have been acquired from inelastic pp collisions at $\sqrt{s} = 5.02\,\mathrm{TeV}$ using the $\mathrm{MB_{and}}$ trigger and $\sqrt{s} = 7.0\,\mathrm{TeV}$ using the $\mathrm{MB_{or}}$ trigger for a rapidity interval of $|y_{\mathrm{CMS}}| < 0.8$. Similarly, Pb–Pb data are obtained from collisions at $\sqrt{s_{\mathrm{NN}}} = 5.02\,\mathrm{TeV}$ requiring a signal from the $\mathrm{MB_{and}}$ trigger and sampling the same rapidity interval as for pp collisions. In contrast to that, there are two different datasets available for p–Pb events: one for NSD p–Pb collisions and one for p–Pb collisions divided into different V0A multiplicity classes. Still, both datasets are given at an energy of $\sqrt{s_{\mathrm{NN}}} = 5.02\,\mathrm{TeV}$ and for a rapidity interval of $-0.5 < y_{\mathrm{CMS}} < 0$. [ALI16] [ALI20]
Finally, a paper from 2022 includes data for the mean transverse-momentum $\langle p_{\mathrm{T}} \rangle$ per event in dependence of the corresponding number of final charged particles. These charged particles were selected to have a momentum between $0.15\,\mathrm{GeV} < p_{\mathrm{T}} < 10\,\mathrm{GeV}$ and a pseudorapidity of $|\eta_{\mathrm{lab}}| < 0.8$. Additionally, each event was required to fulfil the $\mathrm{MB_{and}}$ trigger condition. In total, the $\langle p_{\mathrm{T}} \rangle$ measurements have been conducted in pp, p–Pb, Xe-Xe and Pb–Pb collisions at energies between $\sqrt{s_{\mathrm{NN}}} = 2.76\,\mathrm{TeV}$ and $\sqrt{s_{\mathrm{NN}}} = 13\,\mathrm{TeV}$ In this thesis, however, only the measurement from pp collisions at $\sqrt{s} = 5.02\,\mathrm{TeV}$ will be compared with data from PYTHIA. [Col22a]

4. Monte-Carlo Event Generation

In high-energy particle physics, an event consists of a large number of particles which are created in different processes after a collision of two high-energetic particles. Most of these processes can not be calculated by using perturbation theory. Instead, an event can be generated in a computer simulation to predict properties in the experimental data. These properties vary from event to event due to the random nature of quantum processes in particle collisions. Hence, the event generation is implemented by using the Monte-Carlo method for the creation of large samples of random sequences by following the probability distributions of the involved processes. Moreover, such a MC event generator is based on calculations from perturbation theory as well as on phenomenological models.

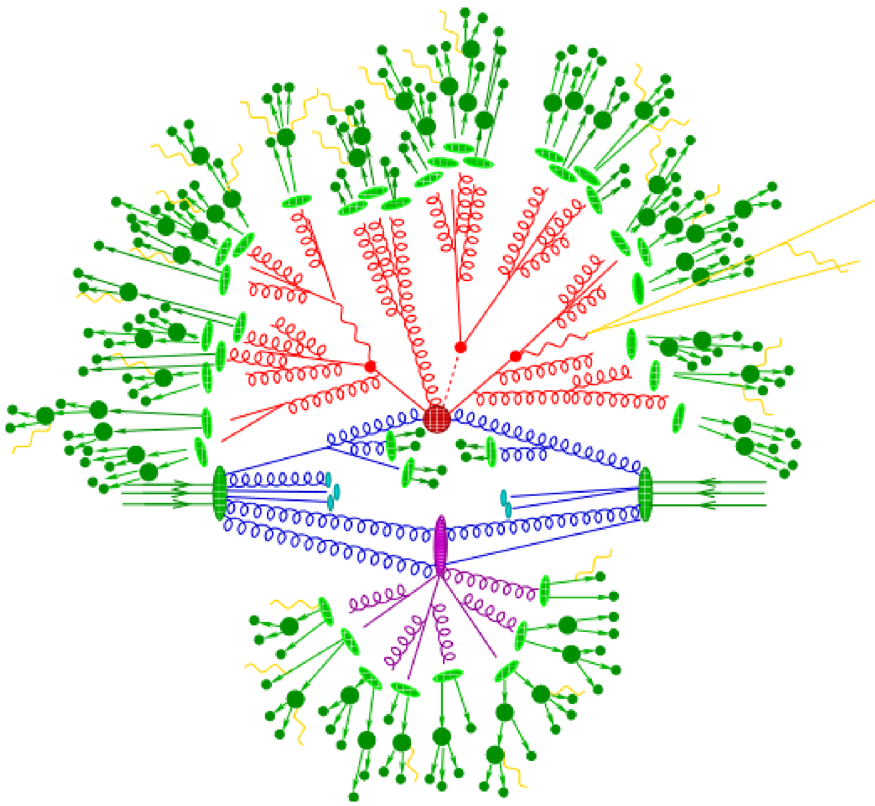

Figure 14: Illustration of a hadron-hadron collision simulated by a MC event generator. The hard-scattering process is displayed as a dark red circle and a second hard process is shown as a purple oval. Resulting partons are propagated in parton showers, portrayed in blue (ISR) and red (FSR). Light green ovals indicate the fragmentation of partons into hadrons while dark green circles denote hadron decays or final-state hadrons. The yellow lines represent soft photon radiation. Taken from [Höc15] fig. 3.

Figure 14 depicts the different steps in the generation of a hadron-hadron collision event. The initial partons radiate and scatter inside the projectiles which is called “Initial State Radiation” (ISR). In the collision, two partons from each one of the colliding hadrons perform the hard-scattering process at the hardest momentum scale in the process. Other partonic interactions at softer momentum scales are summarised under the term “MultiParton Interactions” (MPIs). The resulting partons radiate and scatter again which is referred to as “Final State Radiation” (FSR). Both ISR and FSR are modelled as parton showers. At the hadronisation scale ($\sim 1\,\mathrm{GeV}$), coloured partons fragment into hadrons and after the decay of unstable particles, a full event has been generated.
This section gives an overview over the PYTHIA general-purpose Monte-Carlo event generator and the Angantyr framework as an addition to PYTHIA. While the former is mainly used for lepton-lepton, lepton-hadron and hadron-hadron collisions, the latter is specialised for collisions of heavy ions. The latest version which has been used for all calculations in this thesis is PYTHIA 8.306. [Bie+22] [Höc15]

4.1. PYTHIA Event Generator

The program structure in PYTHIA is divided into three main parts which will be presented in more detail in the following subsections. Here, only the simulation of pp collisions will be discussed because this is the collision type being analysed and compared to the data of ALICE in this thesis.
In the process level, the hardest sub-process (i.e. the process with the highest momentum transfer Q^2) is defined and short-lived resonances are produced. Interactions at less hard momentum scales (MPIs) are managed in the parton level, as well as parton showers modelling ISR and FSR. Finally, in the hadron level, all partons are hadronised into colour-singlet states using the Lund String Model. Additionally, the decay of unstable hadrons is performed at this stage. The resulting hadronic structure forms a realistic event as it could be observed in a detector.

4.1.1. Process Level

The process level defines the overall nature of a simulated particle collision. An interaction between each one parton of the colliding hadrons forms the hardest sub-process that can be calculated at leading order perturbation theory. Furthermore, a second hard process as portrayed in fig. 14 can occur.
Internal hard QCD processes are divided into $2 \to 2$ or $2 \to 3$ scatterings with light quarks and gluons and the production of heavy flavours in $2 \to 2$ processes. Additionally, PYTHIA contains electroweak and several other processes, including theories Beyond the Standard Model (BSM). However, this thesis focuses on soft QCD processes without selection bias which have already been described in section 2.4.
Due to the high momentum transfer Q^2 in the hard scattering process, short-lived particle states like Z, $W^{\pm}$, t or the Higgs boson can be produced. Consequently, these particles have to be classified and their decay has to be performed by PYTHIA. Therefore, unstable particles can be identified by the following conditions:

1. if the lifetime is below the hadronisation time (particularly for coloured particles)
2. if the partial and total widths can be calculated perturbatively, such as for μ, Z, $W^{\pm}$, t, Higgs, and most BSM particles
3. if a particle can only be produced in the hard process, such as Z, $W^{\pm}$, t, and Higgs

Internally, PYTHIA differentiates between resonances, particles and partons. By default, all BSM states are considered resonances. Additionally, all states with a rest mass above 20 GeV like Z, $W^{\pm}$, t or the Higgs boson are treated as resonances. Their decay is directly performed during the hard process. However, this does not include hadrons or particles that can be produced in hadron decays, which PYTHIA considers as particles. Similarly, states like a J/Ψ that can be produced in the hard process but also in hadronisation and particle decays are considered particles and not resonances. Finally, quarks and gluons are treated as partons carrying a colour charge and must thus be confined. All unstable particles are then decayed after the hadronisation.

4.1.2. Parton Level

In the parton level, the modelling of MPIs is intertwined with parton showers.
As hadrons are composite objects, several parton pairs can collide in one event. These partonic sub-collisions (or MPIs) are modelled as separate $2 \to 2$ scatterings. They are generated in addition to the hard process at rather soft momentum scales and form the so-called "underlying event". Particle production due to semiperturbative MPIs leads to larger multiplicities and a larger amount of transverse energy in the event.
An example event with two sub-scatterings (one in red and one in black) which are assumed to be $gg \to gg$ processes is shown in fig. 15. In principle, all incoming and outgoing partons would also undergo ISR and FSR but for clarity this has been removed from the illustration. If the two sub-processes are completely uncorrelated (case a), the gluon strings of both scattering processes are stretched out to the beam remnants. This would lead to particle production over the whole available rapidity range also for the secondary scattering. However, the increased multiplicity of soft particles due to stretched out gluon strings in several interactions is not reproduced in the measured data. Hence, most sub-processes in the MPI model are colour-connected to partons resulting from previous scatterings which corresponds to cases b or c in fig. 15.
Parton showers are used in PYTHIA as an intermediate step from the hard momentum scale of the hardest process down to the hadronisation scale. Since the partonic structure generated in such processes is too complicated to be calculated directly, a shower algorithm is applied to a small amount of partons. These showers describe how the partons resulting from the hard process successively reach softer "softer" (smaller momentum transfer) and more "collinear" (smaller angles) resolution scales. They are defined recursively until a limit near the hadronisation scale and the number of partons is increased in each step to build up a realistic partonic structure.
Among parton showers, one differentiates between two kinds: ISR and FSR. As mentioned before, ISR appears before the hard process within the projectile hadrons and FSR afterwards between the outgoing partons. They are also referred to as spacelike and timelike due to the nature of modelled off-shell intermediate particles. The most virtual particles are the ones with the shortest lifetime and exist close to the hard process. Starting from there, showers stretch forwards (FSR) or backwards (ISR) in time with decreasing virtualities.

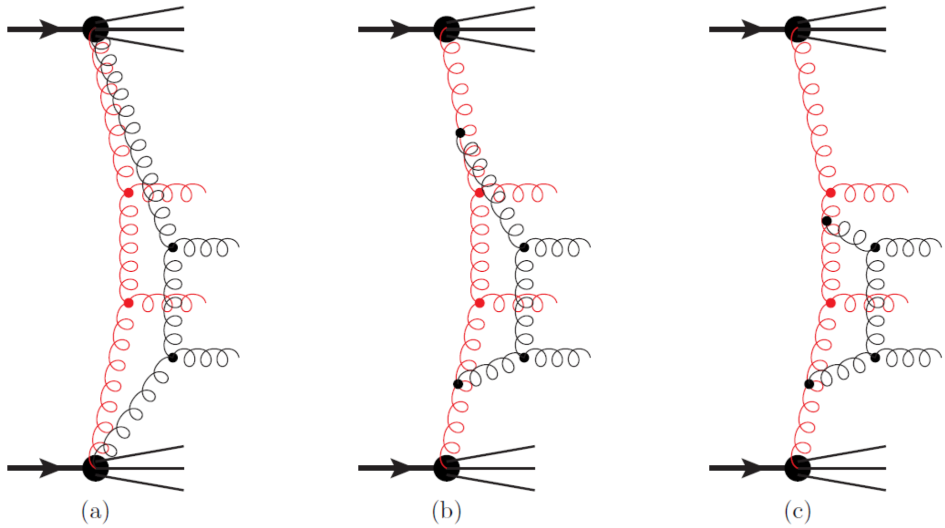

Figure 15: Schematic presentation of MPIs in a pp collisions. The vertical axis represents the spanned rapidity range between the colliding protons. Parton showers are not included for simplicity. In (a) both sub-scatterings are directly colour-connected to the two proton beam remnants, while in (b) and (c) the secondary scattering is colour-connected to the primary one. Taken from [Bie+18] fig. 2.

4.1.3. Hadron Level

Due to confinement, coloured beam remnants resulting from the parton showers now have to be transformed into colourless hadrons which is performed in the hadron level. In contrast to the processes before, hadronisation is not calculable via perturbation theory because of its low energy scale of about 1 GeV. Hence, the implementation of this process has to rely on phenomenological models. In PYTHIA, it is based on the Lund string model which was already presented in section 2.2.1.

After hadronisation in the Lund model is finished, unstable particles have to be decayed. As described before, the decay of resonances produced in the hardest process has already been performed, but states that are treated by PYTHIA as particles are decayed in this step. One of the experimentally known decay channels is chosen randomly according to a weight which is proportional to the branching ratio of the decay channel. If some of the decay products are again unstable (on the time scale that is required to detect outgoing particles), this process continues until a set of final-state particles is generated as it could be observed in a detector.

By simulating an event in PYTHIA, some decay channels might be manually forbidden. In that case, decay products are chosen from the channels that are left open. A user might also set a limit $\tau_{0,\max}$ for a particle's lifetime. In that case, only the particles with a lifetime $\tau_0 < \tau_{0,\max}$ are decayed. All other particles are considered stable.
A possible downside of hadronisation in the Lund model is that it describes the fragmentation of an isolated string. This would presuppose that the numerous partons produced in a high-energy hadron-hadron collision are hadronised independently which might be inaccurate. Indeed, parton showers might lead to overlapping strings during hadronisation which might cause similar collective effects as the ones presented in section 2.5.3 for the creation of QGP. These collective effects that are traditionally assigned to heavy-ion collisions have also been observed experimentally in pp collisions and in data from the Large Electron-Positron (LEP) collider. Instead of assuming that QGP is actually formed, one attempt to account for these effects is to introduce interactions between overlapping strings to the Lund model. However, such approaches are still work in progress and only one possible explanation among others for the observed effects.
In this thesis, the so-called "string shoving model" is used as an extension of the Lund model. Instead of treating strings as massless with no transverse extension, this model tries to explain collisions between strings in densely populated regions of space. All components included in this model are the string shape, its transverse width and the interaction force between two strings. The shoving force mainly originates from the repulsion between strings and is distributed among outgoing hadrons, leading to a transversal momentum push Δp_{T}. [Bie+22]

4.2. Angantyr Model for Heavy-Ion Collisions

Angantyr [Bie+18] is a model in PYTHIA which is used for the description of high-energetic pA or AA collisions. For that, complete exclusive hadronic final states are being extrapolated from the simulation of pp collisions. Similar to PYTHIA, Angantyr does not include the creation of QGP in a heavy-ion collision. It is thus only possible to study the non-collective behaviour of physical observables in Angantyr.
To generalise the event generation from pp collisions to pA or AA collisions, several steps are required. Firstly, the positions of nucleons inside the nuclei have to be identified. Several MC generators are existing which generate nucleon distributions. A common approach is to position the nucleons according to a Woods-Saxon potential which de-

scribes the probability for a nucleon being located at a certain distance from the nucleus centre. Additionally, effects of NN correlations have to be taken into account. Further details are given in [ADS09].

Next, the numbers N_{part} of participating or wounded nucleons and N_{coll} of binary Nucleon-Nucleon collisions have to be determined. This is done via the Glauber formalism as presented in section 2.5.2. Although fluctuations in the nucleon positions have been neglected in the original Glauber Model, they have been found to be essential for the final-state properties of an event. In Angantyr, diffractive excitation (a consequence of these fluctuations) is therefore included through the Good-Walker formalism. As already mentioned, diffraction is modelled as a colour neutral exchange of pomerons.

After the number of participating nucleons is calculated, the contribution of the wounded nucleons to the final-state properties has to be estimated. The procedure in Angantyr is based on the old FRITIOF program and the “wounded nucleon” model. In that model it was assumed that each wounded nucleon contributes to the multiplicity distribution of the final state according to an emission function $F(\eta)$ which has to be found from measured data and depends on the centrality of the collision. The final-state multiplicity is then given by

$$\frac{dN_{\mathrm{ch}}}{d\eta} = N_{\mathrm{part,p}} \cdot F(\eta) + N_{\mathrm{part,t}} \cdot F(-\eta) \tag{17}$$

where $N_{\mathrm{part,p}}$ and $N_{\mathrm{part,t}}$ are the respective numbers of participating nucleons in the projectile and target nucleus.

Instead of assuming that each wounded nucleon results into a string and is hadronised, an event in Angantyr is generated through multiparton interactions. Section 4.2.1 describes how different NN interactions are processed by using the PYTHIA MPI machinery.

In a last step, these NN sub-events have to be combined to one parton level AA event. The according procedure is presented in section 4.2.2. The hadronisation and decay of unstable particles is then handled by PYTHIA as already described in section 4.1. Finally, a full heavy-ion event has been generated.

4.2.1. Contribution of Participating Nucleons to the Final State

Once the number of wounded nucleons is found, one needs to estimate how each of these nucleons contributes to the final particle distribution in the event.
Firstly, the somewhat easier case of a pA collision will be discussed. An example is shown in fig. 16, where the projectile proton is assumed to interact with two target nucleons via $gg \to gg$ processes. Analogous to fig. 15, additional parton showers are not indicated to keep the illustration uncluttered. In case (a), there is a primary scattering between the proton and one target nucleon which is colour connected to (a) secondary scattering with the other target nucleon. Hence, both target nucleons are absorptively wounded. In case (b), the secondary scattering is pictured as a separate single diffractive excitation process. This is modelled in PYTHIA by a colour-neutral exchange of pomerons, here displayed as a green zigzag line. According to section 2.4, there is no particle production in the region of a colour neutral pomeron exchange. Cases (a) and (b) are thus leading to the same particle distribution in the final state.

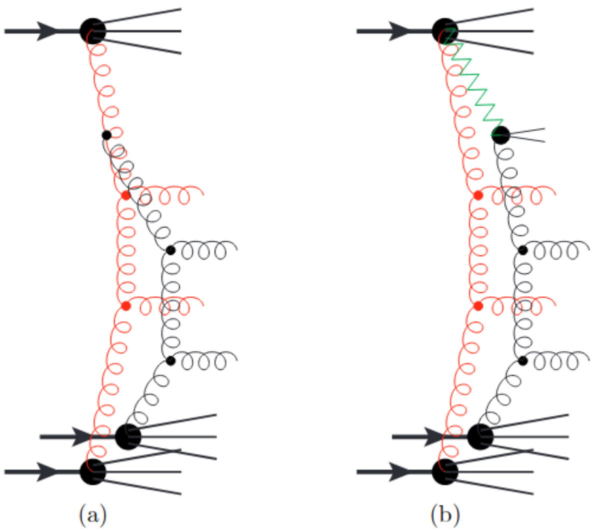

Figure 16: Depiction of two sub-scatterings between one projectile and two target nucleons. The vertical axis represents the spanned rapidity range between the colliding nucleons. Parton showers are not included for simplicity. In (a) the secondary process is colour-connected to the first one. In (b) the green zigzag line represents a pomeron exchange in the secondary interaction which leads to a diffractively excited second target nucleon. Taken from [Bie+18] fig. 3.

Therefore, a secondary interaction can be implemented as if it was a separate single diffractive excitation of an additional imaginary projectile proton while the primary interaction can be modelled as a normal nondiffractive scattering. Potential additional multiparton scatterings are also included as multiple scatterings in the generation of the single diffractive event. This is the way how Angantyr deals with multiple NN interactions to simplify the calculations.

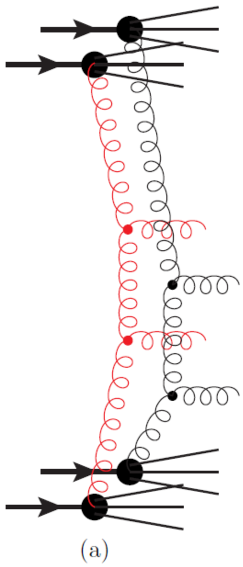

Figure 17: Illustration of an interaction between two projectile and two target nucleons. In (a) the two scattering processes are independent. In both (b) and (c) there is one primary scattering and the secondary interactions are diffractively excited through a pomeron exchange. Taken from [Bie+18] fig. 4.

The treatment of NN collisions in an AA event is conceptually similar. Figure 17 pictures three possible cases to model an interaction between each two nucleons from the projectile and the target nucleus. Again, parton showers are not included for clarity. Case (a) presents two separate absorptive interactions while the other cases include each one primary and two secondary processes which are correlated. The secondary interactions are here shown in black and in blue and are both single diffractive processes. In case (b), both secondary processes are coupled via pomeron exchange to the primary scattering and in case (c), the first secondary interaction is directly coupled to the other one. Again, all three cases contribute in the same way to the final state and secondary scatterings are modelled as if they were a single diffractive excitation event.

A way to classify these different processes and combine all NN collisions to one AA event is outlined in the next subsection.

4.2.2. Combination of Nucleon-Nucleon Sub-events

In a heavy-ion collision, each projectile and target nucleon can undergo multiple interactions. All of these interactions have to be generated as a NN parton level sub-event by PYTHIA and then combined to one parton level AA event.
Firstly, all NN interactions that have been determined by the Glauber formalism are put in a list. This list is sorted with increasing nucleon-nucleon impact parameter

$$\vec{b}_{\mu\nu} = \vec{b}_{\mu} + \vec{b} - \vec{b}_{\nu} \tag{18}$$

which represents the relative separation between the colliding nucleons μ and ν. Here, $\vec{b}_{\mu}$ and $\vec{b}_{\nu}$ stand for the distances of the corresponding nuclei to the centre of the nucleus and $\vec{b}$ is the impact parameter of the heavy-ion collision.
In a first iteration over this list, only absorptive interactions are taken into account. A sub-event is generated by PYTHIA for each selected list entry and both nucleons are labelled as already interacted. If neither nucleon has been part of an interaction before, the process is considered "primary" and is created as an inelastic non-diffractive minimum-bias event. Otherwise, it is called a "secondary" interaction. These are only generated once all primary scatterings are dealt with. Also, the implementation of such a process follows the description in section 4.2.1, where the secondary scattering is modelled as a separate single diffractive process. In this case, the final state produced by PYTHIA is added to the connected primary absorptive sub-event and the additional proton which has been included to implement the diffractive excitation is removed.
Afterwards, a similar process is used to simulate diffractive processes. Primary diffractive scatterings are generated first, then secondary ones. However, a nucleon that has already interacted can not be further excited. If such a nucleon is supposed to be excited in a diffractive interaction, the process is instead modelled as an elastic scattering. Once all absorptive and diffractive processes have been generated, a last iteration takes care of the remaining elastic interactions.
Finally, one parton level sub-event has been produced for each NN interaction. This set is then combined to one parton level AA event and the non-participating nucleons of projectile and target are labelled as beam remnants. In a last step, the hadronisation of outgoing particles and their decay is performed by PYTHIA in the same way as for pp collisions resulting into a complete exclusive hadronic final state of an heavy-ion event.

5. Data Analysis

The data analysis is divided into three different kinds of events: (i) pp, (ii) p-Pb, and (iii) Pb-Pb collisions. For all three collision types, simulated p_T-spectra from PYTHIA are compared with the datasets described in section 3.2.
For this purpose, the settings that are applied to the MC event generation are shown in section 5.1. Afterwards, the data resulting from pp collisions are analysed in section 5.2. This gives a first overview of how well PYTHIA reproduces ALICE data. Building on this, section 5.3 and section 5.4 include results from simulations of p–Pb and Pb–Pb collisions.
In all three collisions types, the simulated p_T-spectra will be presented for all charged particles as well as for identified charged pions, kaons, and protons. In collisions including heavy ions, these spectra are also discussed for different centrality classes. Moreover, the effects of including the string shoving model (presented in section 4.1) are analysed in all three cases. This is used to take possible collective-like effects into consideration.

5.1. PYTHIA Setup

This section gives an overview of the settings that are applied to the PYTHIA event generation in this thesis.
All simulations were performed by using the default Monash 2013 tune. For generating pp events, the *SoftQCD:inelastic* flag was set to compare with the INEL event class. This activates all inelastic processes from eq. (8). For p–Pb and Pb–Pb collisions, the *SoftQCD:all* flag was applied which includes also elastic processes. However, the results of p–Pb collisions were filtered for NSD events, which means that all single diffractive events were discarded. A limit in lifetime for particle decays was also added via the *ParticleDecays:limitTau0* flag to match the ALICE definition of primary charged particles (see section 2.3.2). In that case, only the decay of particles with a lifetime τ_0 smaller than $\tau_{0,\max} = 10\,\text{mm}$ is performed. Additionally, the effects of including string shoving are tested by switching on the *Ropewalk:RopeHadronization* and *Ropewalk:doShoving* flags.
A special characteristic of p–Pb collisions is the asymmetry between proton and lead beam. This asymmetry introduces a rapidity shift between the laboratory frame and the nucleon-nucleon Centre-of-Mass System in the direction where the lead beam is going.

Conventionally, this is in positive η_{lab} direction, while the proton beam is going in direction of negative η_{lab}. This is modelled in PYTHIA by setting the first incoming particle to *Beams:idA* = 1000822080, the particle id code of ^{208}Pb. Accordingly, the second incoming particle is modelled as a proton by setting its particle code to *Beams:idB* = 2212. For high-p_{T} particles, η and y agree. Hence, the pseudorapidity coverage

$$\eta_{\text{CMS}} = \eta_{\text{lab}} + \Delta y_{NN} \tag{19}$$

in the CM frame is shifted in relation to the laboratory frame by a factor of $\Delta y_{NN} = 0.465$. Thereby, a detector coverage of $|\eta_{\text{lab}}| < 0.8$ in a p–Pb collision roughly corresponds to $-0.3 < \eta_{\text{CMS}} < 1.3$. [ALI18] [Col22b]

5.2. Results from pp Collisions

Colliding two protons is the simplest of the three collision types that are discussed in this thesis. Simulations of such pp collisions in PYTHIA can be compared with experimental data to determine how accurately certain observables are reproduced in PYTHIA. This will later be used as a basis for the analysis of heavy-ion events.

In this chapter, there are two types of simulated observables that are compared with their experimental counterparts. Firstly, section 5.2.1 includes a discussion of transverse-momentum distributions of final-state particles once for all charged particles and once individually for identified pions, kaons, and protons. Secondly, the charged-particle multiplicity is analysed in section 5.2.2. Besides, effects of including the string shoving mechanism in the hadronisation phase of PYTHIA are presented in section 5.2.3 for both of the previous mentioned observables.

5.2.1. Transverse-Momentum Spectra

Transverse-momentum spectra can be used to analyse the production of new particles in a high-energetic particle collision. In the following, p_{T} spectra from PYTHIA simulations will be compared with data from the ALICE detector. The aim is to discuss similarities and differences between particle spectra in MC simulations and experiment.

An example is given in fig. 18 (a). Here, one can see the p_{T}-dependent yield $d^2N/(dp_{\text{T}}d\eta)$

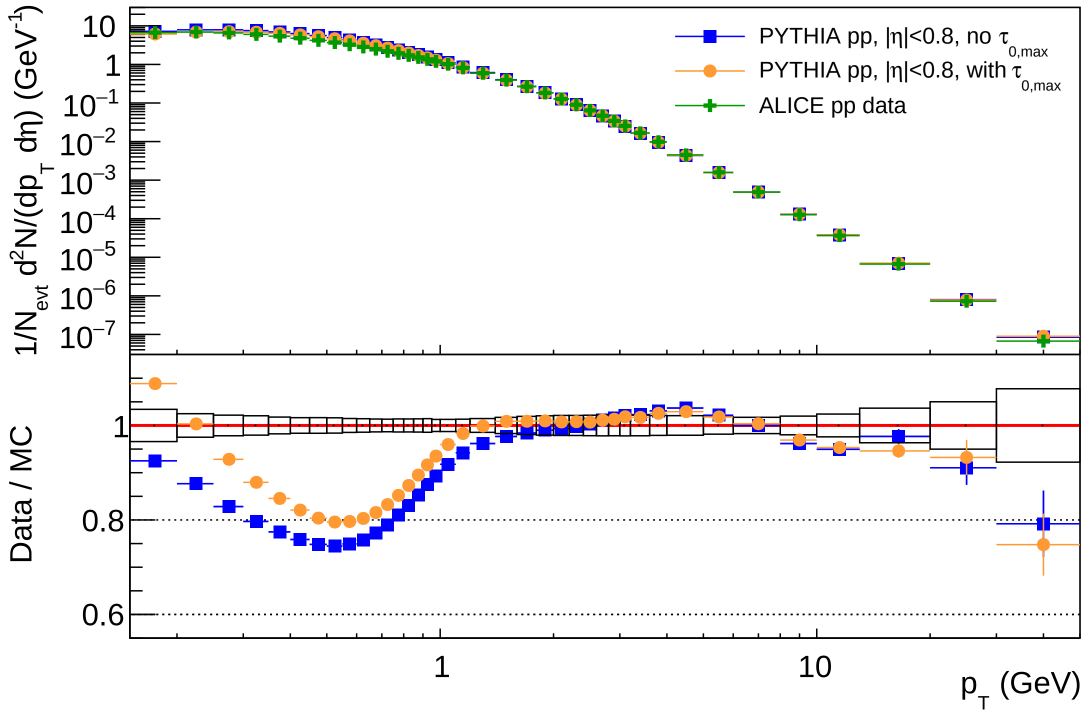

Figure 18: The top panel (a) shows the p_{T} spectra of inelastic pp collisions at $\sqrt{s} = 5.02\,\mathrm{TeV}$ in PYTHIA including final-state charged particles with $|\eta| < 0.8$ with and without $\tau_{0,\mathrm{max}}$. ALICE data from [ALI18] are plotted for comparison. The bottom panel (b) portrays the respective data/MC ratios.

of final-state charged particles normalised by the number of events N_{evt}. In both cases, a hit in both V0A and V0C was required in an event ($\mathrm{MB}_{\mathrm{and}}$ trigger). Furthermore, a pseudorapidity interval of $|\eta| < 0.8$ has been selected for the simulated spectrum in order to reproduce the η range from the measurement in ALICE. Therefore, the simulation is also normalised by the size of this interval and the bin width.

In this plot, yields from inelastic pp collisions at $\sqrt{s} = 5.02\,\mathrm{TeV}$ simulated in PYTHIA are compared with experimental data from [ALI18]. The statistical errors of both spectra are depicted as bars and the systematical errors from the measurement as boxes around the data points. However, the latter are too small to be visible in this plot. In both yields, the most particles carry rather small transverse momenta. From a yield of about $10\,\mathrm{GeV}^{-1}$ around $p_{\mathrm{T}} = 0.3\,\mathrm{GeV}$, the number of particles decreases exponentially to approximately $10^{-7}\,\mathrm{GeV}^{-1}$ at $30\,\mathrm{GeV} \leq p_{\mathrm{T}} \leq 50\,\mathrm{GeV}$. This can be explained by the fact that most processes in the event generation like MPIs and hadronisation are non- or semi-perturbative with rather soft momentum transfer. [Bie+22]

The largest difference between both spectra appears for small p_T. This can be seen more clearly in a ratio of the measured data to the simulated spectrum as plotted in fig. 18 (b). Here, two data/MC ratios are plotted for an event generation with (orange) and without (blue) a $\tau_{0,\max} = 10\,\mathrm{mm}$ cut applied in the event generation. The case where simulation and measurement are identical and the ratio results to unity is indicated by a red line. The systematical errors of the experimental data are illustrated as black boxes around this line while the combined systematical errors from simulation and measurement are plotted as error bars.

In the small-momentum range below $\sim 1\,\mathrm{GeV}$, the ratio without τ_0-limit starts slightly below unity while the other ratio is shifted upwards by about 15 percentage points. With increasing p_T, both curves decrease towards a minimum around $p_T = 0.56\,\mathrm{GeV}$. The respective ratios at these minima are 75 % (with $\tau_{0,\max}$) and 80 % (without the cut) which means that PYTHIA overestimates the creation of low-p_T particles. At higher p_T, both distributions increase again towards unity and the deviation between them decreases further. In the intermediate-momentum range with $1\,\mathrm{GeV} < p_T < 10\,\mathrm{GeV}$, the orange ratio is flatter and has smaller deviations from unity than the blue one. Hence, the PYTHIA simulation with $\tau_{0,\max}$ included mostly agrees with the ALICE data within the respective uncertainties. In the high-momentum range with $p_T > 10\,\mathrm{GeV}$, the statistical and systematical uncertainties grow strongly since there are only very few particles produced with such high energies and they are more difficult to measure. This makes it difficult to make a statement as to whether the simulated spectrum matches the data or not, but for $p_T > 30\,\mathrm{GeV}$, both ratios clearly fall below unity.

Overall, the simulated yield decreases especially for small p_T by applying the limit $\tau_{0,\max} = 10\,\mathrm{mm}$ which leads to an upwards shift in the ratio in comparison to the event generation without τ_0-limit. The biggest difference appears in the first bin and it gets smaller with increasing p_T. For momenta above 2 GeV, both ratios are matching within their uncertainties.

The reason for the decrease in the simulated yield at small p_T is that fewer particles are produced in decays since particles with a lifetime above 10 mm are considered stable. Instead, high-p_T particles originate rather from decays of heavy leptons or bosons with very short lifetimes. These decays are thus not affected by the limit in lifetime.

For the remaining analysis of this thesis, the τ_0-limit will be applied to the MC event generation in PYTHIA since it matches the ALICE definition of primary particles.

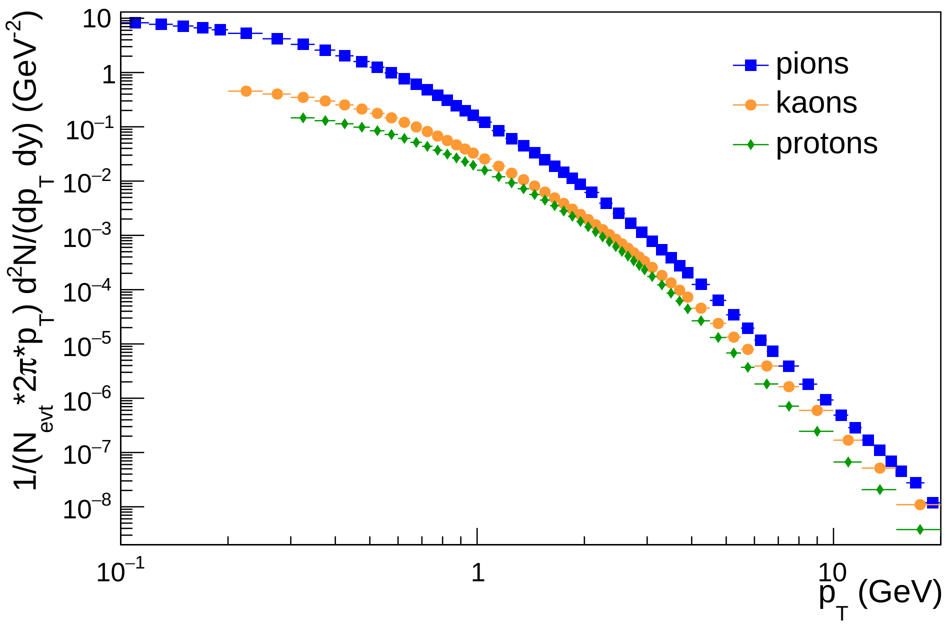

Figure 19: p_{T} spectra of charged pions, kaons, and protons in PYTHIA inelastic pp collisions at $\sqrt{s} = 5.02\,\mathrm{TeV}$ with $|y| < 0.8$, including the limit $\tau_{0,\max} = 10\,\mathrm{mm}$.

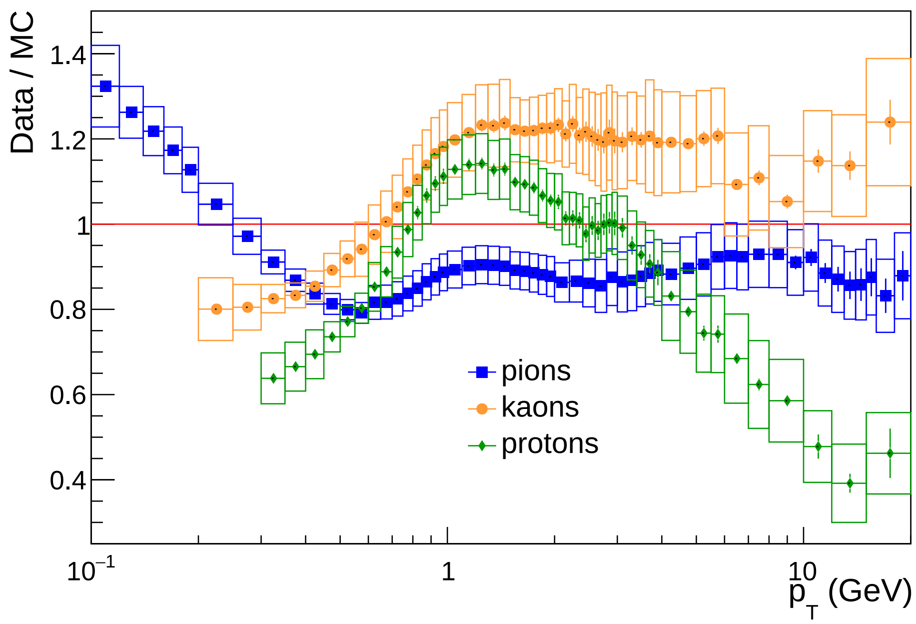

Figure 20: Ratio of p_{T} spectra from charged pions, kaons, and protons in inelastic pp collisions at $\sqrt{s} = 5.02\,\mathrm{TeV}$ with $|y| < 0.8$, including the limit $\tau_{0,\max} = 10\,\mathrm{mm}$. The measured data are taken from [ALI16].

Additionally to the whole spectrum of charged particles in the final state, one can also analyse a specific kind of identified particles. The focus in this thesis lies on the analysis of charged pions, kaons, and protons. In PYTHIA, particle states can be separated by their particle id. Figure 19 displays the yields of charged pions ($\pi^{\pm}$), kaons ($K^{\pm}$) and (anti-)protons ($p^{\pm}$). Each of these distributions has a different binning within a range from 0.1 GeV up to 20 GeV. The yields show that most of the charged particles produced in pp collisions are pions. Especially for small momenta, the pion yield is about one order of magnitude higher than the one for kaons and protons.
Similar to before, reference data from the measurements of identified pions, kaons or protons ([ALI16]) are divided by the respective simulated p_{T} spectra. The resulting ratios are presented in fig. 20.
Since pions make up a large fraction of the total amount of final-state charged particles, their ratio of data/MC is rather similar to fig. 18. Indeed, the highest deviation between simulation and data is present at very small p_{T} of about 0.1 GeV, which is different for the distribution with all charged particles, but in the latter case, the measurement only starts at $p_{\mathrm{T}} = 0.15\,\mathrm{GeV}$. Nevertheless, in a range of $0.2\,\mathrm{GeV} < p_{\mathrm{T}} < 1\,\mathrm{GeV}$, the pion ratio features the same decrease down to 80 % as seen before. For higher p_{T}, however, it remains below unity.
In contrast to that, kaons and protons, which constitute a much smaller percentage of final-state charged particles, have a higher particle production for small p_{T} in the MC-generated spectrum than in the measured data. Going to higher momenta, both distributions first increase in the same way up to a ratio between 110 % and 120 %. Yet, while the kaon ratio keeps fairly constant above unity also for high p_{T}, the proton ratio decreases drastically down to a value of about 40 %.
Overall, the description of individual final-state hadrons in PYTHIA is quite inaccurate. There are only very small intervals where data and MC spectrum match within the given uncertainties. However, since several spectra are overestimated while others are underestimated, these deviations are smaller in the analysis of all final-state charged particles, at least for higher p_{T}. Instead, for lower momenta of about $0.3\,\mathrm{GeV} < p_{\mathrm{T}} < 0.8\,\mathrm{GeV}$ (varying a bit depending on which kind of particles are analysed), it seems to be characteristic for PYTHIA to overestimate the respective particle production.

5.2.2. Charged-Particle Multiplicity

Similar to p_T spectra, one can analyse the multiplicity of final-state charged particles in an event. In this section, multiplicities simulated by PYTHIA will be compared to data from ALICE.

Both simulated and measured distributions are illustrated in fig. 21 (a). There, the probability to find a certain number of charged particles N_{ch} is plotted for PYTHIA simulations with and without $\tau_{0,max} = 10$ mm applied and for measured data. In all of these spectra, the MB_{or} trigger was applied. The data are taken from pp collisions at a centre-of-mass energy of 7 TeV and filtered for a pseudorapidity interval of $|\eta| < 2$.

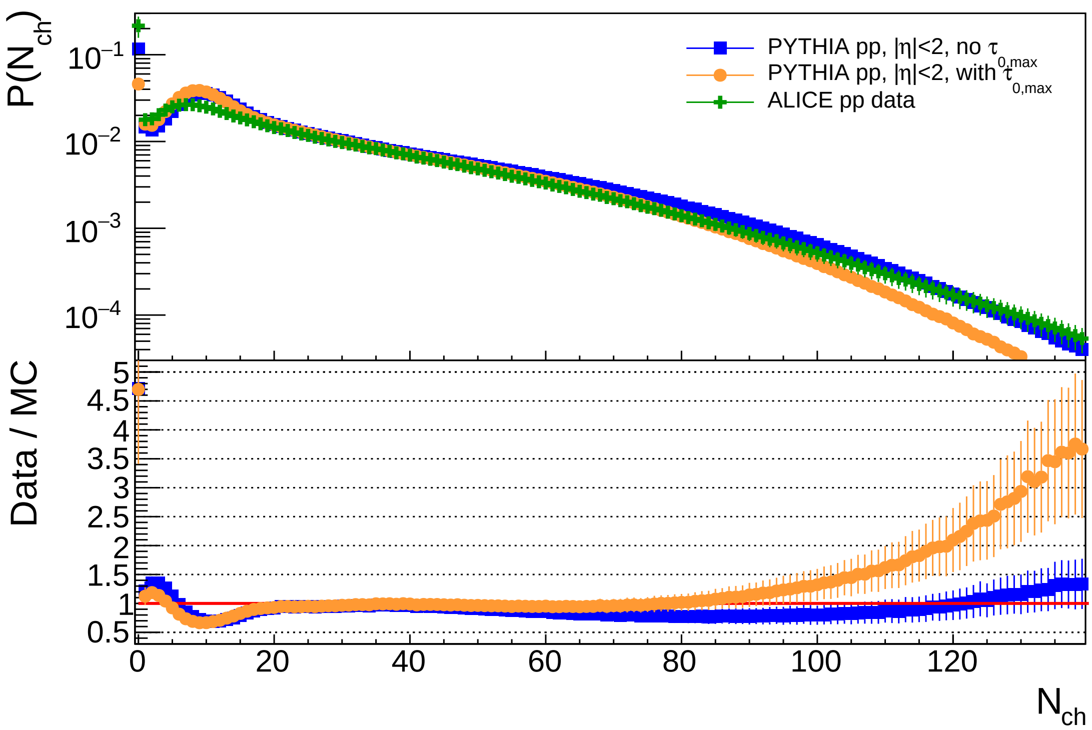

Figure 21: The top panel (a) contains charged-particle multiplicities of a simulated pp collision at $\sqrt{s} = 7$ TeV including only final-state charged particles with $|\eta| < 2$ with and without $\tau_{0,max}$ in comparison with measured data from [Col17]. The data/MC ratios are presented in the bottom panel (b).

Above 10 charged particles per event, all three curves are decreasing exponentially with higher N_{ch}. Below, the probabilities are first increasing up to a local maximum between 2 % and 4 %. This feature is more pronounced in the simulation than in the data. Also, the combined statistical and systematical uncertainties of the measured multiplicity grow for large N_{ch}, while the errors are in the order of 10^{-5} for the simulations. Finally, each

distribution shows an outlier at $N_{\mathrm{ch}} = 0$ with a probability between 5 % and 20 %. Thus, there is a significant amount of events that do not produce any charged particles in the chosen central pseudorapidity region. These might be diffractive events which show a gap in particle production at mid-rapidity.
Again, the ratio of measured over MC-generated $P(N_{\mathrm{ch}})$ is portrayed in fig. 21 (b) for the two simulated distributions discussed above. In both cases, there is first an underestimation of the simulated multiplicity below $N_{\mathrm{ch}} = 7$ which is smaller if the mentioned filters are applied. In contrast to that, the deviation from unity increases drastically for 0 charged particles by implementing these filters. Yet, this deviation is not very significant because it is very difficult to experimentally determine the number of events without any charged particles in the pseudorapidity range of $|\eta| < 2$. Additionally, PYTHIA overestimates the charged-particle multiplicity for $7 < N_{\mathrm{ch}} < 20$ rather independently of the $\mathrm{MB_{or}}$ trigger and the τ_0-limit.
For higher amounts of charged particles, measured and MC data initially agree with each other within their uncertainties in both cases. However, while the ratio without cut drops slightly below unity between $N_{\mathrm{ch}} = 60$ and $N_{\mathrm{ch}} = 120$, the other one increases strongly from $N_{\mathrm{ch}} = 80$ on. For 140 charged particles in the event, the measured multiplicity is then almost four times higher than the simulated one if $\tau_{0,\mathrm{max}}$ is set in PYTHIA. This shows that including the lifetime limit mainly affects events with a very high number of charged particles because there are no decay products from particles with a lifetime $\tau_0 > 10\,\mathrm{mm}$.

5.2.3. Effects of String Shoving

Collective effects as introduced in section 2.5.3 are mostly present in heavy-ion collisions due to the creation of QGP, but have also been observed in collisions of protons. Regarding the transverse momenta of outgoing particles, collective effects lead to a blueshift from small p_{T} towards the intermediate-momentum range.
Since PYTHIA does not model the creation of QGP, it also does not include a description of this blueshift in the transverse direction. Therefore, the MC-generated yield is assumed to be larger than the measured one at small p_{T} and smaller for intermediate p_{T}. This can be seen in fig. 18, where PYTHIA overestimates the particle production below 1 GeV, resulting in a drop of the ratio. Nevertheless, there is no prominent underestimation for intermediate momenta. [Bie+22]

The string shoving model is one attempt to account for these effects in PYTHIA without assuming that QGP is actually formed. Figure 22 portrays the result of applying string shoving after hadronisation in the MC event generation. Panel (a) gives the p_T spectra of measured data and the ones resulting from different PYTHIA simulations with and without shoving while part (b) illustrates the respective ratios of the three simulated spectra over ALICE data to visualise the differences.

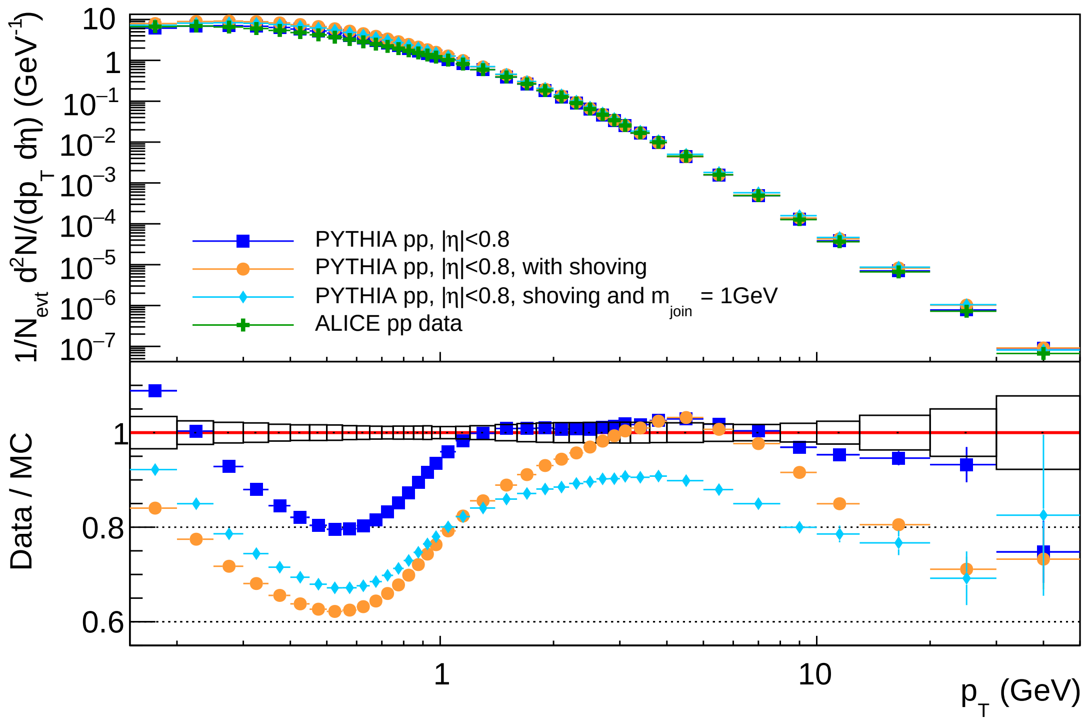

Figure 22: The top panel (a) shows MC-generated p_T spectra in units of GeV^{-1} from all charged particles in inelastic pp collisions at $\sqrt{s} = 5.02\,\mathrm{TeV}$ and $|\eta| < 0.8$ with and without shoving in comparison to measured data. The data/MC ratios are presented in the bottom panel (b).

For the moment, only the yields resulting from an event generation without shoving and with the default shoving model are discussed. The associated data/MC ratios are displayed in fig. 22 (b) in dark blue and orange.

The general shapes of the shown yields is quite similar. Only at small p_T are the yields including string shoving shifted upwards in comparison to the one without. Hence, the transversal push Δp_T applied by the shoving model seems to mainly increase the number of particles with small momenta. This results in a decrease in the orange ratio down to almost 60 %. For higher momenta, the effect of this transverse push reduces until both ratios are matching around $3\,\text{GeV} < p_\text{T} < 6\,\text{GeV}$. This is due to the default cutoff in the shoving model at $p_\text{T} = 2\,\text{GeV}$. However, for even higher p_T, the simulated yield including shoving is again shifted upwards, leading to another reduction of the orange ratio.

It turns out that the default string shoving model does not improve the reconstruction of p_T spectra in pp collisions. It only increases the MC-generated particle production in the analysed pseudorapidity interval of $|\eta| < 0.8$ and over the whole p_T range. Especially at small p_T, where the simulated yield is already higher than the measured one, this increase leads to a further drop in the ratio and thus to higher deviations from unity. This contradicts the expectations of a model which is supposed to account for collective-like effects in pp collisions.

The reason for the increase in multiplicity in the string shoving model is that excitation gluons are created in the interactions of nearby strings on the hadron level of the event generation. To account for this, nearby colour-connected partons can be joined into one state by setting the *FragmentationSystems:mJoin* parameter. This parameter gives the maximum mass m_join which a parton pair is allowed to have in order to be combined. Gluons are only counted with half of their momentum by checking for this limit. By default, this mass is given as $m_\text{join} = 0.3\,\text{GeV}$.

In another test of the string shoving model, excitation gluons are taken into account by setting the maximum mass for a pair of colour-connected partons to be combined into one particle state to $m_\text{join} = 1\,\text{GeV}$. The resulting PYTHIA yield is given in fig. 22 (a) as the light blue curve. In comparison to the default shoving model in orange, the light blue ratio is shifted upwards at small p_T due to the joining of nearby excitation gluons. At intermediate p_T, however, the ratio decreases since particles with such momenta are unaffected by the joining process while the total charged-particle multiplicity decreases. In contrast to that, both ratios agree with each other at high p_T within their uncertainties.

The same analysis is now applied to p_T spectra of identified pions (see fig. 23), kaons (fig. 24) and protons (fig. 25). Again, these plots show data/MC ratios resulting from PYTHIA simulations without shoving in dark blue, for the default shoving model in orange and for string shoving with $m_\text{join} = 1\,\text{GeV}$ included in light blue.

In all three cases, the biggest difference between the ratios with and the one without shoving is visible for small p_T. Similar to fig. 22 (b), the down-shift is smaller for the ratio including $m_\text{join} = 1\,\text{GeV}$ than for the one without. Above $p_\text{T} = 1\,\text{GeV}$, this turns around and the light blue ratio becomes smaller than the orange one.

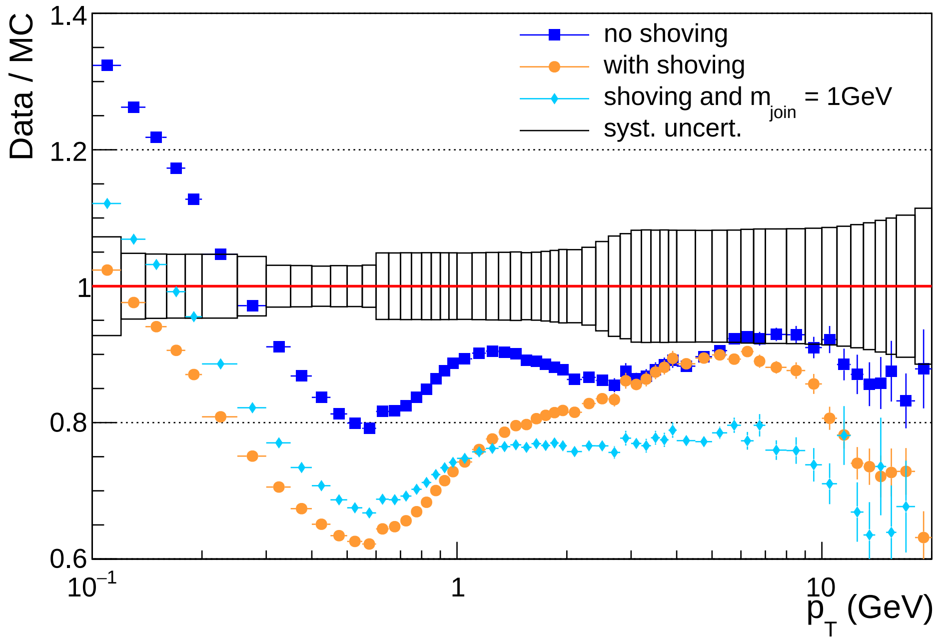

Figure 23: Ratio of p_{T} spectra from charged pions in inelastic pp collisions at $\sqrt{s}$ = 5.02 TeV with $|y| < 0.8$ once with and once without shoving switched on.

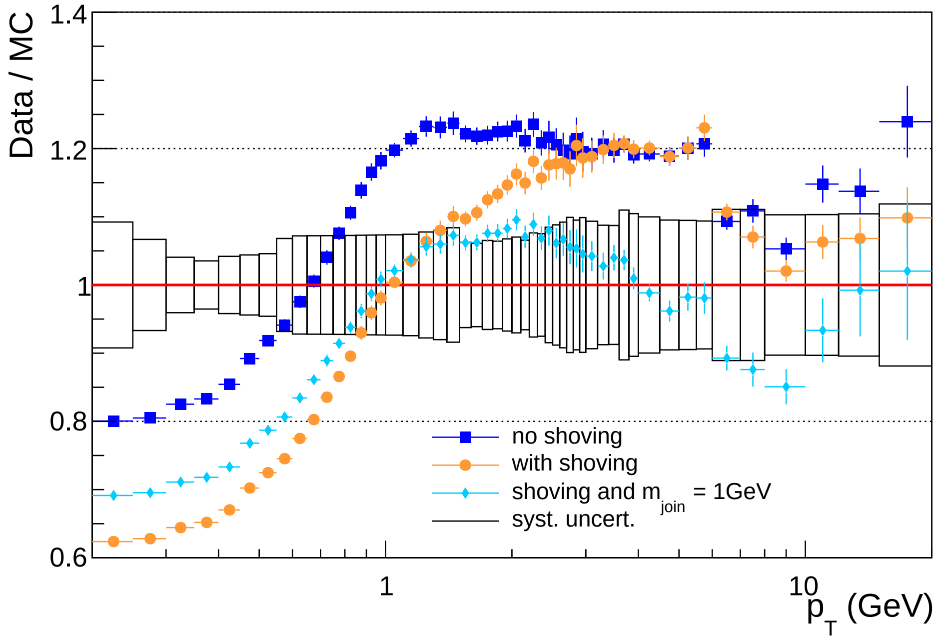

Figure 24: Ratio of p_{T} spectra from charged kaons in inelastic pp collisions at $\sqrt{s}$ = 5.02 TeV with $|y| < 0.8$ once with and once without shoving switched on.

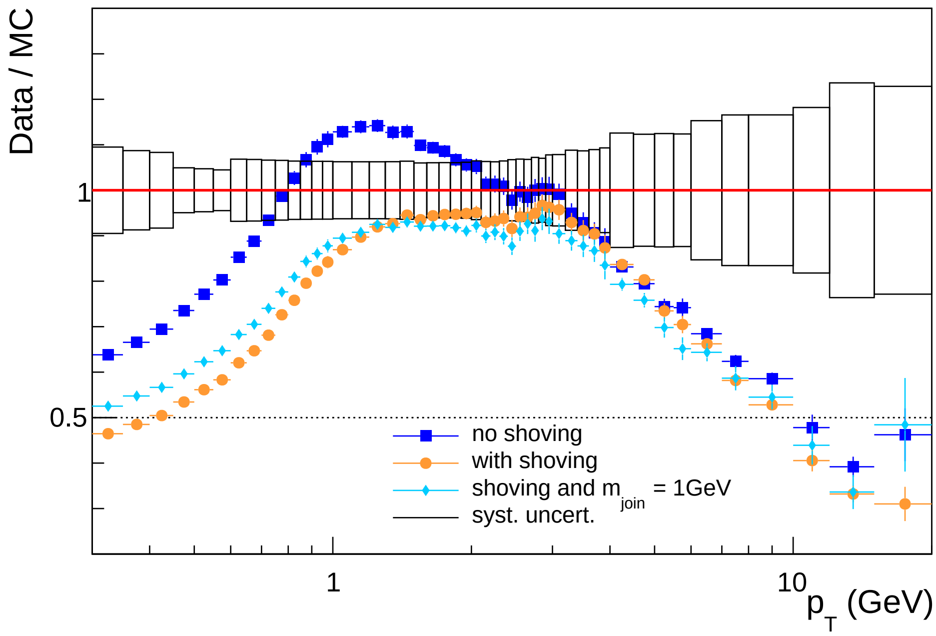

Figure 25: Ratio of p_{T} spectra from charged protons in inelastic pp collisions at $\sqrt{s}$ = 5.02 TeV with $|y| < 0.8$ once with and once without shoving switched on.

For pions and kaons, the behaviour of the ratios at intermediate to high p_{T} is similar to the analysis of all charged particles. While the orange and dark blue curves agree with each other for $3\,\mathrm{GeV} < p_{\mathrm{T}} < 6\,\mathrm{GeV}$, the former one falls below the latter one again at even higher momenta. At the same time, the shoving ratio including $m_{\mathrm{join}} = 1\,\mathrm{GeV}$ has a similar course to the ratio without shoving but shifted down. That is different in the case of identified protons, where all three ratios are rather similar for $p_{\mathrm{T}} > 3\,\mathrm{GeV}$. The offset between them is much smaller than for the pion and kaon ratios.
Moreover, a special characteristic in the pion ratios in fig. 23 is a jump at $p_{\mathrm{T}} = 0.6\,\mathrm{GeV}$ by about three percentage points. At the same point, the systematical uncertainty increases strongly. This is due to a change of the detector module for higher momenta in the measurement in ALICE.
Overall, string shoving leads to higher simulated yields especially at small p_{T}. This increase can be reduced by joining excitation gluons, but the deviation from ALICE data is still bigger than in events without shoving. Since only one value of m_{join} has been simulated, one could investigate the effects of different m_{join} on the MC-generated yields. However, the most probable reason for the differences to measured data is the fact that the default Monash 2013 tune is used in this thesis for generating events with the string shoving model since PYTHIA does not provide a sensible tune for this model.

To analyse the mentioned increase in particle production at small p_T further, the impact of string shoving on the charged particle multiplicity is determined in the following. In order to do so, the model is applied to the reconstruction of the charged-particle multiplicity in PYTHIA. The resulting yields with and without shoving are displayed in fig. 26 (a) together with ALICE data. The respective data/MC ratios are given in fig. 26 (b).

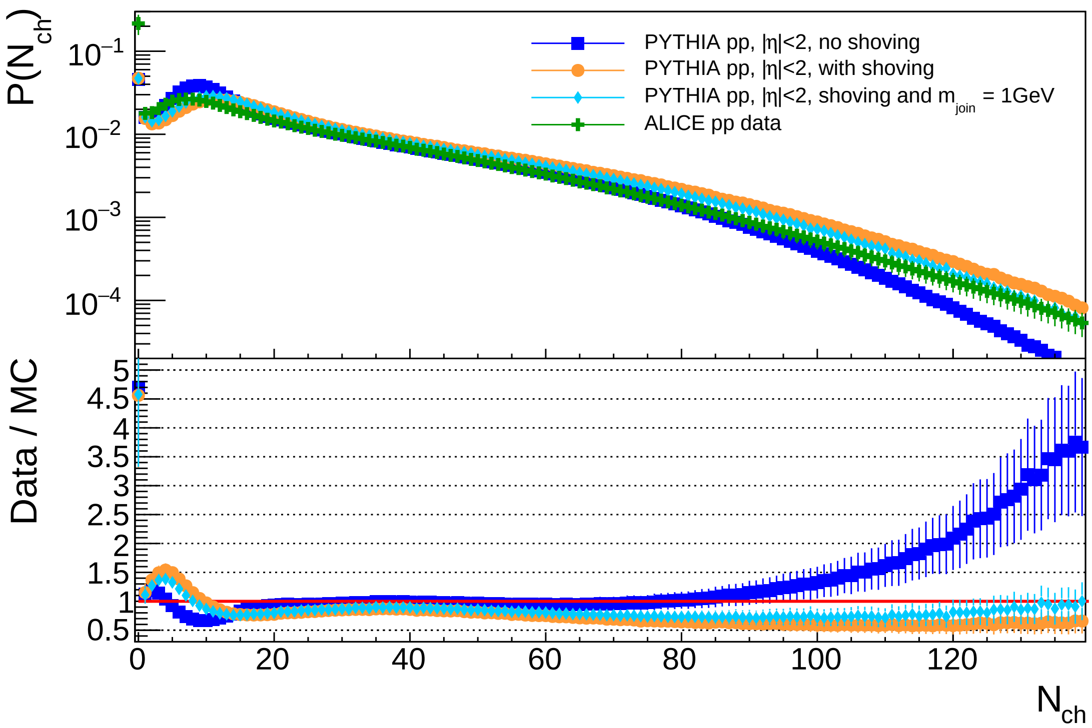

Figure 26: The top panel (a) shows simulated charged-particle multiplicities at $\sqrt{s} = 7\,\mathrm{TeV}$ including only final-state charged particles with $|\eta| < 2$ with and without shoving in comparison to measured data. The data/MC ratios are presented in the bottom panel (b).

Regarding the multiplicities, it turns out that string shoving shifts the distribution to higher N_{ch}. While the probability to find events with $N_{\mathrm{ch}} \lesssim 15$ decreases, it increases for events with a large number of charged particles. This is the most striking for events with $N_{\mathrm{ch}} > 80$, where the multiplicity from a default event generation falls below the measured distribution (leading to a strong increase in the respective ratio). In contrast to that, the simulations including string shoving exhibit a multiplicity that is higher than in the data. Hence, the resulting ratio stays below unity instead of a strong increase. For the default shoving model, the difference between measured and MC-generated multiplicity is too

big to be accounted for by the combined uncertainties. By including $m_{\text{join}} = 1\,\text{GeV}$, however, the ratio reaches unity within the uncertainties for $N_{\text{ch}} > 120$. Instead, the ratio for small N_{ch} is a bit smaller than for the default shoving model which means that there is a higher probability for events with fewer charged particles.
This behaviour is consistent with what has been observed in the p_{T}-spectra analysed before. The increase in multiplicity is mostly based on excitation gluons that are created by the string shoving model. By joining nearby gluons with a combined mass $m < m_{\text{join}} = 1\,\text{GeV}$, the increase in multiplicity can be reduced.

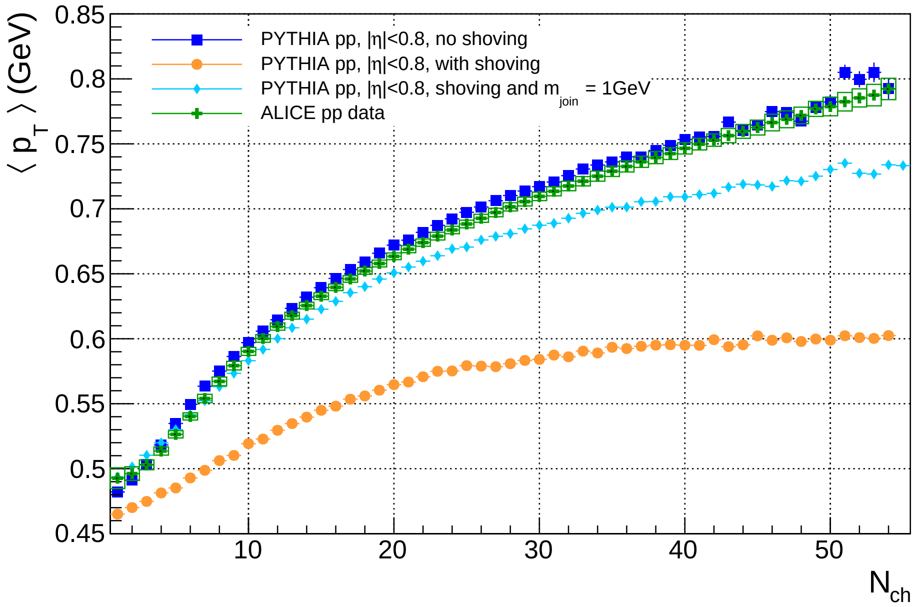

Figure 27: Mean p_{T} in dependence on N_{ch} with $|\eta| < 0.8$ and $0.15\,\text{GeV} < p_{\text{T}} < 10\,\text{GeV}$ in comparison with data from [Col22a].

In a last test of the string shoving model in pp collisions, the average transverse momentum $\langle p_{\text{T}} \rangle$ in dependence of the N_{ch} per event is analysed.
According to fig. 27, $\langle p_{\text{T}} \rangle$ is for all events in the considered N_{ch} interval below $1\,\text{GeV}$. The reason for that is that the number of particles decreases exponentially with increasing momentum. Also, $\langle p_{\text{T}} \rangle$ grows first strongly and then weaker with N_{ch}. The PYTHIA simulation without shoving reproduces the measured curve very well. Both increase from $\langle p_{\text{T}} \rangle \approx 0.5\,\text{GeV}$ for only one charged particle per event with $|\eta| < 0.8$ up to $\langle p_{\text{T}} \rangle \approx 0.8\,\text{GeV}$ for $N_{\text{ch}} = 55$.
In contrast to that, the simulated spectrum with the default shoving model only reaches $\langle p_{\text{T}} \rangle \approx 0.6\,\text{GeV}$ and saturates above $N_{\text{ch}} = 40$. Thus, string shoving with the applied

push Δp_{T} does not increase but actually decrease the average momentum. The reason for that arises from the previous analysis of p_{T} spectra, which shows that mainly the number of particles with small p_{T} is increased. Furthermore, the model produces gluons with small momenta in interactions between the hadronising strings. By merging nearby low-p_{T} particles in the event generation with shoving, $\langle p_{\mathrm{T}} \rangle$ increases. For a small value of N_{ch} per event, the shoving model with $m_{\mathrm{join}} = 1\,\mathrm{GeV}$ in light blue even agrees with the ALICE data in green. With increasing N_{ch}, however, the light blue curve increases less strongly and only reaches $\langle p_{\mathrm{T}} \rangle \approx 0.73\,\mathrm{GeV}$ at $N_{\mathrm{ch}} = 55$. A possible explanation for the remaining difference in $\langle p_{\mathrm{T}} \rangle$ is that the default Monash 2013 tune does not include string shoving effects.

In total, applying the default string shoving model to the event generation in PYTHIA does not lead to smaller deviations from ALICE data. As already said, it actually has a contrary effect on the simulated yield than expected and only increases the differences in the ratios data/MC. The increased particle production, especially at small p_{T}, can mostly be explained by excitation gluons, which are created in string interactions. These can be accounted for by setting the m_{join} parameter in the event generation. Implementing this parameter in the event generation improves the agreement with measured data in the analysis of the charged-particle multiplicity and the mean transverse momentum. It also reduces the deviation from unity in the data/MC ratios of p_{T}-spectra at small momenta. Still, the simulated yields of all charged particles with shoving included show bigger deviations from unity than the simulation without shoving.

Hence, the string shoving model alone with the settings applied in this thesis does not account for collective-like effects in pp collisions. A possible reason might be that the default Monash 2013 tune was used in the event generation since there is no PYTHIA tune for string shoving available yet.

5.3. Results from p–Pb Collisions

In contrast to collisions of protons, every p–Pb collision has a different centrality depending on the impact parameter between proton and lead nucleus. Hence, the outcome of simulations in PYTHIA can be compared with measured data in different centrality classes. This is done in section 5.3.1 for the p_T spectra of all final-state charged particles and for the individual hadrons $\pi^{\pm}$, $K^{\pm}$, and $p^{\pm}$. Additionally, a centrality-independent comparison among measured and simulated NSD events is presented in section 5.3.2. For this, p_T spectra independent of the collision centrality are created. In a last step, similar to the previous chapter, the result of applying the string shoving model to the generation of p–Pb events will be investigated in section 5.3.3.

5.3.1. Comparison with Centrality Dependent Data

In p–Pb collisions, the centrality cannot be determined geometrically as outlined in section 2.5.1. Instead, different centrality classes are defined over the charged-particle multiplicity in an event.

By following the Glauber model as presented in section 2.5.2, high impact parameters (corresponding to peripheral collisions) lead to a relatively small number of proton-nucleon subcollisions. Hence, only a few number of final-state charged particles are created, whereas events with smaller impact parameters (corresponding to central collisions) contain much more charged particles. The centrality of an event can thus be approximately identified by counting all final charged particles.

The boundaries of different multiplicity classes are determined by integrating over the multiplicity of charged particles registered in the pseudorapidity range $2.8 < \eta < 5.1$ corresponding to the V0A detector in the Pb-going direction. As shown in fig. 28, this integral is divided into seven such intervals. Starting from the event with the most charged particles, the first interval represents all events belonging to the highest 5 % of the integral, corresponding to the 0-5 % multiplicity class. For the case of a minimum-bias MC-generated spectrum, which is plotted here as blue squares, the lower limit of this most central class is $N_{\text{ch}} = 109$. Analogously, the other classes represent the 5-10 % (with the lower limit $N_{\text{ch}} = 90$), 10-20 % ($N_{\text{ch}} = 69$), 20-40 % ($N_{\text{ch}} = 47$), 40-60 % ($N_{\text{ch}} = 31$) and 60-80 % ($N_{\text{ch}} = 16$) most central events. The most peripheral multiplicity class 80-100 % requires at least one charged particle in the V0A pseudorapidity range.

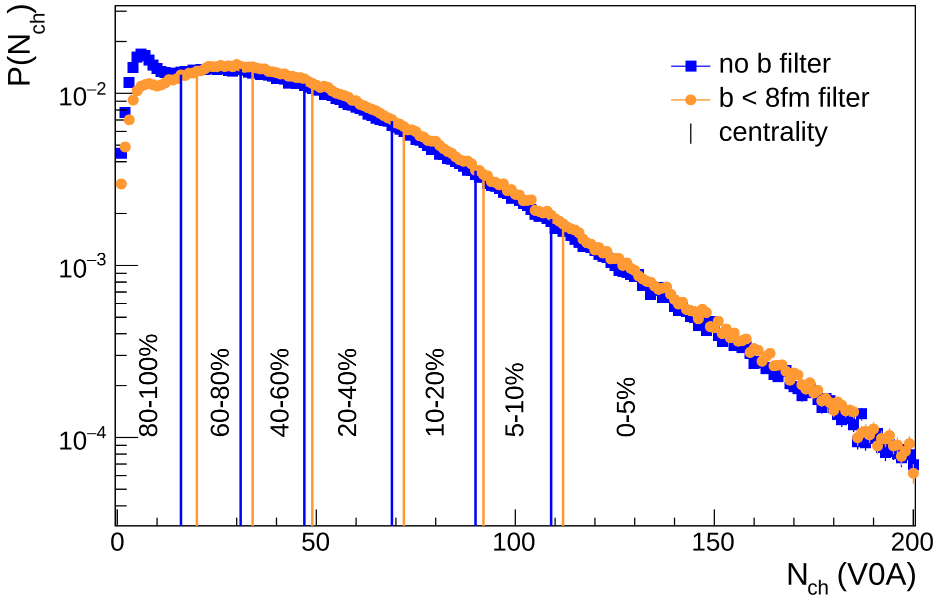

Figure 28: Charged-particle multiplicity of a simulated p–Pb collision at $\sqrt{s_{\mathrm{NN}}} = 5.02\,\mathrm{TeV}$ including only final-state charged particles with $2.8 < \eta_{\mathrm{lab}} < 5.1$ with and without an impact parameter filter switched on. The vertical numbers represent the multiplicity class corresponding to the indicated N_{ch}.

Overall, the charged-particle multiplicity is flatter than for pp collisions and is going to much higher N_{ch} since there are more subcollisions in the lead nucleus. The highest probability is given as a peak centred around $N_{\mathrm{ch}} = 7$ with almost $2\,\%$. The probability to find even less charged particles in an event falls drastically, which might be due to the requirement of the $\mathrm{MB}_{\mathrm{and}}$ trigger in the event selection. For higher N_{ch}, the probability is first decreasing and then features a flat peak around $N_{\mathrm{ch}} \approx 30$. From there, the probability for even more charged particles in an event decreases exponentially analogously to pp collisions.

Additional to the minimum-bias analysis displayed in blue, the orange curve describes an analysis where each event with an impact parameter $b \geqslant 8\,\mathrm{fm}$ has been sorted out in the event generation. This cutoff originates from the assumptions for the nuclear radii of lead-nuclei with $R_{\mathrm{Pb}} \approx 7\,\mathrm{fm}$ and protons with $R_{\mathrm{p}} \leqslant 1\,\mathrm{fm}$. Thus, this filter leads to the exclusion of events with no overlap between the nuclei. According to fig. 28, the mentioned cutoff reduces the peak in the multiplicity for small N_{ch} and shifts the boundaries of the multiplicity classes to higher N_{ch}. The reason is that the discarded events with no overlap only produce very few charged particles in electromagnetic interactions. This does not have a significant impact on the probability for events with a high number of

charged particles.
Given these intervals, each event in PYTHIA is categorised in a multiplicity class according to the N_{ch} in the event. For each class, particle yields are extracted and normalised by the sum of weights of all events in this class.
As an example, the simulated and measured pion yields are given for the mentioned multiplicity classes in fig. 29. Additionally, the simulated spectrum has been scaled by a factor of 10^2 for better visibility. The measured data also include systematical uncertainties printed as boxes but in most cases, these are too small to be visible.
It turns out that the yields from different multiplicity classes are in both cases ordered by their centrality. This makes sense because the most central multiplicity class is defined as the one with the most charged particles per event. Moreover, all spectra are decreasing exponentially with higher momenta. However, the simulated yields drop faster than the ones in the measurement for high p_{T}. Also, the MC-generated spectrum in the most peripheral multiplicity class $80\,\% < c \leqslant 100\,\%$ has an offset to the next more central class while the spectra of other classes are lying closer together.

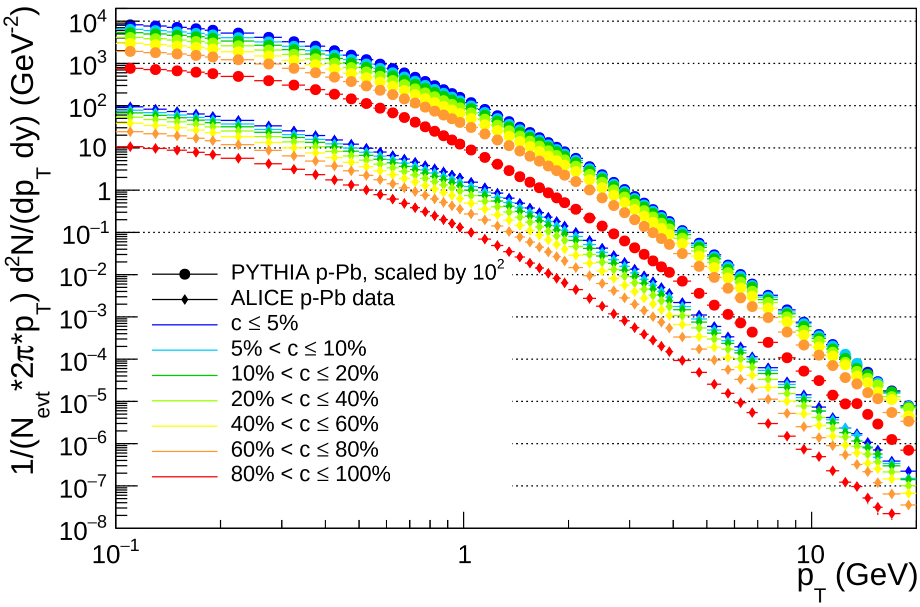

Figure 29: p_{T} spectra of simulated p–Pb collisions at $\sqrt{s_{\mathrm{NN}}} = 5.02\,\mathrm{TeV}$ including only final-state pions with $-0.5 < y_{\mathrm{CM}} < 0.0$ scaled with a factor 10^2 in comparison with measured data from [ALI16].

This offset in the most peripheral simulated yield results in a shift of the corresponding ratio data/MC in comparison to more central classes, which is illustrated in fig. 30.

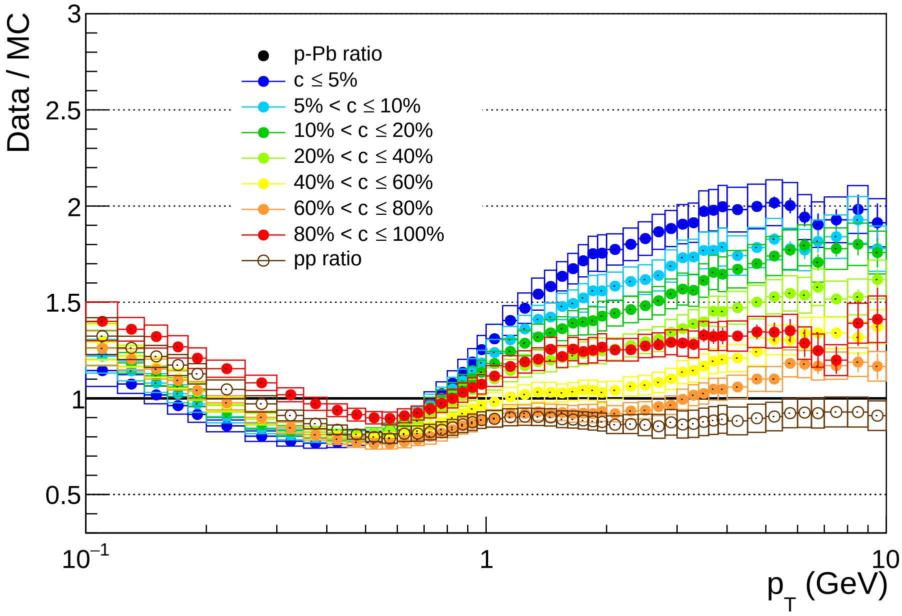

Figure 30: Ratios of the previous shown p_{T} spectra at $\sqrt{s_{\mathrm{NN}}} = 5.02\,\mathrm{TeV}$ including only final-state pions with $-0.5 < y_{\mathrm{CM}} < 0.0$.

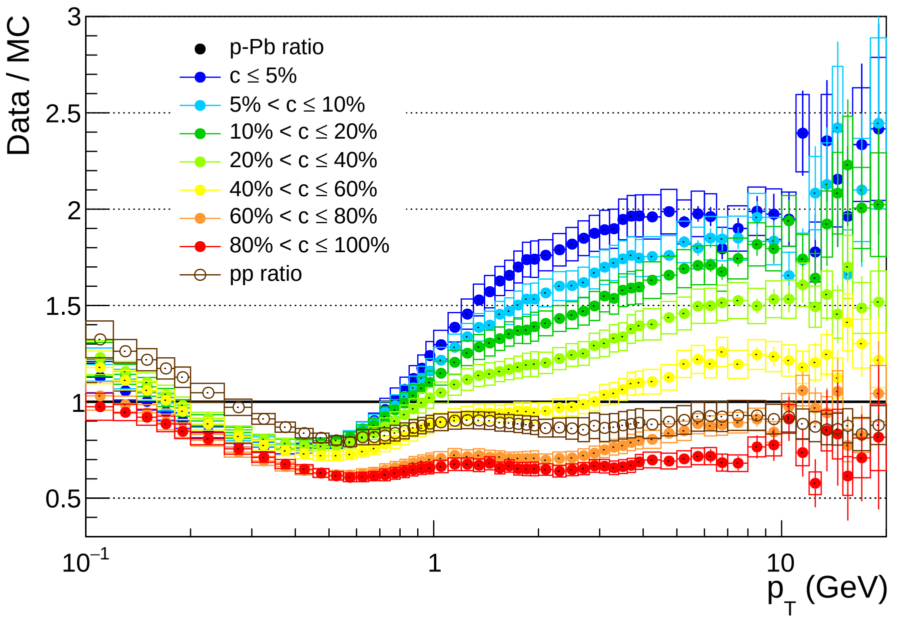

Figure 31: Ratios of p_{T} spectra at $\sqrt{s_{\mathrm{NN}}} = 5.02\,\mathrm{TeV}$ including only final-state pions with $-0.5 < y_{\mathrm{CM}} < 0.0$ and with an impact parameter $b < 8\,\mathrm{fm}$. The corresponding data/MC ratio from pp collisions is plotted for comparison.

Again, most ratios are ordered according to their collision centrality. For $p_{\mathrm{T}} < 0.5\,\mathrm{GeV}$, a valley similar to the pion ratio in pp collisions appears. The most central class features the lowest ratio and thus the biggest deviation with a minimum of about 80 %. This changes at higher momenta, where the ratio gets higher the more central the collision is. For $c \leqslant 5\,\%$, the ratio increases up to 200 %, meaning that the measured yield is twice as big as the MC-generated one. At the same time, the second most peripheral class contains ratios only up to 120 % while the other classes are somewhere in-between. This is different from the previously analysed ratio in pp collisions, where the ratio stays below unity for high p_{T}.
As already mentioned, the most peripheral multiplicity class does not fit in this ordering. Instead, it is shifted upwards and contains ratios up to 140 %. This is because the PYTHIA event generation of the displayed yields includes events where the impact parameter is larger than the radius of the lead nucleus. Therefore, also events with no overlap between proton and lead nucleus are part of the most peripheral class. In these events, only a few charged particles are created in electromagnetic interactions. The impact of discarding all events with $b \geqslant 8\,\mathrm{fm}$ in the event generation is analysed in the following simulation.
Figure 31 depicts ratios which include the mentioned impact parameter filter. Moreover, the pion ratio from pp collisions is portrayed for comparison with the most peripheral p-Pb collisions where the number of binary N-N collisions is very small and thus similar to a collision of two protons. It appears that rather central multiplicity classes ($c \leqslant 60\,\%$) are not changed by the implemented centrality filter. Only the systematical and statistical uncertainties grow strongly at high p_{T} since the x-axis has been extended to 20 GeV. Instead, the simulated yield per event in the two most peripheral classes increases as expected, leading to a decrease in the respective ratios. Additionally, the curves are flatter than before and the minimum for small p_{T} is less distinct since the ratios stay below unity. In particular, the ratio in the most peripheral class $80\,\% < c \leqslant 100\,\%$ is now similar to the pp ratio but shifted downwards. This shows that the processes in very peripheral p–Pb collisions are comparable to pp events.
Another analysis of the filter $b < 8\,\mathrm{fm}$ in the PYTHIA event generation has been conducted for kaon and proton yields in different multiplicity classes. The resulting ratios of data / MC are shown in fig. 32 for kaons and in fig. 33 for protons. In both cases, the general behaviour is conceptually similar to the analysis of pions.

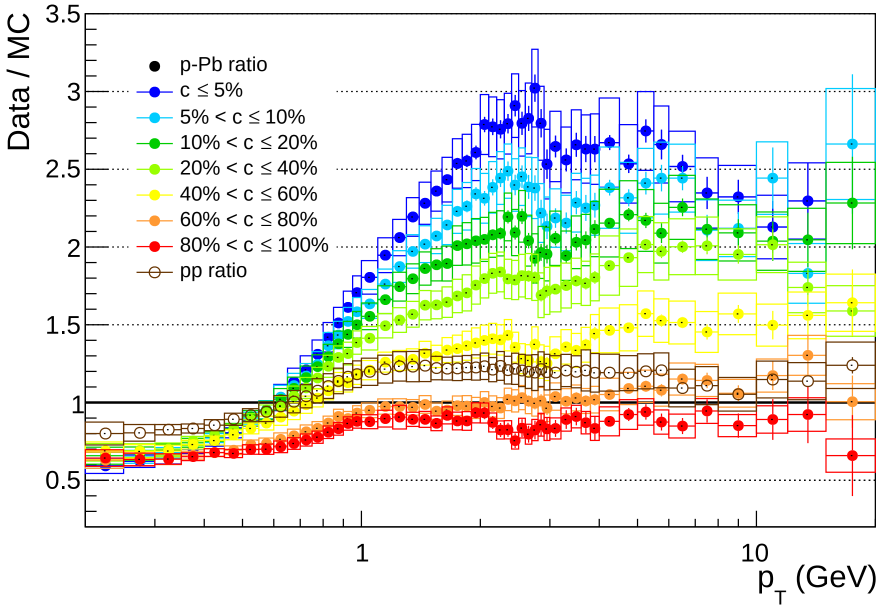

Figure 32: Ratios of p_{T} spectra at $\sqrt{s_{\mathrm{NN}}} = 5.02\,\mathrm{TeV}$ including only final-state kaons with $-0.5 < y_{\mathrm{CM}} < 0.0$ and with an impact parameter $b < 8\,\mathrm{fm}$. The corresponding ratio from pp collisions is plotted for comparison.

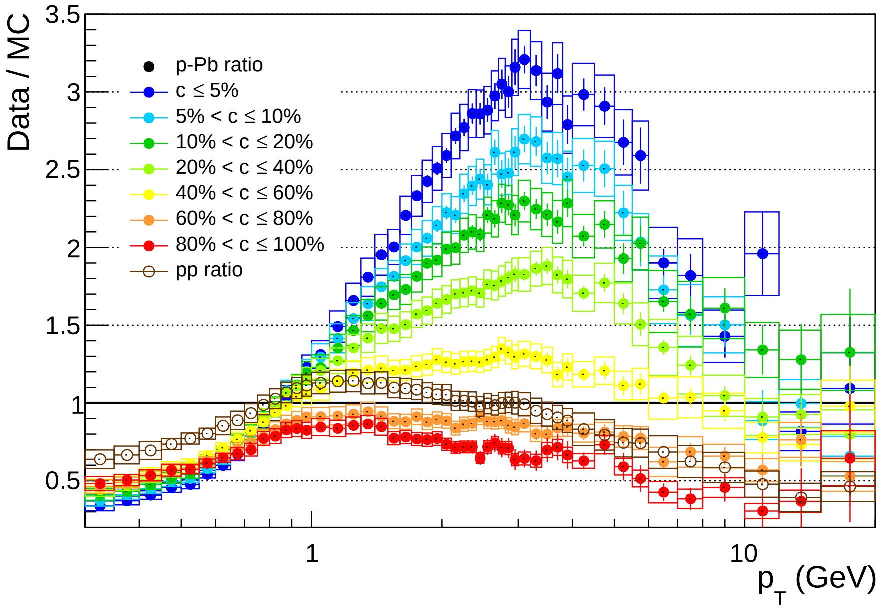

Figure 33: Ratios of p_{T} spectra at $\sqrt{s_{\mathrm{NN}}} = 5.02\,\mathrm{TeV}$ including only final-state protons with $-0.5 < y_{\mathrm{CM}} < 0.0$ and with an impact parameter $b < 8\,\mathrm{fm}$. The corresponding ratio from pp collisions is plotted for comparison.

In the case of kaons, PYTHIA initially overestimates the particle production at small p_{T} independently of the centrality of the collision. Analogously to the comparative ratio from pp collisions, this changes for larger momenta. Similar to fig. 31, the highest deviations from unity are found in the most central multiplicity class with a particle production in the measured data up to three times as high as in the simulation. This deviation decreases with increasing centrality. Again, the ratio in the most peripheral class is running in parallel but shifted downwards in comparison to the distribution from pp collisions.
The same applies to the ratios of proton yields with the main difference that the proton ratios decrease again towards unity after they have reached a peak. Hence, PYTHIA does not underestimate the production of high-p_{T} protons like it does for kaons in rather central collisions. However, the position of the peak depends on the collision centrality. In the four most central classes, the peak is centred around $p_{\mathrm{T}} = 3\,\mathrm{GeV}$. The shape of the peak also flattens with decreasing centrality. More peripheral classes do not feature a distinct peak but in the most peripheral class, the maximum of the curve is around $1\,\mathrm{GeV}$ as it is also the case in the comparative pp ratio.
Overall, the reconstruction of measured p_{T} spectra in PYTHIA is quite imprecise. The biggest deviations are found in the most central collisions where the measured particle production for certain momenta is two to three times bigger than the MC-generated yield. In contrast to that, the deviations from data in more peripheral classes are rather low. A possible reason for that might be that QGP-like effects have a stronger impact on more central collisions.

5.3.2. Comparison with Data from NSD Events

In this section, measured p_{T} spectra from p–Pb collisions will be compared with simulation results in a MB analysis without a division into different multiplicity classes. Like in section 5.2.1, this comparison is done once for all charged particles and once for individual pions, kaons, and protons.
Figure 34 displays the measured and simulated yields of final charged particles for transverse momenta between $p_{\mathrm{T}} = 0.15\,\mathrm{GeV}$ and $p_{\mathrm{T}} = 50\,\mathrm{GeV}$. In comparison with the p_{T}-spectrum resulting from pp collisions, the shown p–Pb yields are up to one order of magnitude higher since there are much more nucleons in the lead nucleus interacting with the projectile proton than in a single target proton.

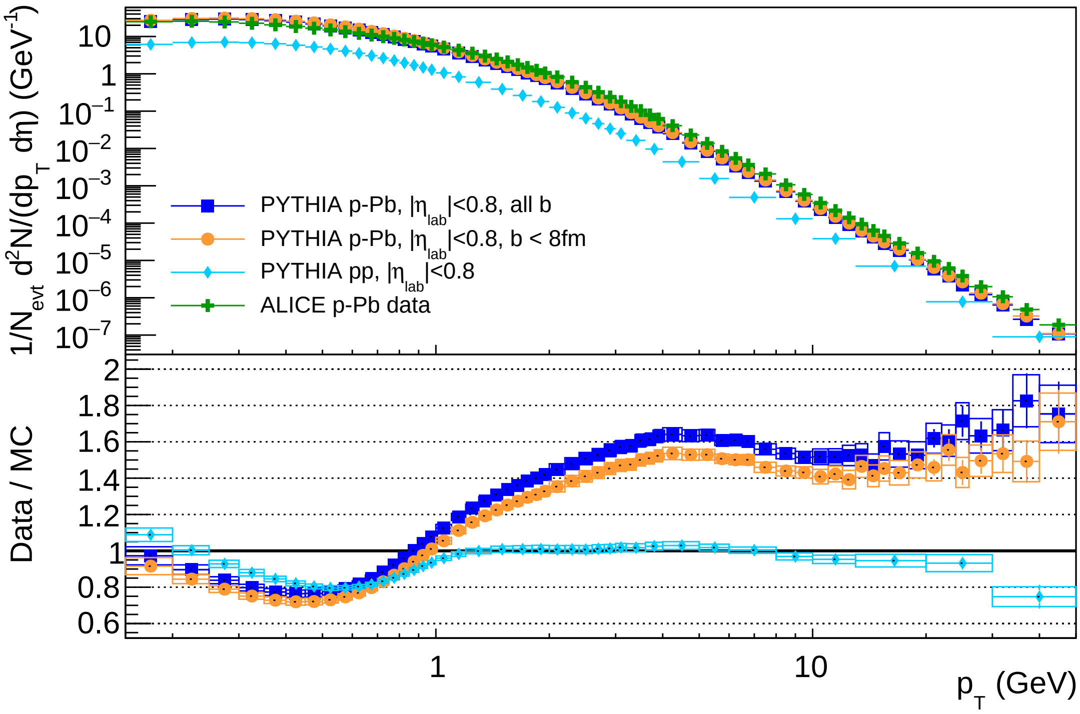

Figure 34: The top panel (a) shows p_T spectra of simulated NSD p–Pb collisions at $\sqrt{s_\mathrm{NN}} = 5.02\,\mathrm{TeV}$ in units of GeV^{-1} including only final-state charged particles with $|\eta_\mathrm{lab}| < 0.8$ in comparison with measured data from [ALI18]. The lower panel (b) portrays the ratios of measured data to the simulated spectra. A ratio from pp collisions is plotted for comparison.

Another phenomenon that one can see directly is that the simulated spectrum is overestimated by PYTHIA for small p_T and underestimated for large p_T. This is highlighted by the ratio plot in the lower part of the figure, where also the corresponding ratio from pp collisions including the τ_0 cut (see fig. 18) is shown for comparison. For momenta below 1 GeV, all three distributions have a similar form. The only difference from pp to p–Pb is that the deviation from unity grows slightly and its minimum shifts to $p_\mathrm{T} = 0.5\,\mathrm{GeV}$. Above 1 GeV, however, the difference gets much bigger. While the pp ratio stays mostly around or below unity, the p–Pb distributions are increasing strongly towards a peak at $p_\mathrm{T} \approx 4\,\mathrm{GeV}$ of about 160 %. Afterwards, the ratios first decrease and then rise again towards the highest deviation between simulation and data with up to 80 percentage points for very high $p_\mathrm{T} > 30\,\mathrm{GeV}$.

Furthermore, the difference between the minimum-bias case and the application of the filter $b < 8\,\mathrm{fm}$ for possible impact parameters in the event generation is indicated. As an average over all centralities, the ratio including this filter is only shifted downwards a

bit which does not imply a big improvement regarding the deviation between measured and simulated results. Still, to not generate events without any hard collisions, they are selected according to $b < 8\,\mathrm{fm}$ in all remaining PYTHIA simulations.
In a next step, measured p_T spectra of identified charged pions, kaons, and protons have been compared with simulated distributions. The resulting data/MC distributions are portrayed in fig. 35 together with the corresponding pp ratios as references.

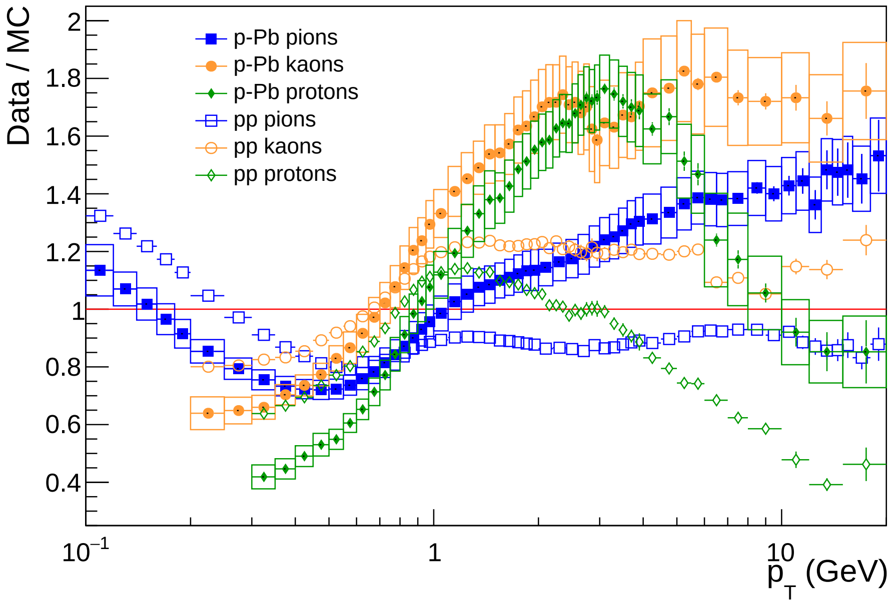

Figure 35: Ratios of p_T spectra from charged pions, kaons, and protons in NSD p–Pb collisions at $\sqrt{s_\mathrm{NN}} = 5.02\,\mathrm{TeV}$ with $-0.5 < y_\mathrm{CM} < 0.0$, including the filter $b < 8\,\mathrm{fm}$. The reference data are taken from [ALI16]. Ratios from pp collisions are plotted for comparison.

In all three cases, the p–Pb ratios are smaller than their pp counterparts for small p_T. Above a momentum of about $1\,\mathrm{GeV}$, this turns around and the p–Pb distributions increase much more. Like in the analysis of all charged particles, the ratios reach a deviation of up to 180 %. Nevertheless, the general behaviour of the different curves stays rather similar. While the kaon ratio remains around a value of 180 %, the proton ratio decreases again towards 90 %.
Hence, PYTHIA underestimates the particle production at intermediate to high momenta in p–Pb collisions much more than in pp events. Instead, for very small p_T, the overestimation gets slightly stronger. This might be explained by a stronger blueshift in the transverse movement due to collective-like effects. To account for that, the string shoving model is applied to the MC event generation in the next section.

5.3.3. Effects of String Shoving

Similar to pp collisions, the string shoving model is applied to the generation of p–Pb events and gives a transverse push Δp_T to the outgoing hadrons.
The effects of this model on the data/MC ratios of centrality dependent p_T spectra are analysed first. Hereby, the multiplicity classes are unchanged but the boundaries of the integrals are shifted to higher N_{ch}. The intervals are shown in table 1 for the default shoving model and for a simulation where excitation gluons are accounted for.

	no shoving	default shoving	shoving with $m_{join} = 1\,\mathrm{GeV}$
$c \leq 5\,\%$	$N_{ch} \geq 112$	$N_{ch} \geq 165$	$N_{ch} \geq 138$
$5\,\% < c \leq 10\,\%$	$112 > N_{ch} \geq 92$	$165 > N_{ch} \geq 131$	$138 > N_{ch} \geq 113$
$10\,\% < c \leq 20\,\%$	$92 > N_{ch} \geq 72$	$131 > N_{ch} \geq 97$	$113 > N_{ch} \geq 86$
$20\,\% < c \leq 40\,\%$	$72 > N_{ch} \geq 49$	$97 > N_{ch} \geq 63$	$86 > N_{ch} \geq 56$
$40\,\% < c \leq 60\,\%$	$49 > N_{ch} \geq 34$	$63 > N_{ch} \geq 41$	$56 > N_{ch} \geq 37$
$60\,\% < c \leq 80\,\%$	$34 > N_{ch} \geq 20$	$41 > N_{ch} \geq 24$	$37 > N_{ch} \geq 20$
$80\,\% < c \leq 100\,\%$	$20 > N_{ch} \geq 1$	$24 > N_{ch} \geq 1$	$20 > N_{ch} \geq 1$

Table 1: Boundaries of multiplicity classes for events with $b < 8\,\mathrm{fm}$.

The data/MC distributions resulting from an event generation with the default shoving model applied are illustrated in fig. 36. Again, the corresponding pp ratio of charged pions is given as a reference.
In comparison to fig. 31, the minimum for low p_T in the ratios with shoving is shifted down to about 50 - 60 % and the ratio is below unity for all centralities. Above 1 GeV, PYTHIA starts to underestimate the pion yields in the rather central multiplicity classes and the ratios increase with a higher slope than in the default case. Although shoving is by default cut off at 2 GeV, this increase continues until $p_T = 4\,\mathrm{GeV}$. Above that momentum, the deviations from unity in the most central and most peripheral ratios are even larger than in the analysis without string shoving. Therefore, string shoving rather decreases than increases central yields at intermediate p_T.
By including $m_{join} = 1\,\mathrm{GeV}$ in the event generation with shoving, however, the PYTHIA yields are more similar to the measured ones. The resulting ratios are displayed in fig. 37. At small p_T, the increase in the simulated yield is weaker than in the default shoving model. Furthermore, there is also an increase at intermediate p_T in rather central classes which leads to smaller deviations from unity. Still, the most central measured yield is almost twice as high as the MC-generated one for $p_T > 4\,\mathrm{GeV}$.
Similar results can be obtained from the analysis of kaon and proton yields which are shown in appendix A.

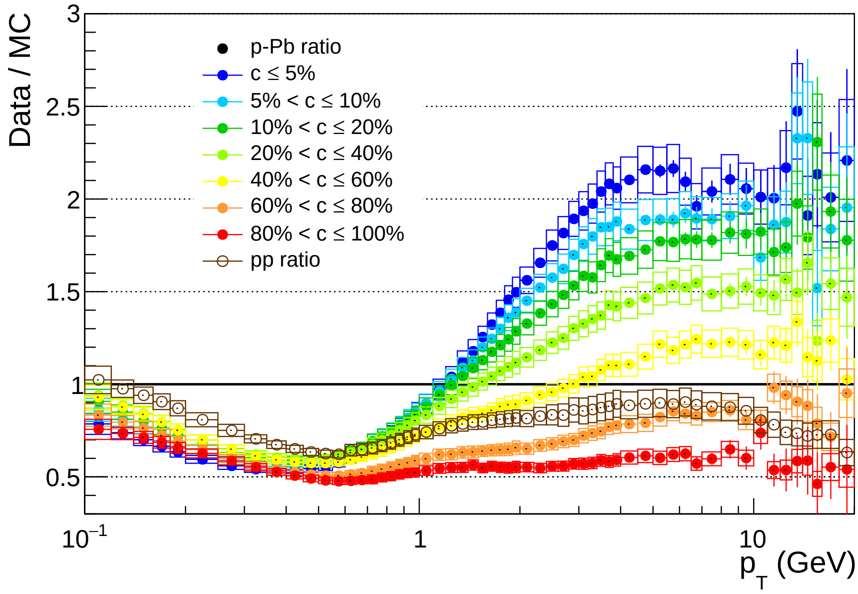

Figure 36: Data/MC ratios of p_{T} spectra at $\sqrt{s_{\mathrm{NN}}} = 5.02\,\mathrm{TeV}$ including only final-state pions with $-0.5 < y_{\mathrm{CM}} < 0.0$ and $b < 8\,\mathrm{fm}$. The default string shoving model has been applied to the PYTHIA event generation. A ratio from pp collisions including shoving is plotted for comparison.

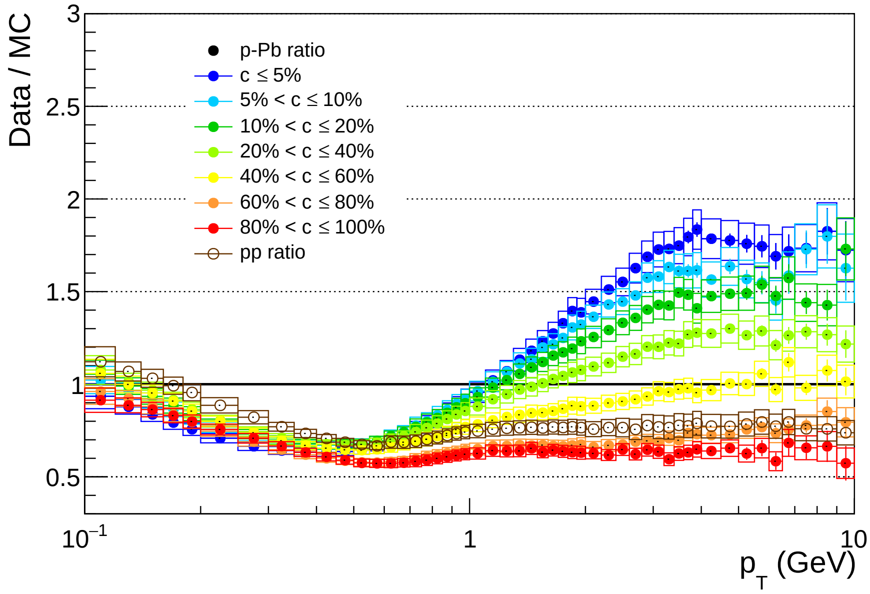

Figure 37: Data/MC ratios of p_{T} spectra at $\sqrt{s_{\mathrm{NN}}} = 5.02\,\mathrm{TeV}$ including only final-state pions with $-0.5 < y_{\mathrm{CM}} < 0.0$ and $b < 8\,\mathrm{fm}$. String shoving has been applied with $m_{\mathrm{join}} = 1\,\mathrm{GeV}$. The corresponding pp ratio is plotted for comparison.

As a next step, the effects of string shoving on the charged-particle yields in NSD p–Pb collision are presented in fig. 38. Additionally to the ratio for all charged particles, ratios of identified pions, kaons, and protons are depicted in different subplots.

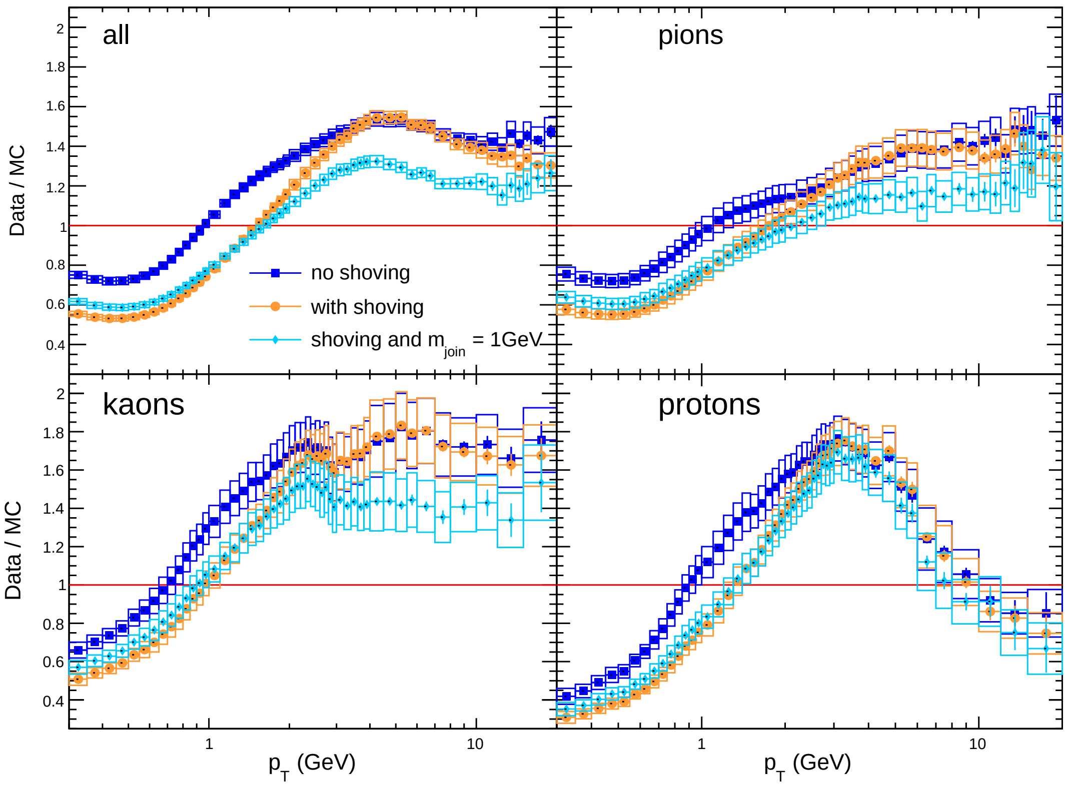

Figure 38: Data/MC ratios of p_T spectra from all charged particles with $|\eta_{lab}| < 0.8$ and from identified pions, kaons, and protons with $-0.5 < y_{CM} < 0.0$ in NSD p–Pb collisions at $\sqrt{s_{NN}} = 5.02\,\text{TeV}$ with and without shoving.

In all four cases, the default string shoving model increases the MC-generated yields for $p_T < 3\,\text{GeV}$, resulting in a decrease in the ratio. This decrease is more significant for all charged particles and for identified pions than for kaons and protons. At higher momenta, the ratio matches the results of an analysis without shoving with the exception of another small drop in the ratio at $p_T > 10\,\text{GeV}$ which is again more significant in the upper two subplots.

In contrast to that, the ratio including string shoving and $m_{join} = 1\,\text{GeV}$ leads to smaller deviations from unity at intermediate to high p_T. In this case, the data/MC ratio of all charged particles decreases at its peak from about about 160 % to approximately 130 %. Nevertheless, the deviations from unity at small p_T are larger than for events without shoving but still slightly smaller than with the default shoving model.

Overall, the default string shoving model does not lead to a better description of measured yields in PYTHIA. This changes by setting $m_{\mathrm{join}} = 1\,\mathrm{GeV}$ to join excitation gluons which are created in interactions of the strings. Especially at intermediate to high p_{T}, this leads to higher MC-generated yields and thus smaller deviations from data. However, the MC-generated yields are also increased for small p_{T} which leads to higher deviations from measurements in ALICE since the data/MC ratios are already below unity. These results differ from the analysis for pp collisions in section 5.2.3, where string shoving lead to no improvement in the description of p_{T} spectra.
Hence, the string shoving model alone does not account for the blueshift from small to intermediate momenta which is present in the measured data. Especially for small p_{T}, string shoving increases the MC-generated yield even further which is the opposite of what would have been expected from a model that is supposed to account for collective-like effects in PYTHIA. Again, this might be due to the fact that all simulations have been performed with the default Monash 2013 tune.

5.4. Results from Pb–Pb Collisions

Heavy ions, in particular lead nuclei, are collided at the LHC to probe QGP and its properties. This type of collision is of special interest since the energy density in multiple NN subcollisions is much higher than in pp or p–Pb collisions. Therefore, this chapter focuses on effects that are present in the p_{T} spectra of charged particles due to the creation of QGP and the differences to MC-generated yields by PYTHIA which does not model QGP-like effects.

Firstly, the differences between dividing simulated events into centrality and multiplicity classes are analysed in section 5.4.1. Afterwards, measured and simulated p_{T} spectra are compared with each other in section 5.4.2 and the differences are discussed with respect to our understanding of QGP-like effects. Finally, section 5.4.3 presents the impact of applying the string shoving model to the event generation.

5.4.1. Accuracy of Centrality Determination via Multiplicity Measurement

Similar to the procedure in section 5.3.1, Pb–Pb events are divided in different multiplicity classes due to their fractions of the total charged-particle multiplicity. In contrast to p–Pb collisions, the centrality in collisions of heavy ions can also be determined geometrically by using eq. (9). Since both approaches are possible, this section will discuss to what extent the assignment of multiplicity classes coincides with the geometrical determination of centrality classes.

Firstly, the MC-generated charged-particle multiplicity in Pb–Pb collisions is displayed in fig. 39. All events are divided into nine multiplicity classes between $0\,\%$ and $80\,\%$ according to the number of charged particles measured in the pseudorapidity ranges of the V0A and V0C detectors. Again, the multiplicity is shown once without a centrality filter in the event generation and once for a simulation where all events with $b \geqslant 14\,\mathrm{fm}$ have been sorted out which corresponds to twice the radius of the lead nucleus.

The main difference between these distributions is that the probability to find events with very low N_{ch} is much bigger in the analysis without an impact parameter filter. The same behaviour has been observed in fig. 28 and can be explained by the fact that lead nuclei with a separation $b \geqslant 14\,\mathrm{fm}$ do not collide and only a few particles are generated in electromagnetic interactions. For higher N_{ch}, the behaviour of both distributions is similar. However, there is no continuous exponential decrease in $P(N_{\mathrm{ch}})$ like in the p–Pb multiplicity. Instead, the decrease flattens with increasing N_{ch} per event until

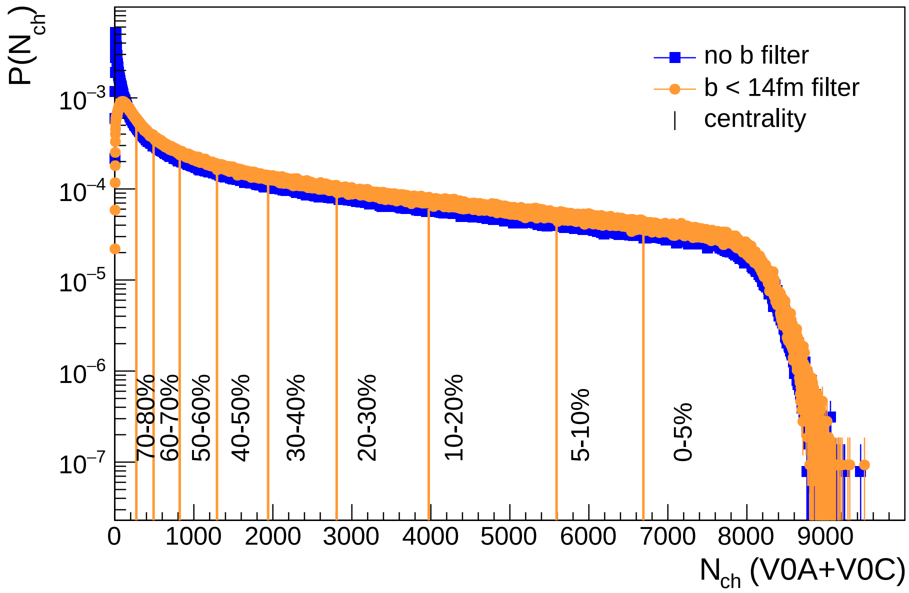

Figure 39: Charged-particle multiplicity of a simulated Pb–Pb collision at $\sqrt{s_{\mathrm{NN}}} = 5.02\,\mathrm{TeV}$ including only final-state charged particles in the V0A+V0C pseudorapidity range with and without an impact parameter filter. The vertical numbers represent the multiplicity class corresponding to the indicated N_{ch}.

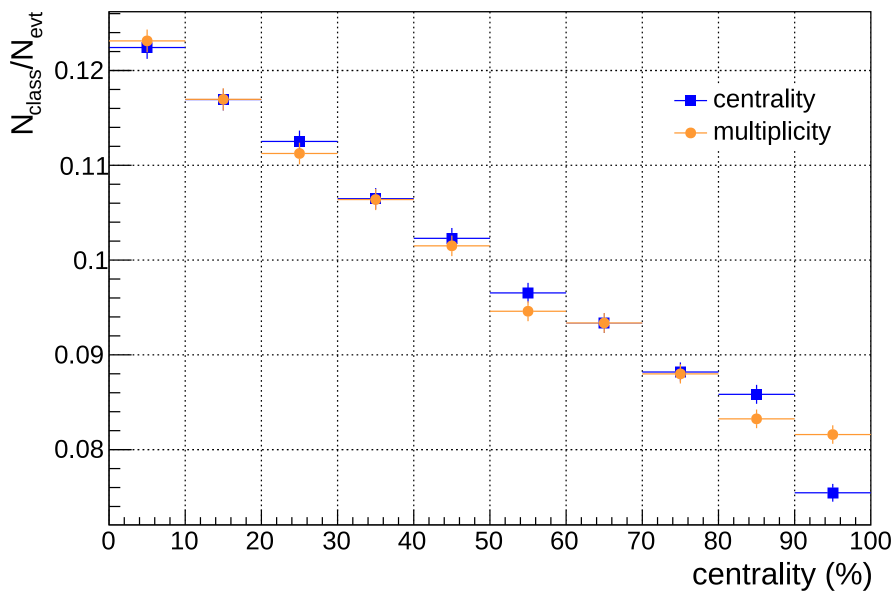

Figure 40: Simulated number of events per multiplicity class compared with geometrically determined centrality classes normalised to the total number of events.

$N_{\text{ch}} = 8000$. The probability to find even more charged particles decreases very sharply and the most charged particles found in an event are around 9000. As expected, this is a much higher number than what is generated in p–Pb collisions.
The boundaries of the multiplicity classes are found by integrating over the total charged-particle multiplicity which includes the mentioned impact parameter filter. The highest 5 % of the integral are events with $N_{\text{ch}} > 6690$. Analogously, the lower limits of the other multiplicity classes are $N_{\text{ch}} = 5591$ (5-10 %), $N_{\text{ch}} = 3973$ (10-20 %), $N_{\text{ch}} = 2808$ (20-30 %), $N_{\text{ch}} = 1940$ (30-40 %), $N_{\text{ch}} = 1293$ (40-50 %), $N_{\text{ch}} = 821$ (50-60 %), $N_{\text{ch}} = 490$ (60-70 %) and $N_{\text{ch}} = 272$ (70-80 %). More peripheral events are not analysed to avoid contamination by electromagnetic processes and selection biases which might have a significant impact on QGP effects in peripheral events [ALI18].
Secondly, these multiplicity classes are compared with the geometrical determination of the collision geometry. The number of events in each class are indicated in fig. 40 once for the geometrical centrality and once for the previously defined multiplicity classes. Both simulations only include events with an impact parameter $b < 14\,\text{fm}$. It turns out that the number of events per class decreases linearly from central to peripheral collisions. Also, centrality and multiplicity classes have the same number of events within their uncertainties except in the most peripheral classes with $c > 80\,\%$. However, this is also the range where experimental data are difficult to obtain without contamination as discussed before.
Hence, the division of events in different classes according to their multiplicity or geometrical centrality leads to the same number of events in the relevant centrality interval. This does not mean, however, that each event is allocated to the same class via multiplicity determination as it is assigned to due to its geometrical centrality. Still, both cases lead to similar results and are thus assumed to be consistent with each other.

5.4.2. Centrality Dependent Transverse-Momentum Spectra

Similar to section 5.3.1, this section compares measured and MC-generated p_{T} spectra with each other for different centralities. Therefore, multiplicity classes in the measurement are determined in the same way as for p–Pb collisions by assigning the events with the highest charged-particle multiplicities to the most central class. The simulated events are classified to their centrality which is calculated via eq. (9). According to the discussion in section 5.4.1, these different types of classifications are comparable with each other.

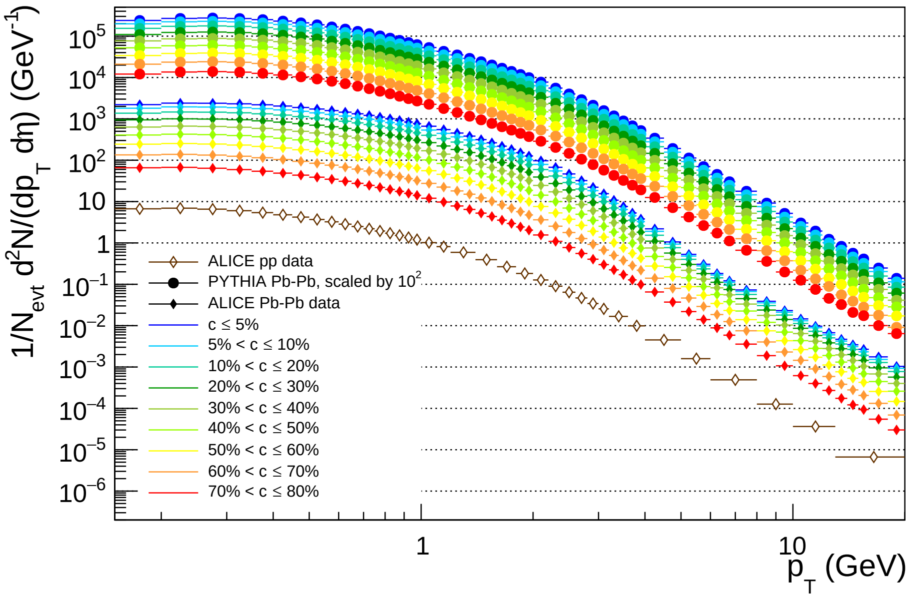

Figure 41: p_T spectra of simulated Pb–Pb collisions at $\sqrt{s_{NN}} = 5.02\,\text{TeV}$ including only final-state charged particles with $|\eta| < 0.8$ and $b < 14\,\text{fm}$ scaled with a factor 10^2 in comparison with measured data (pp and Pb–Pb) from [ALI18].

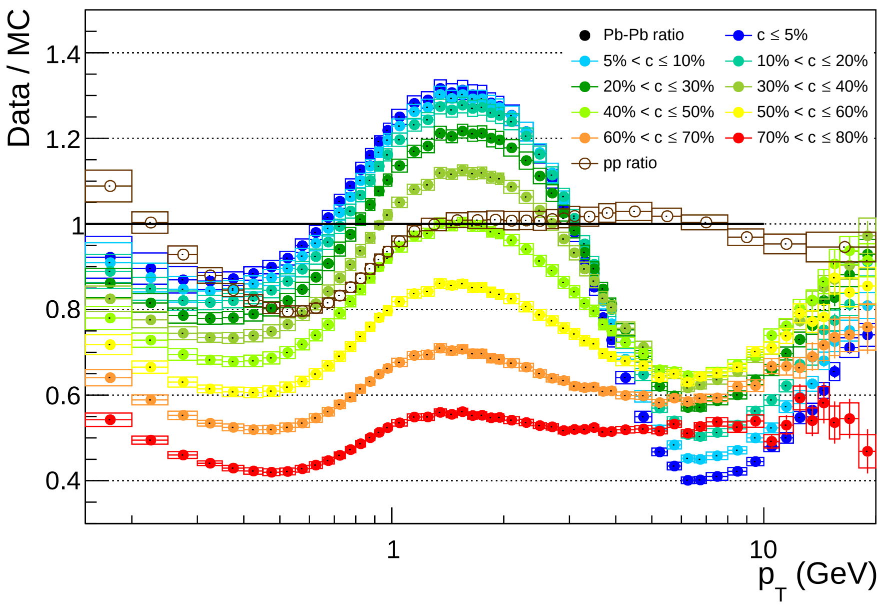

Figure 42: Ratios of the previous shown p_T spectra at $\sqrt{s_{NN}} = 5.02\,\text{TeV}$ including only final-state charged particles with $|\eta| < 0.8$ and with a selection $b < 14\,\text{fm}$. The corresponding ratio from pp collisions is plotted for comparison.

Figure 41 presents yields from measured and simulated Pb–Pb collisions, the latter being multiplied by a factor of 10^2 for better visibility. Again, the yields for a certain p_{T} are decreasing from central to peripheral events. In comparison to the yields from pp collisions in fig. 18, the Pb–Pb yields in the most central class are more than two magnitudes higher while the ones in the most peripheral class are still one magnitude higher. Furthermore, there is a bigger difference between the behaviour of the MC-generated and the measured p_{T}-spectrum. While the former is again decreasing exponentially without irregularities, the latter decreases first weaker until $p_{\mathrm{T}} \approx 4\,\mathrm{GeV}$ and then stronger than the simulated yields which is not observed in a measured yield from pp collisions.
These effects become more obvious by plotting the yields as ratios which is done in fig. 42. In each centrality class, there is a peak in the ratio at $p_{\mathrm{T}} \approx 1.5\,\mathrm{GeV}$. While the maximum of this peak is above unity in the five most central classes, it is below for more peripheral events and decreases down to almost $55\,\%$. Overall, the more central the collision is, the sharper the shape of the peak becomes. Additionally, each distribution shows a minimum at small momenta around $3\,\mathrm{GeV}$ for rather central events and $5\,\mathrm{GeV}$ for rather peripheral events.
Until a momentum of approximately $4\,\mathrm{GeV}$, the ratios are higher for more central collisions. This turns around at higher momenta, where there is a valley in the ratios with a minimum at $p_{\mathrm{T}} \approx 6\,\mathrm{GeV}$. Here, the most central ratio features the biggest deviation from unity where the simulated yield is more than twice as high as the measured one. Going to more peripheral collisions, this deviation decreases. Only the ratio in the most peripheral class $70\,\% < c \leqslant 80\,\%$ falls out of that order. For even higher p_{T}, all ratios except the one in the most peripheral class increase again towards unity.
As a comparison for peripheral Pb–Pb collisions with a rather small number of subcollisions, the pp ratio from fig. 18 which includes $\tau_{0,\mathrm{max}} = 10\,\mathrm{mm}$ is also displayed here. It shows a similar behaviour to the most peripheral Pb–Pb class but is shifted upwards by about 40 percentage points.
While the first part of the spectra for $p_{\mathrm{T}} < 2\,\mathrm{GeV}$ is similar to what has been found in p–Pb collisions in fig. 34, a valley at high momenta has not been observed before. This is caused by effects due to the creation of QGP in heavy-ion collisions. On the one hand, as already discussed, collective effects lead to a blueshift from small to intermediate momenta in the measured yields. Since this is not accounted for in PYTHIA, the MC-generated yield is first overestimating the particle creation at low p_{T} and then underestimating it at intermediate p_{T}. Collective-like effects are also assumed to be present in p–Pb events, leading to a similar behaviour in the ratio. On the other hand,

high energetic partons resulting from collisions of heavy ions lose energy by traversing the QGP which is called jet quenching. This leads to a valley in the ratio at high p_{T} because PYTHIA does not include the creation of QGP. This peak is not present in the p–Pb ratio since there is no medium created to which the partons could lose energy.
In the following, similar ratios of different identified particles are analysed. Ratios of identified pions, for example, are illustrated in fig. 43. These are very similar to the ones in fig. 42 because pions are the largest fraction of all generated charged particles. The biggest difference is that collective effects are less pronounced which can be recognised through the smaller valley at low p_{T} and a smaller peak at intermediate p_{T}. The latter is additionally shifted to smaller momenta slightly above 1 GeV. At $p_{\mathrm{T}} = 0.3\,\mathrm{GeV}$, there is also a discontinuity in the most central ratios similar to the one in fig. 23 due to a change of detector module in the measurement.
Moreover, the course of the distributions in the most peripheral classes with $c > 70\,\%$ is again similar to the comparative pp ratio but shifted down by about 40 to 70 percentage points. Therefore, peripheral events show the same QGP effects that are characteristic to pp collisions. In particular, jet quenching does not seem to appear in very peripheral collisions. Still, that leaves unexplained why the yields in these classes are estimated by PYTHIA to be approximately twice as high as the measured yields.

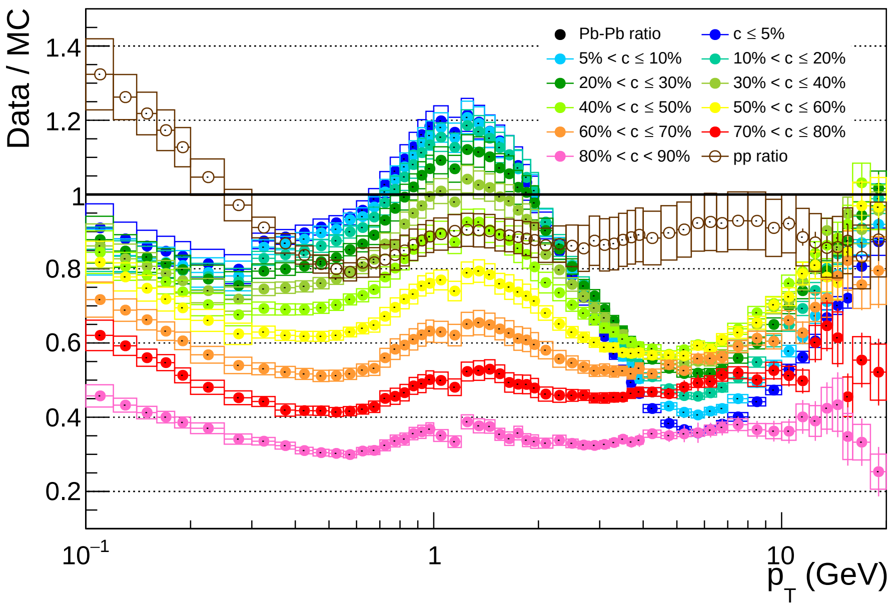

Figure 43: Data/MC ratios of p_{T} spectra at $\sqrt{s_{\mathrm{NN}}} = 5.02\,\mathrm{TeV}$ including only final-state charged pions with $|\eta| < 0.8$ and with a selection $b < 14\,\mathrm{fm}$. The corresponding ratio from pp collisions is plotted for comparison.

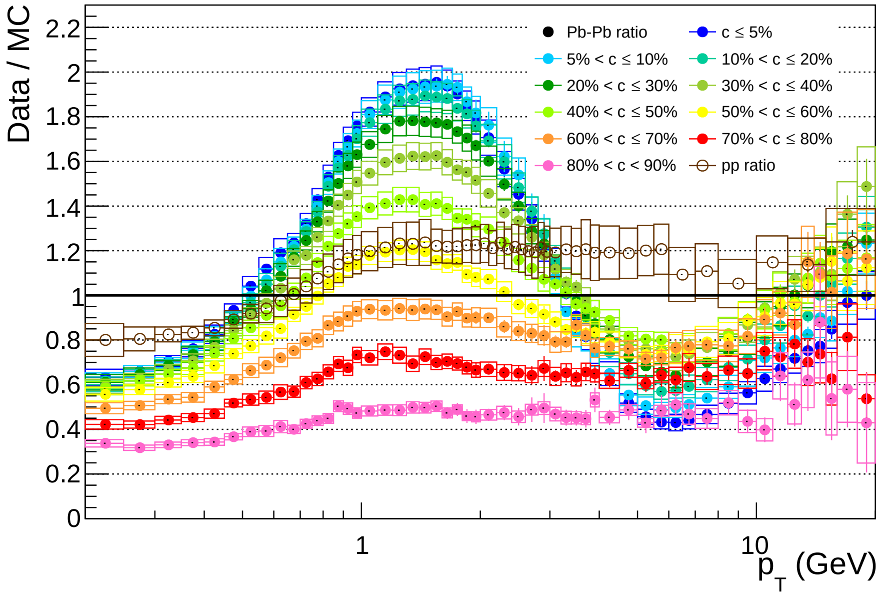

Figure 44: Data/MC ratios of p_{T} spectra at $\sqrt{s_{\mathrm{NN}}} = 5.02\,\mathrm{TeV}$ including only final-state charged kaons with $|\eta| < 0.8$ and with a selection $b < 14\,\mathrm{fm}$. The corresponding ratio from pp collisions is plotted for comparison.

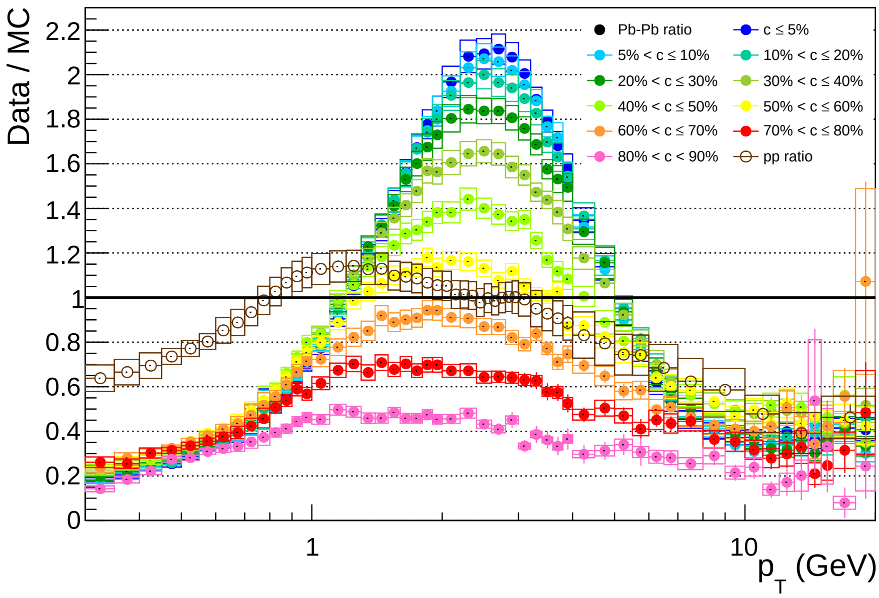

Figure 45: Data/MC ratios of p_{T} spectra at $\sqrt{s_{\mathrm{NN}}} = 5.02\,\mathrm{TeV}$ including only final-state charged protons with $|\eta| < 0.8$ and with a selection $b < 14\,\mathrm{fm}$. The corresponding ratio from pp collisions is plotted for comparison.

In comparison with the centrality dependent p–Pb ratios in fig. 31, the pion distributions here are very different. Firstly, the p–Pb ratios do not show a valley at high p_{T} due to the absence of jet quenching. Secondly, the behaviour at small p_{T} is also different. While the p–Pb yields are mostly overestimated by PYTHIA with ratios up to 200 % in the intermediate-momentum range, Pb–Pb yields are rather underestimated with a maximum ratio in the most central class of 120 % at a transverse momentum around 1 GeV. Additionally, while all p–Pb ratios form a similar deviation at low p_{T} with minima between 70 % to 80 %, there is a clear centrality ordering in the Pb–Pb ratios with minima between 90 % and 30 %.

Analogously, kaon ratios are depicted in fig. 44. Their general behaviour is similar to pions but the ratios reach much higher values above unity. At the maximum around 1.5 GeV, the MC-generated yields are about twice as high as the measured ones. Also at very high p_{T}, the ratios in rather central classes increase again to values above unity and are matching the comparative pp ratio.

In the case of protons (see fig. 45), the peak is shifted to higher momenta around 2.5 GeV. Furthermore, the measured yields are much higher than the simulated ones at low and high p_{T}, respectively, leading to ratios around 30 % to 40 %.

Overall, the differences between the ratios of pions, kaons, and protons are rather small in comparison with the results from pp or p–Pb collisions. Instead, QGP effects are dominating the differences in the spectra. Since PYTHIA does not simulate these effects, particle yields are underestimated at intermediate p_{T} and overestimated at small and high p_{T}. Still, the different ratios differ in the amplitude of the peak at intermediate p_{T}. While the MC-generated yield of pions in the most central class overestimates the measured one only by up to 20 %, the simulated kaon and proton yields are at the same centrality about twice as high as the respective measured yields.

Moreover, the Pb–Pb data/MC ratios are in general smaller than the respective centrality dependent p–Pb ratios. In the case of pions, for example, the p–Pb ratios (over all centrality classes) assume values between 60 % and 250 %, while the Pb–Pb ratios are between 30 % and 120 %. Hence, central events in collisions of two heavy ions are better described by PYTHIA than in p–Pb collisions. The opposite applies for peripheral events which are reproduced quite well in p–Pb collisions, while the MC-generated Pb–Pb yields are two to five times higher than the measured ones.

One attempt to include a description of the blueshift in p_{T} due to collective effect is the string shoving model. The results of applying this model to the generation of heavy-ion events are presented in the next section.

5.4.3. Effects of String Shoving

Similar to the analysis of pp and p–Pb collisions before, the string shoving model has been applied to the MC generation of heavy-ion events to account for collective effects. Firstly, centrality dependent data/MC ratios for all charged particles are presented in fig. 46. These distributions are only displayed for $p_{\mathrm{T}} < 10\,\mathrm{GeV}$ as the statistical errors at higher momenta grow strongly due to lack of statistics. For the same reason, only the default shoving model has been applied without an investigation of the parameter m_{join}. The pp ratio from fig. 22 including shoving is also given as comparison for peripheral Pb–Pb collisions.

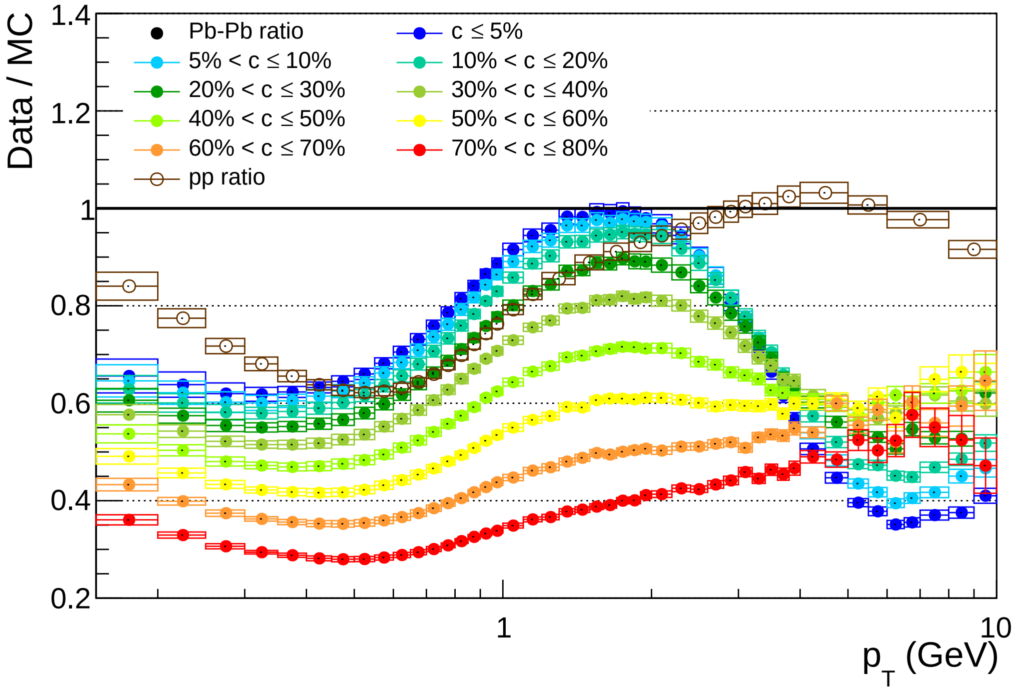

Figure 46: Data/MC ratios of p_{T} spectra at $\sqrt{s_{\mathrm{NN}}} = 5.02\,\mathrm{TeV}$ including all final-state charged particles with $|\eta| < 0.8$ and $b < 14\,\mathrm{fm}$. The string shoving model has been applied to the PYTHIA event generation. The corresponding ratio from pp collisions including shoving is plotted for comparison.

In contrast to the ratios without string shoving (see fig. 42), the Pb–Pb ratios shown here are below unity for all p_{T} and in all centrality classes. This means that all simulated yields are overestimated by PYTHIA. Especially for low p_{T}, the deviation from unity increases. In the most central class, for example, the minimum ratio due to collective effects decreases from slightly under 90 % in the default case to about 60 % with shoving applied, while the most peripheral minimum ratio changes from 40 % to 30 %. Moreover, the peak at intermediate p_T broadens and the three most peripheral classes do not even show a peak any more. This is again resembling the pp ratio but shifted downwards. At $p_T > 4\,\text{GeV}$, the valley due to jet quenching stays rather unchanged in central collisions by applying the shoving model since the model has a default cut off at 2 GeV. However, the minimum of the peak in the most central class is still about four percentage points lower than the default ratio. Instead, in classes which are less central than 50 %, the respective ratios do not show a valley because the values at smaller momenta with string shoving included are even lower than the minimum of the peak at high p_T in fig. 42.

The analysis of identified particle yields with string shoving included in the event generation leads to similar results. In the following, the data/MC ratios of identified pions are illustrated in fig. 47.

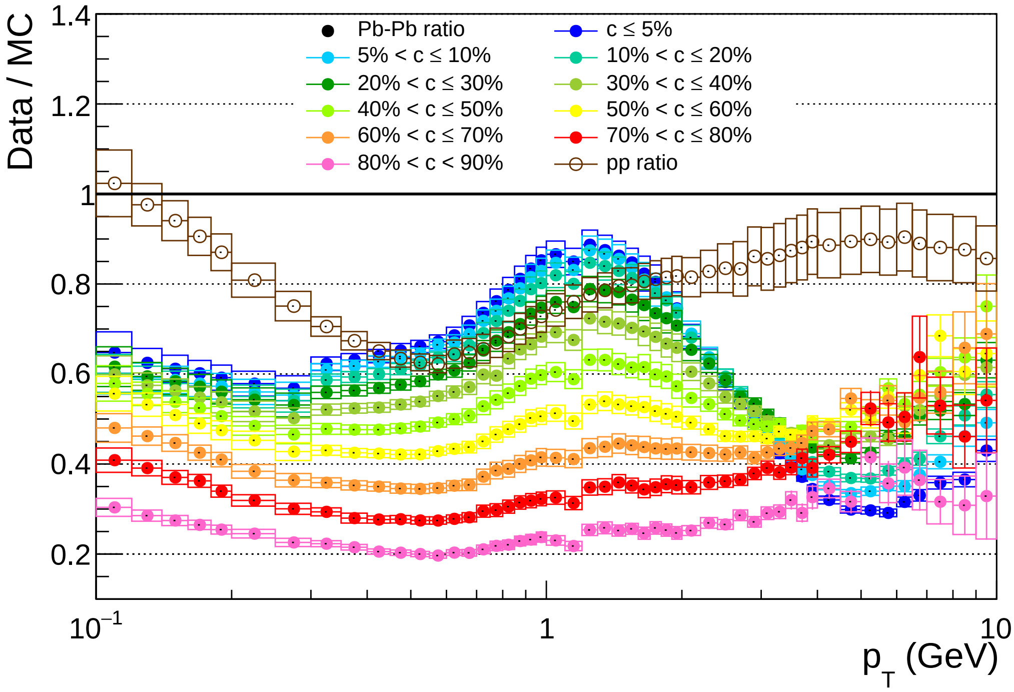

Figure 47: Data/MC ratios of p_T spectra at $\sqrt{s_{NN}} = 5.02\,\text{TeV}$ including only final-state charged pions with $|\eta| < 0.8$ and $b < 14\,\text{fm}$. The string shoving model has been applied to the PYTHIA event generation. The corresponding ratio from pp collisions including shoving is plotted for comparison.

In comparison with the ratios depicted in fig. 43 resulting from a default event generation without shoving, the ratios given here are also shifted down similar to the case of all charged particles. This down-shift mainly increases the deviation at small p_T and broadens the peak at intermediate p_T while the peak at high p_T is rather unchanged. The comparative pp ratio shows again a behaviour similar to the most peripheral ratios but it is closer to unity. The same results can be obtained from an analysis of kaon and proton yields with string shoving applied which can be seen in appendix A.

Overall, using the string shoving model in the PYTHIA generation of heavy-ion events leads to higher simulated particle yields mostly at $p_\mathrm{T} < 4\,\mathrm{GeV}$. This leads to a down-shift in the most central data/MC ratio with all charged particles of about 30 percentage points for small and intermediate p_T, while the most peripheral ratio is only changed by about 10 percentage points. At the same time, the yield at higher p_T only increases slightly which does not have a major effect on the ratio.

This shows that the string shoving model accounts for too small yields in the simulation at intermediate p_T due to the blueshift of momenta in the measurement. However, similar to the analyses in section 5.2.3 and section 5.3.3, the MC-generated yield also increases for small p_T which leads to an even bigger deviation between simulation and data. Additionally, only the most central ratio in fig. 46 agrees with the measured spectrum at the peak at intermediate p_T. In all other classes, the decrease in the ratios due to shoving is too big and PYTHIA overestimates the yields in the most peripheral collisions by factors of up to three in the analysis of all charged particles or even five for identified pion yields.

Hence, the default string shoving model increases simulated particle yields more than necessary to account for collective effects. This might be improved by including an analysis of the m_join parameter in the event generation or by applying a sensible tune.

6. Conclusion and Outlook

In this thesis, different spectra measured in ALICE have been compared with results from the PYTHIA event generator. This has been done for pp collisions as well as for collisions including lead nuclei, the latter being simulated by using the Angantyr model. A particular focus was on the analysis of effects attributed to the creation of QGP.

For collisions of protons, the reconstruction of p_{T} spectra has been analysed for all charged particles and for identified charged pions, kaons, and (anti-)protons. While the single particle yields mostly deviate from the measurement, the data/MC ratio of all charged particles includes unity within its uncertainties in the intermediate-momentum range. For $p_{\mathrm{T}} < 1\,\mathrm{GeV}$, there is a valley in the ratio due to an overestimation of the MC-generated yield. A possible reason for that is a blueshift in the measured transverse momenta due to collective-like effects which are not included in PYTHIA.

The string shoving model is one attempt to account for these effects. However, simulations including this model lead to even higher yields. Especially at small p_{T}, where the default PYTHIA yield is already higher than the one in the measurement, this leads to even larger deviations. This can partly be explained by an increase in multiplicity due to excitation gluons. These can be joined by setting the m_{join} parameter. Still, the resulting deviations from measured yields are larger than in a simulation without string shoving enabled. Also, $\langle p_{\mathrm{T}} \rangle$ in dependence of the N_{ch} per event is reconstructed best in a simulation without shoving. The most probable reason for these deviations is that the simulations in this thesis have been performed by using the default Monash 2013 tune since PYTHIA does not provide a sensible tune for the string shoving model yet.

The increase in particle production was also shown in an analysis of the charged-particle multiplicity. In the default PYTHIA event generation, there are much less events with $N_{\mathrm{ch}} > 100$ than in the measurement. String shoving leads to higher probabilities for having more charged particles per event. By including $m_{\mathrm{join}} = 1\,\mathrm{GeV}$, the probability to find events with $N_{\mathrm{ch}} > 120$ agrees within the uncertainties with the measured charged-particle multiplicity.

In p–Pb collisions, p_{T} spectra have been compared with measurements from ALICE in a MB analysis of NSD events and for events divided in multiplicity classes. The former analysis shows a similar valley for small p_{T} as in the pp ratio, but the deviations at higher momenta are much larger. In the latter case, the multiplicity classes have been identified in an integral over the charged-particle multiplicity. Additionally, the effects of an impact parameter filter $b < 8\,\mathrm{fm}$ have been analysed. It turned out that the resulting

data/MC ratios are ordered from central to peripheral classes. In all classes, there is an overestimation of PYTHIA at small p_T. At larger momenta, the measured yields in the most central class are up to three times higher than the simulated ones, whereas they are lower in the most peripheral class.
The default string shoving model does not lead to an improvement of the description of p_T spectra in p–Pb collisions. By setting $m_{\text{join}} = 1\,\text{GeV}$ to account for excitation gluons, however, the MC-generated yields increase at intermediate to high p_T which leads to smaller deviations from measured yields. In contrast to that, the deviations at low p_T are still larger than in simulations without shoving.
In Pb–Pb collisions, it has been shown that a division into centrality and multiplicity classes leads to a similar number of events per class, except for centralities above 80 %. The data/MC ratios of p_T spectra are also ordered by centrality. For all charged particles as well as for identified pions, kaons, and protons, they show a peak at intermediate p_T and a valley at small and high p_T due to collective effects and jet quenching. The distributions broaden from central to peripheral which means that QGP effects are much stronger in central than in peripheral collisions. Moreover, the yields are rather overestimated by PYTHIA in contrast to p–Pb collisions where the simulated yields are much lower than measured ones at high p_T. Hence, in Pb–Pb collisions, the description of central yields is more accurate than for peripheral ones, whereas this is the other way round in p–Pb collisions.
Applying the default string shoving model to the generation of Pb–Pb events leads to smaller data/MC ratios at low to intermediate p_T. This accounts for an underestimation by PYTHIA in central collisions at intermediate p_T due to the absence of collective-like effects. In peripheral collisions as well as for all centrality classes at small p_T, this downshift leads to even larger deviations. The valley at high p_T is unchanged since string shoving does not include a description of jet quenching.
Overall, the string shoving model leads to higher deviations from unity in data/MC ratios at small p_T in all three analysed collision types. This differs from the expectations from a model that is supposed to account for collective-like effects. In further analyses, this might be improved by providing a sensible tune to string shoving in PYTHIA. By doing so, the impact of different settings in the m_{join} parameter could also be tested. Furthermore, a model of jet quenching in MC-generated heavy ion collisions could be tested since this is not accounted for by the string shoving model.
Finally, the current version of the string shoving model without a sensible tune should be used with caution.

A. Appendix

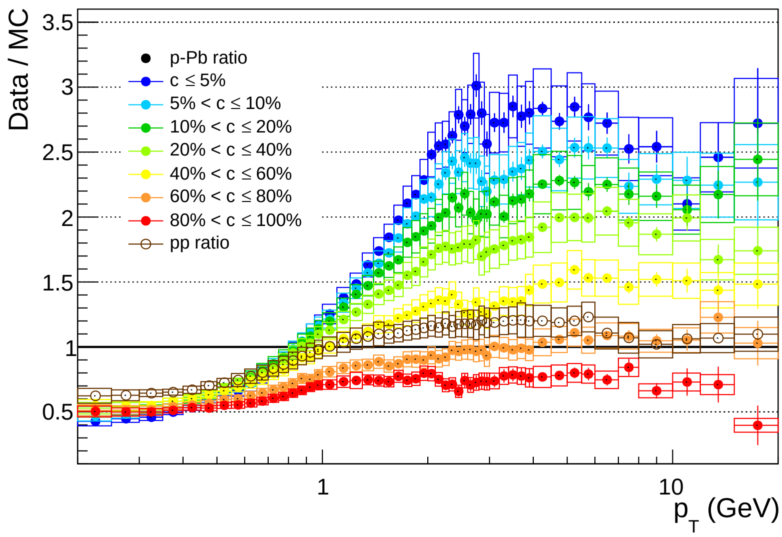

Figure 48: Data/MC ratios of p_{T} spectra at $\sqrt{s_{\mathrm{NN}}} = 5.02\,\mathrm{TeV}$ including only final-state kaons with $-0.5 < y_{\mathrm{CM}} < 0.0$ with $b < 8\,\mathrm{fm}$. The default string shoving model has been applied to the PYTHIA event generation. The corresponding pp ratio is plotted for comparison.

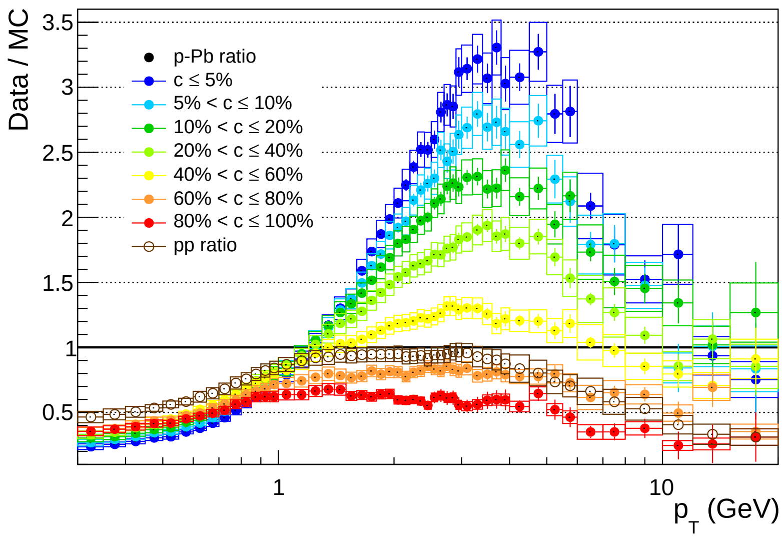

Figure 49: Data/MC ratios of p_{T} spectra at $\sqrt{s_{\mathrm{NN}}} = 5.02\,\mathrm{TeV}$ including only final-state protons with $-0.5 < y_{\mathrm{CM}} < 0.0$ with $b < 8\,\mathrm{fm}$. The default string shoving model has been applied to the PYTHIA event generation. The corresponding pp ratio is plotted for comparison.

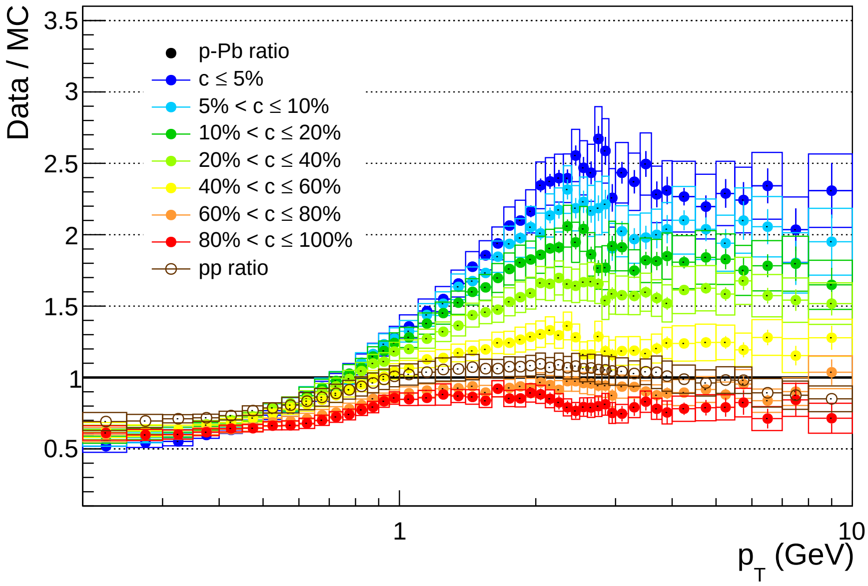

Figure 50: Data/MC ratios of p_{T} spectra at $\sqrt{s_{\mathrm{NN}}} = 5.02\,\mathrm{TeV}$ including only final-state kaons with $-0.5 < y_{\mathrm{CM}} < 0.0$ and $b < 8\,\mathrm{fm}$. String shoving has been applied with $m_{\mathrm{join}} = 1\,\mathrm{GeV}$. The corresponding pp ratio is plotted for comparison.

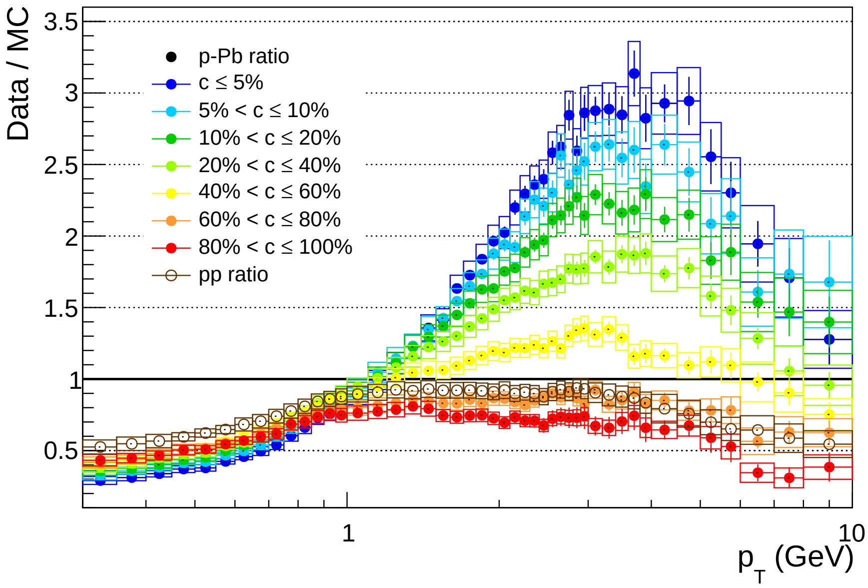

Figure 51: Data/MC ratios of p_{T} spectra at $\sqrt{s_{\mathrm{NN}}} = 5.02\,\mathrm{TeV}$ including only final-state protons with $-0.5 < y_{\mathrm{CM}} < 0.0$ and $b < 8\,\mathrm{fm}$. String shoving has been applied with $m_{\mathrm{join}} = 1\,\mathrm{GeV}$. The corresponding pp ratio is plotted for comparison.

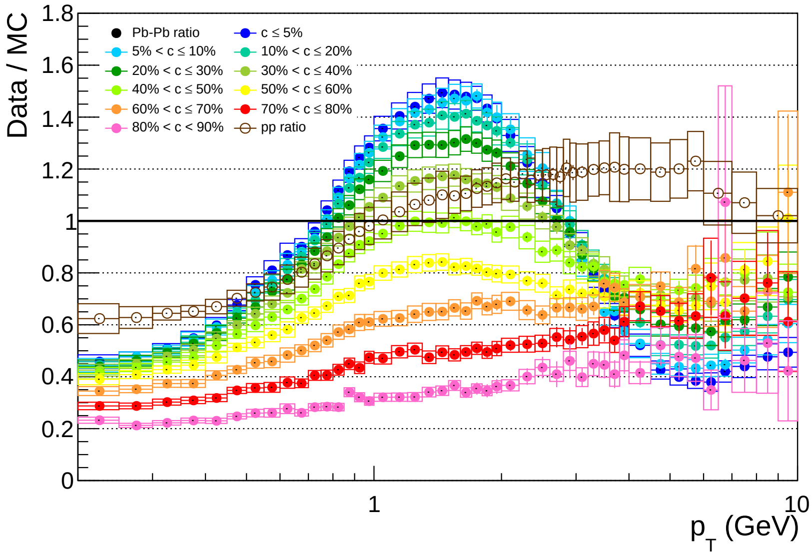

Figure 52: Data/MC ratios of p_{T} spectra at $\sqrt{s_{\mathrm{NN}}} = 5.02\,\mathrm{TeV}$ including only final-state charged kaons with $|\eta| < 0.8$ and $b < 14\,\mathrm{fm}$. The string shoving model has been applied to the PYTHIA event generation. The corresponding pp ratio is plotted for comparison.

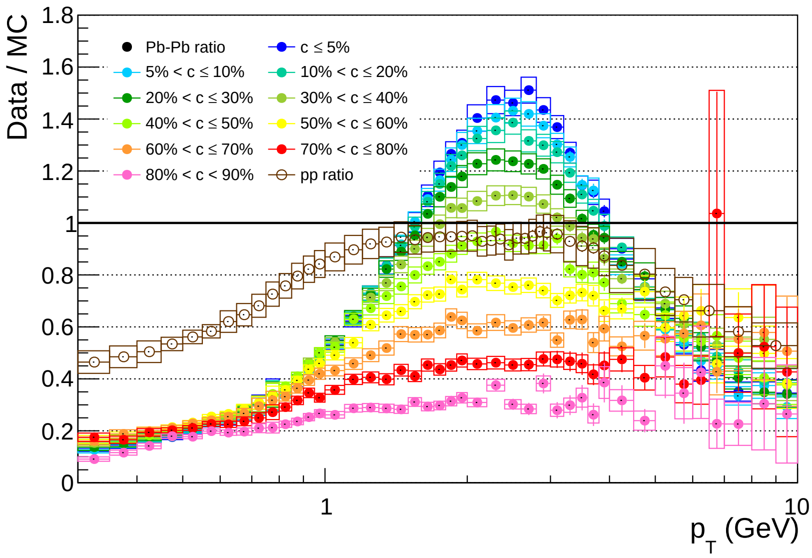

Figure 53: Data/MC ratios of p_{T} spectra at $\sqrt{s_{\mathrm{NN}}} = 5.02\,\mathrm{TeV}$ including only final-state charged protons with $|\eta| < 0.8$ and $b < 14\,\mathrm{fm}$. The string shoving model has been applied to the PYTHIA event generation. The corresponding pp ratio is plotted for comparison.

References

[ADS09] M. Alvioli, H.J. Drescher and M. Strikman. ‘A Monte Carlo generator of nucleon configurations in complex nuclei including nucleon–nucleon correlations’. In: *Physics Letters B* 680.3 (2009), pp. 225–230. ISSN: 0370-2693. DOI: https://doi.org/10.1016/j.physletb.2009.08.067. URL: https://www.sciencedirect.com/science/article/pii/S0370269309010442.

[ALI08] K. Aamodt et al. (ALICE Collaboration). ‘The ALICE experiment at the CERN LHC’. In: *Journal of Instrumentation* 3.08 (Aug. 2008), S08002. DOI: 10.1088/1748-0221/3/08/S08002. URL: https://dx.doi.org/10.1088/1748-0221/3/08/S08002.

[ALI14] B. Abelev et al. (ALICE Collaboration). ‘Performance of the ALICE experiment at the CERN LHC’. In: *International Journal of Modern Physics A* 29.24 (Sept. 2014), p. 1430044. DOI: 10.1142/s0217751x14300440. URL: https://www.worldscientific.com/doi/abs/10.1142/S0217751X14300440.

[ALI16] J. Adam et al. (ALICE Collaboration). ‘Multiplicity dependence of charged pion, kaon, and (anti)proton production at large transverse momentum in p–Pb collisions at $\sqrt{s_{\mathbf{NN}}} = 5.02$ TeV’. In: *Physics Letters B* 760 (2016), pp. 720–735. ISSN: 0370-2693. DOI: https://doi.org/10.1016/j.physletb.2016.07.050. URL: https://www.sciencedirect.com/science/article/pii/S0370269316303914.

[ALI18] S. Acharya et al. (ALICE Collaboration). ‘Transverse momentum spectra and nuclear modification factors of charged particles in pp, p-Pb and Pb-Pb collisions at the LHC’. In: *Journal of High Energy Physics* 2018.11 (Nov. 2018). DOI: 10.1007/jhep11(2018)013. URL: https://link.springer.com/article/10.1007/JHEP11(2018)013.

[ALI20] S. Acharya et al. (ALICE Collaboration). ‘Production of charged pions, kaons, and (anti-)protons in Pb-Pb and inelastic pp collisions at $\sqrt{s} = 5.02$ TeV’. In: *Physical Review C* 101.4 (Apr. 2020). DOI: 10.1103/physrevc.101.044907. URL: https://journals.aps.org/prc/abstract/10.1103/PhysRevC.101.044907.

[And14] Anton Andronic. ‘An overview of the experimental study of quark–gluon matter in high-energy nucleus–nucleus collisions’. In: *International Journal* *of Modern Physics A* 29.22 (Aug. 2014), p. 1430047. DOI: 10.1142/s0217751x14300476. URL: https://www.worldscientific.com/doi/abs/10.1142/S0217751X14300476.

[AS00] B. Andersson and F. Söderberg. 'The diagonalisation of the Lund fragmentation model I'. In: *Eur. Phys. J. C* 16 (Aug. 2000), pp. 303–310. DOI: 10.1007/s100520050023. URL: https://doi.org/10.1007/s100520050023.

[BC03] L. Betev and P. Chochula. *Definition of the ALICE Coordinate System and Basic Rules for Sub-detector Components Numbering*. 2003. URL: https://alice-servotech.web.cern.ch/HELP_DCDB-SVT/Help_Files/ALICE-INT-2003-038.pdf (visited on 15/02/2023).

[BD16] Cosimo Bambi and Alexandre D. Dolgov. 'The Standard Model of Particle Physics'. In: *Introduction to Particle Cosmology: The Standard Model of Cosmology and its Open Problems*. Berlin, Heidelberg: Springer Berlin Heidelberg, 2016, pp. 35–52. ISBN: 978-3-662-48078-6. DOI: 10.1007/978-3-662-48078-6_3. URL: https://doi.org/10.1007/978-3-662-48078-6_3.

[Ber06] Christoph Berger. 'Das Standard-Modell'. In: *Elementarteilchenphysik*. Berlin, Heidelberg: Springer Berlin Heidelberg, 2006, pp. 391–471. ISBN: 978-3-540-33594-8. DOI: 10.1007/3-540-33594-3. URL: https://doi.org/10.1007/3-540-33594-3.

[Bie+18] Christian Bierlich et al. 'The Angantyr model for heavy-ion collisions in Pythia8'. In: *Journal of High Energy Physics* 2018.10 (Oct. 2018). DOI: 10.1007/jhep10(2018)134. URL: https://link.springer.com/article/10.1007/JHEP10(2018)134.

[Bie+22] Christian Bierlich et al. *A comprehensive guide to the physics and usage of PYTHIA 8.3*. 2022. DOI: 10.48550/ARXIV.2203.11601. URL: https://arxiv.org/abs/2203.11601.

[Buc+11] Andy Buckley et al. 'General-purpose event generators for LHC physics'. In: *Physics Reports* 504.5 (July 2011), pp. 145–233. DOI: 10.1016/j.physrep.2011.03.005. URL: https://www.sciencedirect.com/science/article/pii/S0370157311000846?via%3Dihub.

[CER23a] CERN. *About CERN*. 2023. URL: https://home.web.cern.ch/about (visited on 14/02/2023).

[CER23b] CERN. *LHC - The guide*. 2023. URL: https://cds.cern.ch/record/2809109/files/CERN-Brochure-2021-004-Eng.pdf (visited on 15/02/2023).

[Col17] ALICE Collaboration. 'Charged-particle multiplicity distributions over a wide pseudorapidity range in proton-proton collisions at $\sqrt{s} = 0.9$, 7 and 8 TeV'. In: (2017). arXiv: 1708.01435 [hep-ex].

[Col22a] ALICE Collaboration. *Multiplicity dependence of charged-particle production in pp, p-Pb, Xe-Xe and Pb-Pb collisions at the LHC*. 2022. arXiv: 2211.15326 [nucl-ex].

[Col22b] ALICE Collaboration. *The ALICE experiment – A journey through QCD*. 2022. arXiv: 2211.04384 [nucl-ex].

[Dem17] Wolfgang Demtröder. 'Physik der Elementarteilchen'. In: *Experimentalphysik 4*. Springer Berlin Heidelberg, 2017, pp. 161–198. ISBN: 978-3-662-52883-9. DOI: 10.1007/978-3-662-52884-6. URL: https://doi.org/10.1007/978-3-662-52884-6.

[dEn10] David d'Enterria. 'Jet quenching'. In: *Relativistic Heavy Ion Physics*. Springer Berlin Heidelberg, 2010, pp. 471–520. DOI: 10.1007/978-3-642-01539-7_16. URL: https://arxiv.org/abs/0902.2011.

[FS18] Silvia Ferreres-Solé and Torbjörn Sjöstrand. 'The space–time structure of hadronization in the Lund model'. In: *The European Physical Journal C* 78.11 (Nov. 2018). DOI: 10.1140/epjc/s10052-018-6459-8. URL: https://link.springer.com/article/10.1140/epjc/s10052-018-6459-8.

[GR10] Jan Fiete Grosse-Oetringhaus and Klaus Reygers. 'Charged-particle multiplicity in proton–proton collisions'. In: *Journal of Physics G: Nuclear and Particle Physics* 37.8 (July 2010), p. 083001. DOI: 10.1088/0954-3899/37/8/083001. URL: https://doi.org/10.1088%5C%2F0954-3899%5C%2F37%5C%2F8%5C%2F083001.

[Höc15] Stefan Höche. *Introduction to parton-shower event generators*. 2015. arXiv: 1411.4085 [hep-ph].

[Ian14] Edmond Iancu. 'QCD in heavy ion collisions'. In: *2011 European School of High-Energy Physics*. 2014, pp. 197–266. DOI: 10.5170/CERN-2014-003.197. arXiv: 1205.0579 [hep-ph].

[Kli+09] Michael Kliemant et al. 'Global Properties of Nucleus–Nucleus Collisions'. In: *The Physics of the Quark-Gluon Plasma*. Springer Berlin Heidelberg, 2009, pp. 23–103. DOI: 10.1007/978-3-642-02286-9_2. URL: https://doi.org/10.1007/978-3-642-02286-9_2.

[Mil+07] Michael L. Miller et al. 'Glauber Modeling in High-Energy Nuclear Collisions'. In: *Annual Review of Nuclear and Particle Science* 57.1 (Nov. 2007), pp. 205–243. DOI: 10.1146/annurev.nucl.57.090506.123020. URL: https://www.annualreviews.org/doi/10.1146/annurev.nucl.57.090506.123020.

[Pov+14] B. Povh et al. 'Quarks, Gluonen und starke Wechselwirkung'. In: *Teilchen und Kerne*. Springer Berlin Heidelberg, 2014, pp. 103–121. ISBN: 978-3-642-37821-8. DOI: 10.1007/978-3-642-37822-5. URL: https://doi.org/10.1007/978-3-642-37822-5.

[Rei22] F. Reidt. 'Upgrade of the ALICE ITS detector'. In: *Nuclear Instruments and Methods in Physics Research Section A: Accelerators, Spectrometers, Detectors and Associated Equipment* 1032 (June 2022), p. 166632. DOI: 10.1016/j.nima.2022.166632. URL: https://doi.org/10.1016%5C%2Fj.nima.2022.166632.

[Sne11] Raimond Snellings. 'Elliptic flow: a brief review'. In: *New Journal of Physics* 13.5 (May 2011), p. 055008. DOI: 10.1088/1367-2630/13/5/055008. URL: https://iopscience.iop.org/article/10.1088/1367-2630/13/5/055008.

Acknowledgements

First of all, I want to thank Anton Andronic for the numerous discussions of questions and for his guidance whenever it was needed. I also want to thank him and Christian Klein-Bösing for the opportunity to write this thesis in their group. Furthermore, I want to thank all the people in the working group for their advise, for proof reading this thesis, and for the nice time we had together. Special thanks also goes to all the people in my office who accompanied the work on this thesis with helpful discussions and pleasant distractions when they were needed.

Apart from that, I would like to thank my family and my friends for their company and support during the course of this thesis and all the years before. Last but definitely not least, I want to thank my partner for being there for me in stressful times and for all the emotional support.